Karlsruher Institut für Technologie

Physikalisches Institut

Fakultät für Physik

Karlsruher Institut für Technologie

Investigation of Dielectric Losses in Amorphous Thin Films

Untersuchung Dielektrischer Verluste in Amorphen Dünnschichtfilmen

Diplomarbeit

von

Sebastian Tobias Skacel

21. Oktober 2010

Referent: **Prof. Dr. A. V. Ustinov**
Korreferent: Prof. Dr. M. Siegel
Betreuer: Dipl. Phys. Ch. Kaiser

Zusammenfassung

1971 zeigten Zeller und Pohl in ihrer wegweisenden Arbeit, dass sich die Tieftemperatureigenschaften von Gläsern drastisch von denen idealer Kristalle unterscheiden. Noch faszinierender war die Entdeckung fast universeller thermischer Eigenschaften von Gläsern. Dies rief ein wachsendes Interesse am Verständnis von Gläsern hervor und die Physik der Gläser avancierte zu einem enorm vorangetriebenen Fachbereich innerhalb der Naturwissenschaften. Zu dieser Zeit nahm man an, dass die thermischen Eigenschaften dielektrischer Festkörper (wie Gläser) durch Phononen langer Wellenlänge bestimmt würden. Phononen werden durch das elastische Verhalten von Festkörpern charakterisiert, das über eine Distanz gemittelt wird, die vergleichbar ist mit ihrer Wellenlänge. Bei Temperaturen $T < 1$ K ist die Wellenlänge der dominierenden Phononen um ein tausendfaches größer als der Abstand zwischen den Atomen des Festkörpers. Deshalb erwartete man keinen Unterschied zwischen dem Verhalten von Gläsern mit ihrer ungeordneten Struktur und dem der Kristalle, die ein reguläres Gitter aufweisen. Jedoch deuteten das beobachtete ungewöhnliche Verhalten der spezifischen Wärme und der thermischen Leitfähigkeit von Gläsern darauf hin, dass diese ihren Ursprung in der ungeordneten Struktur der Gläser haben. 1972 entwickelten Anderson und Phillips unabhängig von einander eine theoretische Beschreibungsmöglichkeit, die die ungewöhnlichen Tieftemperatureigenschaften der Gläser erklären konnte. Im Rahmen dieses Modells werden Defektzustände in amorphen Festkörpern durch Doppelmuldenpotentiale beschrieben, was zur Annahme von Zwei-Niveau-Systemen (ZNS) in amorphen Festkörpern führt, die in der Lage sind durch die Potentialbarrieren durchzutunneln. Daher wurde dieses Modell *Tunnelmodell* genannt. Unter Inbezugnahme diese Modells konnte das ungewöhnliche Verhalten der spezifischen Wärme auf Relaxationsprozesse von ZNS mit einer breiten Verteilung der Aufspaltung ihrer zwei Energieniveaus zurückgeführt werden. Beobachtete, nichtlineare Verhalten der Ultraschallabsättigung, der dielektrischen Verluste sowie Änderungen der dielektrischen Konstante und der Schallgeschwindigkeit in Gläsern konnten im Rahmen des Tunnelmodells durch resonante Absorption von Phononen bzw. Photonen durch die ZNS bei sehr tiefen Temperaturen erlärt werden.

In jüngster Zeit erwuchs neues Interesse an den ungewöhnlichen Tieftemperatureigenschaften der Gläser vom Gebiet der Entwicklung supraleitender, künstlicher Quantenzustände. Für das supraleitende Phasen-Quantenbit (Qubit) beispielsweise wurde eine Beeinträch-

tigung seiner Funktionsweise auf Grund von ZNS festgestellt, die an das Qubit koppeln und ihm somit Energie entziehen. Das führt in der Folge zu starken Dekohärenteffekten. Im Prinzip besteht ein supraleitendes Phasen-Qubit aus einem supraleitenden Ring, der von einer sog. Josphson junction unterbrochen wird. Es wurde gezeigt, dass die Dekohärenz mit steigenden dielektrischen Verlusten in den Dielektrika, die für die Herstellung der Phasenqubits benutzt werden, zunimmt. Das legte nahe, dass die ZNS, die für die dielektrischen Verluste und für die Dekohärenz verantwortlich sind, identisch sind. Folglich wurden in den letzten Jahren dielektrische Verluste in amorphen Dünnschichtfilmen gründlich untersucht, was zu bedeutenden Resultaten geführt hat. Untersuchungen mit supraleitenden Mikrowellenresonatoren waren in der Lage die ZNS in den dielektrischen Materialien sowie in dünnen Schichten auf den Oberflächen der Resonatoren festzustellen. Diesen ZNS konnte derselbe Ursprung nachgewiesen werden, wie denen, die drei Jahrzehnte zuvor in Gläsern festgestellt wurden. Beide waren in sehr guter Übereinstimmung mit den Vorhersagen des Tunnelmodells. Obwohl mittlerweile ein detailliertes Verständnis von durch ZNS hervorgerufenen Effekten in supraleitenden Mikrowellenbauteilen erarbeitet werden konnte, bleiben dennoch Fragen offen. Vor Allem wurden bisher die Absolutwerte der dielektrischen Verluste sowie deren Frequenzabhängigkeit nicht zuverlässig untersucht. Gerade diese Untersuchungen sind jedoch von größter Wichtigkeit für die Qubitentwicklung. Auf Grund von Untersuchungen dielektrischer Verluste in Gläsern sowie durch neueste Ergebnisse diesbezüglich in supraleitenden Mikrowellenbauteilen wird die Zustandsdichte der ZNS bezüglich der dielektrischen Verluste als konstant angenommen, obwohl Untersuchungen der spezifischen Wärme von Gläsern ergeben haben, dass diese Zustandsdichte sehr wohl frequenzabhängig ist.

Da, wie schon angesprochen, die ZNS, die verantwortlich sind für die Dekohärenz, und diejenigen, die verantwortlich sind für dielektrische Verluste, ein und dieselben sind, war es das Ziel dieser Arbeit dielektrische Verluste amorpher Materialien zu untersuchen, die gewöhnlich in der Qubit-Herstellung verwendet werden. Somit sollten viel versprechende Dielektrika für die Entwicklung von Qubits aufgezeigt werden. Indem dielektrische Verluste im Arbeitsbereich von Qubits (sehr tiefe Temperaturen und sehr geringe Anregungsenergien) untersucht werden konnten, war es ein weiteres Ziel die physikalische Eigenschaften der ZNS an sich aufzudecken. Dafür wurde in dieser Arbeit eine bestehende Messmethode benutzt, die in der Lage war direkt und zuverlässig dielektrische Verluste in amorphen Dünnschichtfilmen zu ermitteln, indem sie supraleitende Mikrowellenresonatoren zu Hilfe nahm. Diese Methode wurde erweitert, in dem die Anzahl der Resonatoren pro Chip erhöht wurde. Damit erlaubte sie es Verluste in den Dünnschichtfilmen als auch an den Grenzschichten zwischen dem supraleitenden Metall und dem Dielektrikum an mehreren Frequenzen in einem breiten Frequenzband quantitativ in einem Tieftemperaturmessgang zu bestimmen. Zuerst wurden die Verluste in Dünnschichtfilmen von Nb_2O_5, AlO_x, SiO, SiN_x and a-Si:H bei einer Temperatur von 4.2 K im GHz-Bereich gemessen. Dabei konnten

sie die Resultate früherer Arbeiten bestätigen, wonach Verluste im amorphen Festkörper jene der Grenzschichten deutlich überwogen. Mit Hilfe des neuen Resonatordesigns mit mehreren Resonatoren pro Chip konnte die Frequenzabhängigkeit der dielektrischen Verluste untersucht werden, was ein Verhalten bestätigte, das schon früher festgestellt worden war, nämlich das einer universellen Gesetzmäßigkeit. Diese Gesetzmäßigkeit wird durch gebrochenzahlige Potenzgesetze der Form $\tan\delta \propto \omega^{n-1}$ ausgedrückt, wonach der dielektrische Verlust auf Grund von Relaxationsprozessen der ZNS in den Dielektrika direkt proportional zur Frequenz ist. Der gefundene enge Bereich des Exponenten von $0.57 < n < 0.68$ für alle Materialien, die in dieser Arbeit untersucht wurden, legte nahe, dass der Ursprung der ZNS in Dipolen zu finden ist, die durch Vielteilchenwechselwirkung miteinander interagieren und für alle untersuchten Materialien gleich sind. Die absoluten Verlustwerte aller untersuchten Materialien stimmten verglichen miteinander mit der Reihenfolge überein, die erst kürzlich festgestellt wurde. Nb_2O_5 mit dem höchsten Gehalt an Sauerstoff hatte mit Abstand die meisten Verluste, wohingegen s-Si:H, in dem die Defektzustände mit Wasserstoff abgesättigt werden, die geringsten Verluste aufwies, und damit ein viel versprechender Kandidat für die Qubitherstellung ist. Trotz seiner hohen Verluste wird Nb_2O_5 oft in der Nb basierten Qubit-Herstellung verwendet. Aus diesem Grund wurde versucht die Verluste von anodisch oxidiertem Nb_2O_5 durch die Benutzung unterschiedlicher Elektrolyte zu reduzieren, was jedoch nicht erreicht werden konnte. Im Fall von a-Si:H wurde ausprobiert, ob spezielle Behandlungen der Grenzschicht zwischen Supraleiter und Dielektrikum zu einer Reduktion der dielektrischen Verluste führen würden. Aber auch hier konnte bisher noch kein Erfolg verzeichnet werden.

Ein weiterer, sehr wichtiger Teil dieser Arbeit bestand in der Untersuchung der Temperatur−, Leistungs- und Frequenzabhängigkeit der dielektrischen Verluste bei Temperaturen $T < 1\,\mathrm{K}$, die durch kryogene Kühlungsverfahren erreicht wurden. Da herkömmliche Tieftemperatur-Mikrowellen-Messaufbauten durch Bauteile mit engbandigem Frequenzbereich eingeschränkt sind, musste ein breitbandiger Messaufbau entwickelt werden. Dieser neue Messaufbau in Verbindung mit dem neuen Resonatordesign war in der Lage die Frequenzabhängigkeit dielektrischer Verluste zum ersten Mal zuverlässig messen zu können, da die Frequenzabhängigkeit in einem Tieftemperaturmessgang untersucht werden konnte. Bei kleinen Leistungen und Temperaturen ($T < 1$ K) konnte ein Anstieg der dielektrischen Verluste mit sinkender Temperatur festgestellt werden. Des Weiteren wurde ein Sättigungseffekt der Verluste für kleiner werdende Leistungen festgestellt. Zusätzlich wurde eine Verschiebung der Resonanzfrequenz hin zu kleineren Frequenzen bei sinkenden Temperaturen festgestellt. Diese Effekte konnten für alle untersuchten Frequenzen beobachtet werden und stimmten mit der Beschreibung der resonanten Absorption von Photonen durch die ZNS im Rahmen des Tunnelmodells überein. Die Untersuchung der Frequenzabhängigkeit der Verluste lieferte eine deutlich erkennbare Frequenzabhängigkeit der Zustandsdichte der ZNS. Obwohl so etwas weder in den Untersuchungen dielektrischer Verluste in Gläsern noch in

den Untersuchungen ZNS basierter Verluste in supraleitenden Mikrowellenresonatoren gesehen worden war, stimmt diese Frequenzabhängigkeit der ZNS Zustandsdichte doch mit Untersuchungen der spezifischen Wärme überein und wird durch das Tunnelmodell nicht ausgeschlossen. Dieses Ergebnis ist von höchster Wichtigkeit für die Qubitforschung, da Qubits in einem Frequenzbereich von 6 - 10 GHz, bei Temperaturen im mK Bereich und bei sehr kleinen Leistungen arbeiten, einem Bereich, der eindeutig von resonanter Absoption dominiert wird. Da nach den vorliegenden Untersuchungen Verluste bei höheren Frequenzen höher sind, was einhergeht mit der entdeckten Frequenzabhängigkeit der ZNS-Zustandsdichte, müsste die Möglichkeit betrachtet werden, Qubits eventuell bei tieferen Frequenzen zu realisieren um Dekohärenz zu reduzieren.

Zukünftig sollte die Frequenzabhängigkeit der ZNS-Zustandsdichte bei weiteren Frequenzen gemessen werden um eine quantitaive Beziehung zwischen Zustandsdichte und Frequenz ableiten zu können. Unter Inbezugnahme der in dieser Arbeit erhaltenen Ergebnisse bei 4.2 K sind die ZNS in allen untersuchten Dielektrika gleichen Ursprungs. Deshalb sollte die Frequenzabhängigkeit der Verluste der übrigen Dielektrika im Qubit-Arbeitsbereich untersucht werden um die Universalität des ZNS Verhaltens in amorphen Dünnschichtfilmen bestätigen zu können.

Contents

Chapter 1

Introduction

In 1971, Zeller and Pohl [1] showed with their pathbreaking investigations that the low-temperature behavior of glasses drastically differs from that of perfect crystals. Even more fascinating was the discovery of almost universal thermal properties among glasses. This caused an increasing interest in the understanding of glasses and glass physics arose to an intensively pushed field of natural science. At that time, the thermal properties of dielectric solids (like glasses) at low temperatures were expected to be determined by phonons of long wavelength. Phonons are characterized by the elastic behavior of the medium averaged over a distance comparable with their wavelength. At temperatures $T < 1$ K, the wavelength of the dominant phonons is a thousand times larger than the interatomic distance. Therefore, no difference between the behavior of glasses with their disordered structure and that of crystals with their regularly constrained lattice was expected [2]. However, observed anomalous phenomena of the specific heat and the thermal conductivity of glasses [3] pointed out to exhibit their origin in the disordered structure. In 1972, independent of each other Anderson [4] and Phillips [5] worked out a theoretical description, which was able to explain the anomalous low-temperature properties of glasses. In this description, defects in amorphous solids were expressed by double well potentials leading to the assumption of two-level systems (TLSs) in the amorphous solids which are able to tunnel through the potential well barriers. Thus, this model was called the *tunneling model*. With the help of this model, the anomalous specific heat of glasses could be deduced from relaxation effects of TLSs with a broad distribution of energy splittings between their levels [6]. Observed nonlinear ultrasonic attenuation [2], dielectric loss [7] as well as variations of the dielectric permittivity and the sound velocity in glasses could be explained by the tunneling model in terms of resonant absorption of phonons or photons by TLSs at very low temperatures.

In very recent times, new interest in the anomalous properties of glasses at low temperatures gained from the field of superconducting quantum engineering. The superconducting phase qubit for instance, has been reported to suffer from two-level tunneling systems

(TLSs) in its vicinity, which couple to the qubit and extract energy from it leading to strong decoherence [8] . In principle, a superconducting phase qubit consists of a superconducting loop interrupted by a Josephson junction (JJ). It was shown that decoherence is stronger if dielectrics with high dielectric losses are used in phase qubit fabrication [8]. This showed that the TLSs responsible for the qubit decoherence and dielectric losses are identical. Consequently, dielectric loss in amorphous thin films was intensively investigated in the last years leading to remarkable results. Investigations with superconducting microwave resonators were able to identify TLSs to be situated in the bulk dielectric materials [9] as well as in thin layers on the surfaces of such devices [10, 11, 12]. These TLSs were shown to be of the same origin as those found in glasses three decades ago, being in perfect agreement with the predictions of the tunneling model [13, 14, 15]. Although a wide understanding of TLS processes in superconducting microwave devices could be established, open questions remained. Especially absolute values of dielectric losses and their dependence on frequency has not been reliably investigated yet. This on the other hand is of great importance for qubit development. According to investigations of dielectric loss in bulk glasses [16] and to recent results in this regard by superconducting microwave devices, the TLS density of states is assumed to be constant in regard to dielectric loss [13, 14]. However, investigations of the specific heat of glasses [3] have figured out that the TLS density of states is indeed frequency dependent.

In this thesis, dielectric losses of various dielectrics commonly used in qubit fabrication will be studied at low temperatures and low excitation energies. An enhanced measurement method using superconducting microwave resonators and a low-temperature microwave setup for a broad frequency range will be developed in order to evaluate absolute values of dielectric loss as well as their dependence on frequency. The is done in order to find useful low-loss dielectrics improving qubit performances. In order to be able to explain the concept of the method and the obtained results of this thesis, the essential theoretical background will be introduced in chapter 2. The tunneling model and its predictions for relaxation and resonant processes of the TLSs will be deduced. As superconducting microresonators will used for the investigations, essential concepts of superconductivity and microwave resonator techniques will be explained in the following. In chapter 3, recent investigations of dielectric losses using sperconducting microwave resonators and their pathbreaking results will be discussed. Furthermore, the relation between these investigations and the presented method will explained. In chapter 4, the resonator design and simulation will be explained in detail, followed by the description of the developed broadband setup for the qubit working regime. The experimental results will be shown and discussed in chapter 5, before concluding in the summary in chapter 6.

Chapter 2

Theoretical background

In the following sections the theoretical concepts essential for the presented measurement method and the interpretation of the obtained data within this thesis will be introduced and explained. As within this thesis dielectric losses in amorphous thin films will be investigated, the concept of two-level tunneling systems in such dielectrics will be introduced and important relations will be deduced from it in the first part of this chapter. As the here presented investigations of the dielectrics employ superconducting microwave resonators, the basics of superconductivity and microwave resonators will be described in the second and third part of this chapter respectively.

2.1 Two-Level Tunneling Systems in Amorphous Dielectrics

In 1971, Zeller and Pohl discovered the universality of the thermal low-temperature properties among glasses and the drastic difference of these properties compared to those of perfect crystals [1]. This caused an increasing interest in the understanding of glasses. Therefore, the investigation of the specific heat and of the acoustic and dielectric properties of amorphous solids was pushed intensively. In contrast to crystals, amorphous solids do not have a long-range order of their atoms. Since their bonding lengths and angles vary, they do not exhibit a well-defined atomic structure. This affects the physical properties of glasses at low temperatures strongly.
In 1972, independent of each other Anderson [4] and Phillips [5] worked out a theoretical description, which was able to explain the anomalous low temperature properties of glasses. This description is based on the assumption of two-level states and is called the *tunneling model*.
In section 2.1.1 these two-level tunneling systems (TLSs) will be introduced. This will be followed by the description of the distribution of the parameters involved in the tunneling model leading to the explanation of the anomalous specific heat of glasses. Afterwards, the coupling of the TLSs to electric field will be deduced in general from the tunneling model.

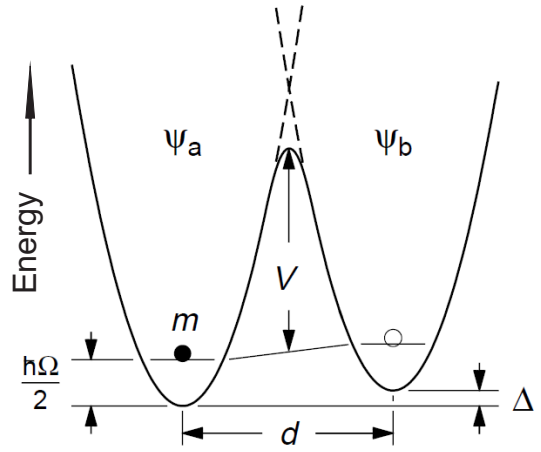

Figure 2.1:
A particle in a double-well potential with asymmetry energy Δ, well distance d, ground state energy $\hbar\Omega/2$ of the particle in an isolated well, and potential barrier V. This figure is taken from [6].

In section 2.1.2 relaxation processes will be discussed, including relaxation absorption, before in section 2.1.3 resonant processes of TLSs will be explained in detail.

2.1.1 Two-Level Tunneling Systems

One of the basic assumptions of the tunneling model is the occurence of configurations of atoms with local adjacent, energetically nearly equal sites of equilibrium in the amorphous structure. Such a configuration can be described by a double well potential. At low temperatures, the thermal energy is not high enough for particles to overcome the potential well barrier, so that only tunneling through the barrier is left. Such double well potentials will now be introduced.

Double Well Potentials

Formally, a two-level tunneling system (TLS) is simply a particle with mass m in a double well potential (see figure 2.1). For reasons of simplicity this potential is composed of two identical, nearly-harmonic wells with ground state energy $\hbar\Omega/2$ as depicted in figure 2.1. Here, $\hbar$ denotes the Planck constant (physical constant reflecting the sizes of quanta in quantum mechanics). For glasses an asymmetry in the depth of the wells with asymmetry energy Δ can be assumed because of their structural disorder. As it can be seen in figure 2.1 d denotes the distance of the two wells.

Starting with two normalized wave functions ψ_a and ψ_b describing the ground state wave functions of the left and the right well, the ansatz $\psi = a\psi_a + b\psi_b$ leads to the solution of the Schrödinger equation $H\psi = E_{\mathrm{H}}\psi$. The energy eigenvalue E_{H} is given by

$$E_{\mathrm{H}} = \frac{\int \psi^* H \psi d^3x}{\int \psi^* \psi d^3x} = \frac{a^2 H_{aa} + b^2 H_{bb} + 2ab H_{ab}}{a^2 + b^2 + 2abS}. \tag{2.1}$$

H_{aa} and H_{bb} are the eigenvalues of the particle in the isolated wells, $S = \int \psi_a^* \psi_b$ describes the overlap of the wave functions and $H_{ab} = \int \psi_a^* H \psi_b d^3x$ the exchange energy.
This expression for the energy can be minimized via $\partial E_{\mathrm{H}}/\partial a = 0$ and $\partial E_{\mathrm{H}}/\partial b = 0$. Thus,

$$(H_{aa} - E_{\mathrm{H}})(H_{bb} - E_{\mathrm{H}}) - (H_{ab} - E_{\mathrm{H}} S)^2 = 0. \tag{2.2}$$

If the middle between the two potentials is chosen as zero energy, one obtains $H_{aa,bb} = (\hbar\Omega \pm \Delta)/2$. Assuming a weak overlap of the wave functions, one can neglect the quantity $E_{\mathrm{H}} S$ and obtains [6]

$$E_{\pm} = \frac{1}{2}\left(\hbar\Omega \pm \sqrt{\Delta^2 + 4H_{ab}^2}\right). \tag{2.3}$$

Here, $\pm$ expresses the symmetric and asymmetric linear combination of ψ_a and ψ_b. This leads to an energy splitting of

$$E = E_+ - E_- = \sqrt{\Delta^2 + 4H_{ab}^2} = \sqrt{\Delta^2 + \Delta_0^2}. \tag{2.4}$$

With the use of the WKB (Wentzel-Kramers-Brillouin) method the *tunnel splitting* Δ_0 can be obtained as $\Delta_0 = -2H_{ab} \approx \hbar\Omega e^{-\lambda}$ with the *tunneling parameter* λ. This parameter is determined by the mass m and the shape of the potential. Under all made approximations, λ is given as $\lambda \approx \frac{d}{2\hbar}\sqrt{2mV}$ [6].

Distributions of the Characteristic Parameters of the Tunneling Model

Due to the irregular structure of glasses the introduced characteristic parameters Δ and λ or Δ and Δ_0 respectively are different for different TLSs. A basic assumption of the tunneling model is, that Δ and λ are independent of each other and that their values are nearly uniformly distributed [5]. This assumption is of phenomenological origin in agreement with experiment. In order to show the consequences of the distributions of Δ and λ, the anomalous specific heat of glasses will be deduced. The interpretation of the origin of the anomalous specific heat will be in close connection to the results of this thesis.

At low temperatures, phonons of long wavelength determine the thermal properties of amorphous dielectrics. The elastic behavior of dielectrics, averaged over a distance similar to this long wavelength, determines the properties of such phonons. Consequently, the atomic disorder was first assumed to be unessential for the low temperature properties of amorphous solids. Thus, non-interacting TLSs in the amorphous dielectrics described by the *Debye model* were used for modelling [17]. In 1971, however, dielectric glasses, amorphous polymers, and superconducting amorphous metals were shown to have almost universal thermal properties and an additional contribution to the total specific heat C_{tot}

at low temperatures besides the expected C_{Debye} deduced with the Debye model [3]

$$C_{\mathrm{tot}} = aT + bT^3 + C_{\mathrm{Debye}}. \tag{2.5}$$

Here, a and b are material dependent constants.
This discovery could be explained by the tunneling model. The simplifying description using a double well potential is plausible as many nearly equivalent wells are unlikely in such distorted structures. The reason for the enhanced specific heat in amorphous solids is the broad distribution of energy splittings of the TLSs. This follows directly out of the broad distribution of asymmetry energy Δ and of the tunneling parameter λ according to (2.4). According to [5], Δ and λ are related like

$$P(\Delta, \lambda)\mathrm{d}\Delta\mathrm{d}\lambda = \mathrm{P}_0\mathrm{d}\Delta\mathrm{d}\lambda. \tag{2.6}$$

Here, P_0 is a constant. By *Jacobian transformation*, one obtains [6]

$$P(E, \Delta_0)\mathrm{dEd}\Delta_0 = \mathrm{P}_0\frac{\mathrm{E}}{\sqrt{\mathrm{E}^2 - \Delta_0^2}}\mathrm{dEd}\Delta_0, \tag{2.7}$$

which gives the relation between the energy splitting E and the tunnel splitting Δ_0. By integrating (2.7) over all values of Δ_0, from a minimum value Δ_0^{min} up to the energy splitting E, the energy dependent density of states $n(E)$ of the TLSs can be obtained as [6]

$$n_{\mathrm{eff}}(E) = \int_{\Delta_0^{\mathrm{min}}}^{E} P(E, \Delta_0)\mathrm{d}\Delta_0 = \mathrm{P}_0 \ln\frac{2\mathrm{E}}{\Delta_0^{\mathrm{min}}}. \tag{2.8}$$

To avoid a nonintegrable divergence of the distribution function for vanishing Δ_0, it was not chosen to be zero but Δ_0^{min} [6].At first, the energy dependence of the density was neglected for theoretical modelling, but soon found to be important for a sufficient description of the specific heat. Additionally, time effects were taken into account, as will be shown in the following.
In section 2.1.2 it will be shown that the relaxation time τ, the typical timescale within a TLS relaxes from its excited state to its ground state, is proportional to (Δ_0/E). Thus, symmetric systems with $(\Delta_0/E) = 1$ exhibit the shortest relaxation time τ_{min} while highly asymmetric systems with $(\Delta_0/E) \to 0$ relax very slowly [6]. Consequently, the relaxation time of an ensemble of TLSs will vary between a minimum value τ_{min} and infinity. According to [6], it can be shown that the relaxation rate is expressed by

$$\tau(E, T) = \left(\frac{E}{\Delta_0}\right)^2 \tau_{\mathrm{min}}(E, T). \tag{2.9}$$

In various experiments [6, 3] it could be shown that the main contribution to the specific heat of glasses is due to TLSs with an energy splitting of $E = k_{\mathrm{B}}T$. According to (2.30),

the relaxation rate is proportional to the energy splitting E like $\tau^{-1} \propto E^3$. Consequently, the minimum relaxation rate for TLSs with $E = k_\mathrm{B}T$ can be given as

$$\tau_{min}^{-1}(E = k_B T) = AT^3. \tag{2.10}$$

Here, A denotes a material dependent proportionality factor.
According to (2.9), a distribution of the tunnel splitting Δ_0 leads to a distribution of the relaxation time. Thus, an expression for the density of states n in relation to τ_min can be obtained in the same way as it was shown for (2.8) [6]:

$$n_\mathrm{eff}(E, t_0) = \frac{P_0}{2} \ln \frac{4t_0}{\tau_\mathrm{min}}, \tag{2.11}$$

Here, t_0 corresponds to the time scale of the experiment. Finally, the additional part in (2.5) due to TLSs besides the expected C_Debye is obtained as [6]

$$C_\mathrm{V} = \frac{\pi^2}{12} P_0 k_B^2 T \ln(4At_0T^3). \tag{2.12}$$

Finally, it is to summarize that two assumptions are essential to describe TLSs based properties of glasses at low temperatures. Firstly, the fact that the characteristic parameters Δ, λ, Δ_0, E and τ are all broadly distributed and secondly, that in principle the density of TLS states is energy dependent, which will be important in the discussion of the results of this thesis.

Coupling to Electric Fields

As this thesis investigates dielectric losses of microwave resonators due to TLSs, the deduction of the coupling of TLSs to electric field is of particular interest and will be discussed in the following.
The unperturbed Hamiltonian of a TLS in the basis (ψ_a, ψ_b) of the normalized wavefunctions can be written in matrix form as

$$H_0 = \frac{1}{2} \begin{pmatrix} \Delta & -\Delta_0 \\ -\Delta_0 & -\Delta \end{pmatrix}. \tag{2.13}$$

Diagonalization supplies the energy description

$$\mathcal{H}_0 = \frac{1}{2} \begin{pmatrix} E & 0 \\ 0 & -E \end{pmatrix}, \tag{2.14}$$

with E denoting the energy splitting of the TLS.
Applying an external electric field to the TLS, normally do not change the shape of the potential, which would have an influence on the separation of the wells as well as their

barrier height and thus, on Δ_0. On th other hand, external perturbations change the environment of the TLS and therewith Δ. Considering these changes as small, one can treat the total Hamiltonian $H = H_0 + H_S$ by first-order perturbation theory with a perturbation Hamiltonian

$$H_S = \frac{1}{2}\begin{pmatrix} \delta\Delta & -\delta\Delta_0 \\ -\delta\Delta_0 & -\delta\Delta \end{pmatrix}. \tag{2.15}$$

Consequently, perturbation theory predicts, that the change in asymmetry energy $\delta\Delta$ will vary linearly with the strength of the electric field [6]

$$\delta\Delta = 2\vec{p}\cdot\vec{F}. \tag{2.16}$$

Here $\vec{p}$ denotes the electric dipole moment and $\vec{F}$ the strength of the applied electric field. Transformation of H_S into the basis of $\mathcal{H}_0$ gives

$$\mathcal{H}_S = \frac{1}{E}\begin{pmatrix} \Delta & -\Delta_0 \\ -\Delta_0 & -\Delta \end{pmatrix}(\vec{p}\cdot\vec{F}), \tag{2.17}$$

in which the diagonal elements describe the influence on the energy splitting by the external electric field, whereas the off-diagonal elements account for the transition between the two levels.

2.1.2 Relaxation Processes

Various low-temperature properties of solids containing defects or structural disorder like glasses evolve from relaxation processes. One example was the anomalous specific heat discussed in section 2.1.1. In the following, relaxation processes of TLSs coupling to electric field will be discussed in detail leading to descriptions which are important for the results within this thesis.

Relaxation

An alternating external electric field modulates the energy splitting (2.4) via coupling to the asymmetry Δ (as shown in (2.17)) like

$$\delta E = 2\vec{p}\cdot\vec{F}\frac{\Delta}{E} \tag{2.18}$$

Here, δE denotes an infinitesimal change of the energy splitting E. The energy splitting on the other hand determines the occupation of the energy levels. At a constant applied electric field, an ensemble of TLSs is in thermal equilibrium. Changing this field drives the states out of equilibrium. By absorption or emission of thermal phonons, which are the

energy quants of a solid structure) the TLSs try to achieve equilibrium again. Once driven out of equilibrium, a TLS needs a characteristic time τ to return. This characteristic time τ was introduced section 2.1.1 as relaxation time.
In the next step, the influence of the electric field on the polarization $\vec{P}$ of a TLS will be discussed. As TLS contribution to the polarization is only a part besides polarization due to the host solid, the TLS contribution will be written as δP. As indicated here, the vectorial character of the polarization contribution and the electric field will be neglected in terms of simplification. In linear approximation, the polarization δP and the electric field F are connected via a response function, which is called susceptibility χ:

$$\delta P = \varepsilon_0 \chi F. \tag{2.19}$$

In this case, ε_0 is the vacuum permittivity.
Assuming an adiabatic change of the electric field in time, thermal equilibrium is maintained. The new equilibrium value of entire polarization P (not only δP) under the influence of the external field is called $\widehat{P}$. This value can be approximated in first-order Taylor expansion [6]

$$\widehat{P} \approx P_0 + \left.\frac{\partial P}{\partial F}\right|_{P_0} \cdot F. \tag{2.20}$$

The second term can be related to the TLS contribution of the polarization δP [6]

$$\delta\widehat{P} \approx \left.\frac{\partial P}{\partial F}\right|_{P_0} F = \varepsilon_0 \widehat{\chi} \cdot F. \tag{2.21}$$

As the change of the alternating field is assumed adiabatic, (2.21) can only be assumed for the quasistatic limit at low frequencies. Thus, $\widehat{\chi}$ is called the *static susceptibility*.
At higher frequencies thermal equilibrium of the TLS will be disturbed non-adiabatically and relaxation effects occur. Thus, a finite value of the relaxation time τ enters the calculations. Via the *relaxation time approximation* the change of polarization δP with time can be given as [6]

$$-\frac{\partial(\delta P)}{\partial t} \approx \frac{\delta P - \delta\widehat{P}}{\tau}. \tag{2.22}$$

It shoul be pointed out that the perturbed system does not relax towards the static equilibrium $\delta P = 0$, but towards the instantaneous equilibrium $\delta\widehat{P}$, which would be reached after waiting a long time in the instantaneous field.
This finite value of τ causes a phase shift between the field and the change of polarization δP, which leads to a *complex susceptibility* $\chi = \chi' + i\chi''$. Assuming a periodically varying field of the form $F = F_0 e^{i\omega t}$ with angular frequency ω and using (2.19) , (2.21) and (2.22) one obtains the following relation for the susceptibility[6]

$$\chi = \frac{\widehat{\chi}}{1 - i\omega\tau}. \tag{2.23}$$

To simplify the discussion, one considers the response of an ensemble of identical TLSs. In thermal equilibrium, these TLSs can assumed to be Boltzmann distributed and the difference in occupation of the two levels can be given according to [18]

$$\Delta N'(E,T) = N'_{\text{ground}} - N'_{\text{excited}} = N' \tanh\left(\frac{E}{2k_{\text{B}}T}\right). \tag{2.24}$$

Here, N'_{ground} denotes the number of TLSs in the lower energy level in the double well potential and hence, N'_{excited} the number of TLSs in the higher energy level. N' denotes the number of all participating TLSs, k_{B} the Boltzmann constant, T the temperature and E the energy splitting.
According to (2.24), $\Delta N'(E,T)$ approaches 0 for $k_{\text{B}}T \gg E$. In this limit, $N'_{\text{ground}} = N'_{\text{excited}}$, i.e. the number of TLSs in both levels is equal. Henceforth, TLSs in this state will be called *saturated*, as there is enough energy available to saturate both levels equally. With decreasing temperature, $\Delta N'(E,T)$ will start to increase. When the temperature approaches $T \approx E/k_{\text{B}}$, the increase will become strong until the temperature reaches $T \approx E/2k_{\text{B}}$, at which all TLSs will be in the ground state, because thermal energy is not any longer enough to overcome the energy splitting.

As soon as an external electric field is applied, the the TLSs (electric dipoles) will align partially. This leads to a change of the energy splitting and thus, to a change $\delta(\Delta N')$ in the population of the two levels [6]. A further simplification is the either parallel or antiparallel alignment of the dipole moments to the electric field. Therefore, one can write $\delta P = \delta(\Delta N') \cdot p_{\text{eff}}$ with $p_{\text{eff}} = p\Delta/E$. The static susceptibility can now be written using (2.21) [6]

$$\widehat{\chi} = \frac{\partial(\delta P)}{\partial(\Delta N')}\frac{\partial(\Delta N')}{\partial E}\frac{\partial E}{\partial F} = \vec{p}\frac{\Delta}{E}(-2N')\frac{\partial f}{\partial E}2\vec{p}\frac{\Delta}{E}. \tag{2.25}$$

In this expression, the derivative of the Fermi-Dirac distribution $f = (e^{E/k_BT}+1)^{-1}$ was introduced. A physical measurand directly connected to the susceptibility χ is the dielectric permittivity ε:

$$\varepsilon = \varepsilon' + i\varepsilon'' = 1 + \chi. \tag{2.26}$$

Using (2.23), (2.25) and (2.26) one can achieve an expression for the variation of the dielectric permittivity

$$\delta\varepsilon' = \frac{-4Np^2}{\varepsilon_0}\left(\frac{\Delta}{E}\right)^2\frac{\partial f}{\partial E}\frac{1}{1+(\omega\tau)^2}, \tag{2.27}$$

as well as for the dielectric loss

$$\tan\delta = \frac{\varepsilon''}{\varepsilon'} = \frac{-4Np^2}{\varepsilon_0\varepsilon'}\left(\frac{\Delta}{E}\right)^2\frac{\partial f}{\partial E}\frac{\omega\tau}{1+(\omega\tau)^2}. \tag{2.28}$$

Here, N denotes for the number of TLSs per unit volume. The typical behavior of these two so called *Debye relaxators* can be seen in figure 2.2.

It is characteristic for these relaxators that the maximum contributions of the TLSs to the

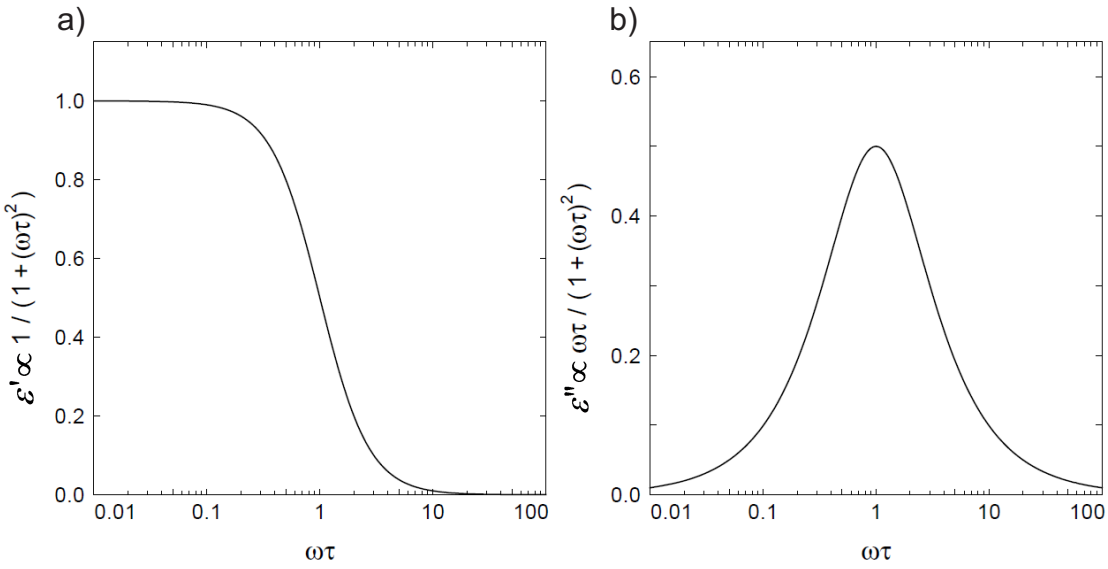

Figure 2.2:
Response ε of a Debye relaxator vs. $\omega\tau$. **a)** Real part with an inflection point at $\omega\tau = 1$. **b)** Imaginary part with a maximum at $\omega\tau = 1$. This figure is taken from [6].

change of the dielectric constant as well as to the dielectric loss appear at $\omega\tau = 1$. Systems with $\omega\tau \ll 1$ are in phase with the applied electric wave because of their short relaxation times while systems with $\omega\tau \gg 1$ are too slow to be able to follow the perturbation.
It has to be mentioned that here presented equations were derived under the assumption of identical TLSs. However, in amorphous solids like glasses a broad distribution of TLS exhibiting a broad distribution of energy splittings has to be taken into account. This will be discussed in the following sections.

Relaxation Times

As it was shown in section 2.1.1 as well as in the previous section, relaxation effects play an important role for the low temperature properties of amorphous solids. In the following, a process will be discussed allowing a TLS to relax from its excited state into its ground state.
At low temperatures, where thermal energy $k_\mathrm{B}T$ is comparable to the energy splitting E, absorption or emission of single phonons can induce transitions between the levels. As there always only one phonon participates, this process is called *one-phonon* or *direct process*. This process can be calculated by *Fermi's Golden Rule* [6]

$$W_{12} = \frac{2\pi}{\hbar}|\langle\psi_b|\mathcal{H}_S|\psi_a\rangle|^2 D(E) f(E) \delta(\hbar\omega = E), \tag{2.29}$$

in which $D(E)$ describes the phonon density of states, $f(E)$ the Bose-Einstein distribution function, $\psi_{a,b}$ the wavefunctions introduced in section 2.1.1 and ω the frequency of the photons of the applied field, equal to $E/\hbar$. For the case of low temperatures the relaxation rate is proportional to [6]

$$\tau^{-1} \approx \left(\frac{\Delta_0}{E}\right)^2 E^3 \coth\left(\frac{E}{2k_B T}\right). \tag{2.30}$$

The temperature dependence of the relaxation rate is given in the last term, describing the thermal phonon occupation.
As it was shown in section 2.1.1, this result for the relaxation rate is capable to explain the anomalous specific heat of glasses at low temperatures.

Relaxation Absorption

The mathematical expressions in the beginning of section 2.1.2 were deduced for identical TLS. For amorphous solids like glasses, however, the broad distributions of the characteristic parameters deduced in section 2.1.1 have to be taken into account in order to deduce the dielectric properties of glasses at low temperatures. For relaxation processes at low temperatures only the one-phonon process introduced in the previous section will be considered.
Usually, in measurements of dielectric losses or dielectric permittivity (like in this thesis) the measurement frequency is kept constant while loss or permittivity are measured over temperature or power. Due to the distribution of the energy splitting E in glasses, the main contribution to this measurements arise from TLss with $E = k_B T$. This was discussed in section 2.1.1. Furthermore, the distribution of the relaxation times or rates (see (2.30)) respectively has to be taken into account.
Thus, in (2.28) the number of relaxing systems N has to be replaced by the integration over all systems, whose spectral distribution function is given by (2.7). Concentrating on the low temperature range, we assume that the one-phonon process is the only one allowing the return to equilibrium. As shown above, for fixed energy splitting and temperature relaxation rate is $\tau^{-1} \approx (\Delta_0/E)^2$.
According to (2.9) various relaxation rates exist for a broad distribution of Δ_0. Taking $\omega\tau = 1$ as condition for maximal absorption, the absorption of TLSs with fixed energy splitting due to relaxation will pass through a maximum over temperature (see figure 2.2b). As in glasses the energy splittings are broadly distributed, there will always be systems fulfilling the condition for maximum absorption. The superposition of all these systems causes a strong absorption at any temperature. The relaxation times of any of these TLSs with a certain energy splitting are distributed. The systems with $\Delta_0/E = 1$ (symmetric systems, see section 2.1.1) exhibit the minimum relaxation time $\tau_{\min}$. Thus, the condition

$\omega\tau_{\min} = 1$ separates the temperature dependence of the dielectric loss into two parts.
$T < T(\omega\tau_{\min} = 1)$:
Only the fastest systems with $E = \Delta_0$ contribute to the dielectric loss $\tan\delta$

$$\tan\delta \propto \alpha\frac{T^3}{\omega}, \tag{2.31}$$

with the macroscopic coupling constant

$$\alpha = \frac{\pi n p^2}{3\varepsilon_0\varepsilon_r}. \tag{2.32}$$

$T > T(\omega\tau_{\min} = 1)$:
There are always systems with $\omega\tau = 1$ and these systems are assumed to have the main contribution to the dielectric loss

$$\tan\delta = \frac{\pi}{2}\alpha. \tag{2.33}$$

For the change of the dielectric permittivity, the following behavior can be derived:

$T < T(\omega\tau_{\min} = 1)$:
In this limit, the TLSs are too slow and do not contribute to the change of the dielectric permittivity.

$T > T(\omega\tau_{\min} = 1)$:
Here, one can find the contribution of the relaxation process to the change of the dielectric permittivity as

$$\left.\frac{\Delta\varepsilon}{\varepsilon}\right|_{\text{rel}} = \frac{3}{2}\alpha\ln\left(\frac{T}{T_0}\right). \tag{2.34}$$

Spectral Dielectric Response due to Relaxation

As it was discussed in the previous section, measurements of dielectric loss or dielectric permittivity are usually done at a fixed frequency investigating temperature or power dependence. But as the measurement method presented in this thesis is capable of doing these measurements over a broad range of frequencies, the frequency dependence of losses due to relaxation processes can be investigated as well. In the following section, this frequency dependence will be considered in more detail and a *universal law* will be deduced describing this dependence for a wide range of materials including amorphous dielectrics.
In various measurements [19, 20] the response of materials on a harmonically varying applied field was investigated as described in the previous sections. As introduced in

the beginning of section 2.1.2, the response can be expressed in terms of the complex susceptibility $\chi(\omega) = \chi'(\omega) + i\chi''(\omega)$ of the real frequency variable $\omega = 2\pi f$.
The response $\chi(\omega)$ was already given as (2.23). According to figure 2.2b) the condition for maximum absorption $\omega\tau = 1$ can be taken to define the *loss peak frequency* $\omega_\mathrm{p} = 1/\tau$, with which (2.23) can be written as

$$\tilde{\chi}(\omega) = \frac{\widehat{\chi}}{1 - i\omega/\omega_p}. \tag{2.35}$$

The same expression was derived in 1912 by Debye [17], assuming non-interacting ideal dipoles to cause this frequency behavior. This is why (2.27) and (2.28) are called Debye relaxators; they were derived for single non-interacting TLSs. But as it was shown in sections 2.1.1 and 2.1.2, in order to explain the anomalous low temperature phenomena of glasses, it is necessary to take the interaction between the TLSs into account. In the tunneling model this is realized by relations between the characteristic parameters, like in (2.6) and (2.7).
Additionally, it shall be mentioned that a wide range of experimental results in the last three decades led to the conclusion that pure Debeye behavior is hardly ever found in nature [21]. Instead, one can distinguish two fundamentally different types of dielectric responses based on interacting systems, namely *dipolar* and *charge carrier* responses. Using the *loss peak* term, one can describe dipolar polarization to leave zero residual polarization after discharging equivalent to reversible systems exhibiting loss peaks. Charge carriers on the other hand give a partial recovery after discharge but typically leave a finite polarization in the system. The corresponding systems are irreversible systems without loss peaks but instead continuing rise of $\chi'(\omega)$ and $\chi''(\omega)$ for decreasing frequencies [21]. These behaviors can be seen in figure 2.3.

General Dipolar Responses

As the measurement results at 4.2 K can be explained by dipolar behavior of the TLSs, dipolar responses will be discussed in the following in detail. As charge hopping effects are not visible in the measurements within this thesis and as they cover a wide range of phenomena, they will be not discussed (a reader interested in hopping transport in solids may read [22]).

The frequency dependence of the dielectric responses for dipoles can be expressed in form of *fractional power laws* [21]. In figure 2.3 (for dipoles), one finds on the left side of the peak with $\omega \ll \omega_\mathrm{p}$

$$\chi'' \propto \omega^m, \tag{2.36}$$

while on the right side with $\omega \gg \omega_\mathrm{p}$,

$$\chi'' \propto \omega^{n-1}. \tag{2.37}$$

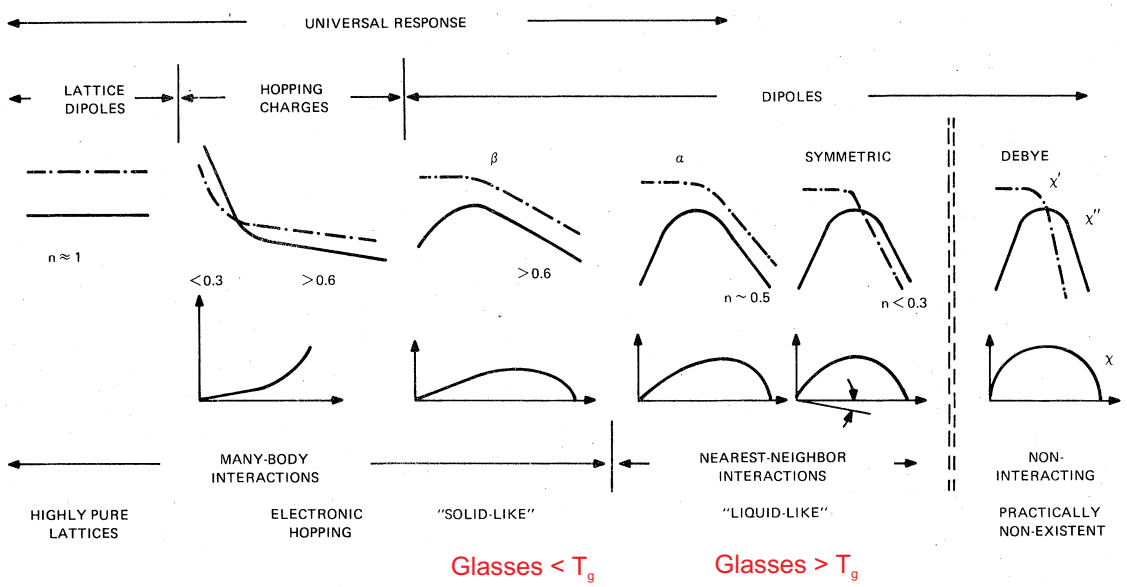

Figure 2.3:
Schematic representation of the various observed types of dielectric response for various types of solids. The upper set of diagrams represent the shapes of the logarithmic plots of $\chi'(\omega)$ - chain dotted lines, and $\chi''(\omega)$ - solid lines, ranging from the ideal Debye shape on the right dipolar loss peak shapes (see text) and peakless hopping shapes on to flat shape in the case of highly pure lattices. The limiting forms of behavior are the strong low-frequency dispersion with small values of n and the case of frequency-independent "lattice response" with $n \approx 1$. The lower set of graphs represent the corresponding complex χ plots. Written in red, glasses below and above the glass transition temperature T_g are emphasized. This schematic is taken from [23].

Here, the exponents m and n are in the range $(0, 1)$. This fractional power laws are commonly known as *universal law*, because they can be found for a wide range of materials [21].

A value of $n \approx 0.5$ can be found for dipoles with nearest-neighbor interaction. Many-body interacting dipoles instead exhibit a value of $n > 0.6$, while many-body interacting hopping charges (in the left part of figure 2.3) have either $n < 0.3$ or $n > 0.6$.

A convenient representation of these generalized loss peaks can be given by [24]

$$\chi'' \propto [1 + (i\omega/\omega_p)^m]^{(n-1)/m}. \tag{2.38}$$

In dipolar materials below the *glass transition temperature* T_g (the temperature at which the glass-to-crystalline transition takes place), the loss peaks are broader and their temperature dependence follows a *Vogel-Fulcher law* [25, 26]

$$\omega_p \propto \frac{1}{T - T_0}, \tag{2.39}$$

with a characteristic temperature T_0. Above T_g, the peaks are narrower and the loss peak frequency follows the *Arrhenius* temperature dependence [27]

$$\omega_p \propto \exp\left(\frac{-W}{k_B T}\right). \tag{2.40}$$

Here, W denotes an activation energy. T_g usually is of the order of 10^2 K.

Low-Loss Materials

Considering the spectral behavior of materials with low loss, very flat spectral responses are expected. The reason is that their $\chi'(\omega)$ and $\chi''(\omega)$ are independent of frequency. Especially in the limit $n \to 0$ for dipoles in highly pure lattices (see fig. 2.3 on the left) (equivalent to low loss) such flat spectral behavior can be found.

2.1.3 Resonant Processes

After the detailed discussion of relaxation processes in amorphous solids within the previous sections, resonant processes will be discussed in the following section. At very low temperatures and energies resonant interaction between the TLSs and an applied electric field is the most dominating process in amorphous dielectrics. At first in this section, the general descriptions of loss and change of the dielectric permittivity due to an resonant interacting TLS will be deduced, before the resonant absorption of interacting TLSs in amorphous materials will be derived.

Resonant Interaction

In resonant processes induced transitions can be separated into two cases: absorption of a photon, leading to an excitation of the TLS from ground to excited state and emission of a photon stimulated by another photon leading to a transition from the excited to ground state. Absorption and induced emission are essentially parts of the same process. Again, Fermi's Golden Rule helps to calculate the transition probability. Since the density of the final states is strongly influencing this process, the Lorentzian line function

$$g(\omega) = \frac{\tau}{\pi} \frac{1}{1 + (\omega - \omega_0)^2 \tau_2^2} \tag{2.41}$$

is helpful as it gives the *spectral function* for the upper level [6]. It has its maximum at ω_0, with width τ_2^{-1}, and maximum height $g(\omega_0) = \tau_2/\pi$. Considering absorption and induced emission, for the dielectric loss one obtains [6]

$$\tan\delta = \frac{Np^2}{\varepsilon_0 \varepsilon'} \left(\frac{\Delta_0}{E}\right)^2 \frac{\pi\omega}{\hbar} g(\omega) \tanh\left(\frac{E}{2k_B T}\right). \tag{2.42}$$

Again, N denotes the number of TLSs per unit volume, p the dipole moment of the TLSs and Δ_0 and E their tunnel and energy splitting. As it was discussed for (2.28), (2.42) does not take the interaction of the TLSs into account. This will be done in the following section.

Resonant Absorption

As it was discussed in the previous section the resonant absorption is an important mechanism dealing with solids at low temperatures. In this section the resonant interaction of TLSs in glasses with electric fields will be deduced. Analogous to section 2.1.2, the distributions of the characteristic parameters of the tunneling model, which where deduced in section 2.1.1, have to be taken into account in order to introduce the interaction of the TLSs.
If the change of Δ and Δ_0 can be considered small (as it was discussed in section 2.1.1), the case of *weak fields* can be assumed. This gives the possibility of treating the Hamiltonian of the system with first-order perturbation theory. It means that one can neglect the phase relationship of the wavefunctions introduced in section 2.1.1 [6]. In this low-temperature regime photons interact resonantly with TLSs with the energy splitting $E = \hbar\omega$. To get the corresponding formula, $N \cdot g(\omega)$ in (2.42) has to be replaced by the distribution function $P(E, \Delta_0)$ (see (2.7)). Then, one has to integrate over all Δ_0 and gets

$$\tan\delta = \alpha\omega \tanh\left(\frac{\hbar\omega}{2k_BT}\right), \tag{2.43}$$

with the same α (see (2.32)) deduced in section 2.1.2 [6]. Here, $\tan\delta$ is defined as loss rate in the units of Hz.
(2.43) predicts an increase of loss due to the difference in occupation number of the levels, which goes with $\tanh(1/T)$ (this was shown in section 2.1.2 with (2.24)). The absorption of photons by the TLSs is proportional to the occupation number. The more TLSs are present in the ground state the more photons can be absorbed to excite them. Thus, the absorption increases with increasing occupation number, which increases with decreasing temperature. This causes increasing loss for decreasing temperatures. It was predicted by [16] that TLSs with an energy splitting E (see (2.4)) equal to the energy of the photons from the applied field at resonance contribute most. This leads to $\hbar\omega = hf_0$ in the numerator of the hyperbolic tangent. As long as the condition $k_BT < hf_0$ is fulfilled while cooling down, resonant absorption is the dominating process leading to increasing loss for decreasing temperature. If the temperature becomes so low that all TLSs are in the ground state, the loss reaches its maximum. For even lower temperatures, the loss stays at this maximum level as the number of TLSs in the ground state does not change. On the other hand, as soon as $k_BT \geq hf_0$, TLSs will be saturated thermally. This means that the available thermal energy is enough to overcome the energy splitting. As soon as TLSs are saturated,

resonant absorption may still take place, but is clearly dominated by relaxation processes. According to (2.26) and (2.28), $\tan\delta$ follows out of χ''. With the help of the *Kramers-Kronig relations* [28, 29]

$$\chi'(\omega) = \frac{1}{\pi}\int_{-\infty}^{\infty}\frac{\chi''(\tilde{\omega})}{\tilde{\omega}-\omega}d\tilde{\omega}, \tag{2.44}$$

one can deduce the change in the dielectric permittivity out of the expression for dielectric loss [30, 16]:

$$\begin{aligned}\frac{\Delta\varepsilon}{\varepsilon} &= \frac{\varepsilon_{\mathrm{r}}(T)-\varepsilon_{\mathrm{r}}(T_0)}{\varepsilon_{\mathrm{r}}(T_0)} \\ &= -\frac{2\alpha}{\pi}\left[\ln\left(\frac{T}{T_0}\right) - \left(\mathrm{Re}\,\psi\left(\frac{1}{2}+\frac{\hbar\omega}{2\pi i k_{\mathrm{B}}T}\right) - \mathrm{Re}\,\psi\left(\frac{1}{2}+\frac{\hbar\omega}{2\pi i k_{\mathrm{B}}T_0}\right)\right)\right].\end{aligned} \tag{2.45}$$

T_0 denotes a reference temperature and ψ is the *complex digamma function* [31].
For $T_0 = 0$ one obtains

$$\frac{\varepsilon_{\mathrm{r}}(T)-\varepsilon_{\mathrm{r}}(T_0=0)}{\varepsilon_{\mathrm{r}}(T_0=0)} = -\frac{2\alpha}{\pi}\left[\mathrm{Re}\,\psi\left(\frac{1}{2}+\frac{\hbar\omega}{2\pi i k_{\mathrm{B}}T}\right) - \ln\left(\frac{\hbar\omega}{k_{\mathrm{B}}T}\right)\right]. \tag{2.46}$$

The complex digamma function becomes significant only for $k_BT \lesssim \hbar\omega/2$.
In the case $\hbar\omega \ll k_BT$, referring again to a temperature T_0, it is sufficient to write [30]

$$\frac{\varepsilon_{\mathrm{r}}(T)-\varepsilon_{\mathrm{r}}(T_0)}{\varepsilon_{\mathrm{r}}(T_0)} = -\frac{2\alpha}{\pi}\ln\left(\frac{T}{T_0}\right). \tag{2.47}$$

The advantage of equations (2.45) - (2.47) is the insensitivity to the strength of the electric field. The reason for this is that the main contribution to the Kramers-Kronig integral comes from states for which $\hbar\omega/k_{\mathrm{B}}T$ is close to unity, and which are therefore much more difficult to saturate than those with $\hbar\omega \ll k_BT$. This fact leads to the conclusion that the TLSs sampled in a $\Delta\varepsilon$ measurement at frequency ω have a larger energy splitting than those probed in loss measurements at the same frequency. Values of np^2 derived from these two experiments need not to be identical if n is energy dependent. In the deduced formula (2.32) for the resonant absorption, n is assumed energy independent [30].

In the case of *strong electric fields*, the phase coherence between the wavefunctions introduced in section 2.1.1 cannot be neglected any longer. Therefore, one has to introduce an additional spectral function in order to describe the dynamics of the system [30]:

$$h(\omega) = \frac{1+(\omega_0-\omega)\tau_2^2}{1+\Omega^2\tau_1\tau_2+(\omega_0-\omega)^2\tau_2^2}. \tag{2.48}$$

Here, ω is the rf frequency, while ω_0 is the resonance frequency . τ_2 is the same as in section 2.1.3 and is called the *phase decoherence lifetime* or *dephasing time*. τ_1 is the

energy relaxation lifetime, named τ in section 2.1.2. Ω denotes the Rabi frequency. The Rabi frequency is the frequency of the oscillation the population of TLSs between ground and excited state in the applied field. Since the Rabi frequency is proportional to the strength E_{el} of the applied field, $(1 + \Omega^2\tau_1\tau_2)$ is typically cast as $(1 + E_{\mathrm{el}}^2/E_{\mathrm{el,c}}^2)$. This can also by expressed in terms of the applied power leading to $(1 + P/P_c)$. The detailed deduction of this relationship can be found in [30].
For the dielectric loss, this means an additional power dependent factor [30]

$$\tan\delta = \alpha\omega \left(1 + \frac{P}{P_c}\right)^{-\frac{1}{2}} \tanh\left(\frac{\hbar\omega}{2k_BT}\right), \tag{2.49}$$

with the condition

$$\frac{P}{P_c} = \frac{(2\vec{p}\cdot\vec{F})^2}{\hbar^2}\tau_1\tau_2. \tag{2.50}$$

Here, $\tan\delta$ is defined as loss rate in the units of Hz.
For (2.49) the same temperature dependence is predicted as discussed for (2.43) and $\hbar\omega = hf_0$ is also valid. At temperatures $T < 1$ K, (2.49) predicts that as soon as a certain power is went below, TLSs cannot be saturated any longer by power. Saturation in regard to power means that ground as well as excited states are occupied equally, because the energy applied in form of electric power of the applied field is high enough to overcome the energy splitting. In the case for very low powers, the loss will reach a maximum value as soon as the power becomes so low that all TLSs are in the ground state. This is the same as for saturation by thermal energy which was described above. As soon as TLSs are saturated (either by thermal energy or by power or by both of them), resonant absorption may still take place, but is clearly dominated by relaxation processes.
Within this thesis the resonant absorption is an important concept essential in order to explain the measurement data at $T < 1$ K.

2.2 Superconductivity

In the first part of the following section, the basic concepts of superconductivity will be discussed in order to give a short explanation why superconductors are so useful for this field of research. The use of superconducting microwave devices needs a further consideration of the high frequency behavior of superconductors. This will be the topic of the second part of this section.

2.2.1 Basic Concepts

In 1911, H. Kamerlingh Onnes discovered superconductivity [32]. Three years after he had liquefied helium for the first time, he cooled down various different metals to investigate the temperature dependence of their electrical resistance. He observed that for some metals like lead or tin, the resistance disappeared below a critical temperature T_C. This phenomenon was named *superconductivity*. A further effect was discovered in 1933, when Meissner and Ochsenfeld found superconductors to be perfect diamagnets [33]. On the one hand a magnetic field cannot enter a superconductor while it is below T_C, on the other hand a field penetrating a superconductor in its normal state is expelled when the superconductor is cooled down below T_C. The first effect can be explained by the perfect conductivity of the superconductor, but the second one can only be explained by if the superconducting state is a new thermodynamic phase. For a superconductor, this means that it looses superconductivity not only above a critical temperature T_C, but also above a critical magnetic field H_C. Empirically, the relation between T_C and H_C can be given by [34]

$$H_\mathrm{C}(T) \approx H_\mathrm{C}(T=0)[1-(T/T_\mathrm{C})^2]. \tag{2.51}$$

In 1935, F. and H. London were able to describe the effects of perfect conductivity and ideal diamagnetism by introducing two equations for the microscopic electrical and magnetic fields [35]

$$\vec{E} = \partial_t(\Lambda \vec{J}_\mathrm{s}), \tag{2.52}$$

$$\vec{B} = -\mathrm{rot}(\Lambda \vec{J}_\mathrm{s}), \tag{2.53}$$

with the phenomenological parameter

$$\Lambda = \frac{m}{n_\mathrm{s} e^2}. \tag{2.54}$$

Here, $\vec{J}_\mathrm{s}$ denotes the current density, m and e the electron mass and charge and n_s the density of superconducting charge carriers. The first equation describes the acceleration of superconducting charge carriers by an electrical field without any resistance, equivalent

to a perfect conductivity. If the second equation is combined with the Maxwell equation $\mathrm{rot}\vec{B} = \mu_0\vec{J}$ (μ_0 being the vacuum permeability) this leads to

$$\nabla^2\vec{B} = \frac{\vec{B}}{\lambda_\mathrm{L}^2}, \tag{2.55}$$

with the London penetration depth

$$\lambda_\mathrm{L} = \sqrt{\frac{m}{\mu_0 n_\mathrm{s} e^2}}. \tag{2.56}$$

This shows that a magnetic field is exponentially screened out of the interior of the superconductor below T_C, as Meissner and Ochsenfeld had found two years before. As it is indicated here by relating the superconducting charge carriers to e, in 1957, Bardeen, Cooper and Schrieffer showed with their pairing theory (BCS theory), that a weak attractive interaction between electrons leads to the formation of bound pairs of them. These *Cooper pairs* are the superconducting charge carriers, and with the BCS theory superconductivity was described microscopically for the first time. One prediction of this theory was a minimum energy which is required to break a Cooper pair: $E_\mathrm{g}(0) = 2\Delta(0)$. $\Delta(0)$ denotes the energy gap for one electron between superconducting and normal state.

2.2.2 High-Frequency Electrodynamics in Superconductors

While superconductors show zero dc resistance below T_C, high-frequency ac currents cause measurable impedance in the superconductor even below T_C. A time-varying applied electric field affects on the superconducting Cooper pairs as well as the normal conducting electrons, which are not paired. On the one hand the scatter of the steady-accelerated and decelerated electrons from impurities in the superconductor causes resistance, described by Ohm's law

$$\vec{J}_\mathrm{n} = \sigma_1 \cdot \vec{E}. \tag{2.57}$$

Here, σ_1 denotes for the conductivity of the normal electrons. But on the other hand the Cooper pairs are accelerated and decelerated as well. As they exhibit mass they are inertial which causes inductance. As this inductance is connected with the motion of Cooper pairs it is called kinetic inductance. A superconductor can then be modeled as a parallel circuit consisting of one branch with the resistance and the inductance of the unpaired electrons in series and of another branch with the kinetic inductance of the Cooper pairs. Thus, when kinetic inductance increases, the influence of the electron resistance (2.57) carries more and more weight and the superconductivity gets reduced.

Two-Fluid Approximation

If one assumes the total charge carrier density n to consist of the density of superconducting electrons n_s and the density of normal electrons n_n, a superconductor can be described by a *two-fluid model* [36]. In this model, the total current density can be expressed as

$$\vec{J} = \vec{J}_\mathrm{n} + \vec{J}_\mathrm{s} = \sigma_1 \cdot \vec{E} + \frac{1}{i\omega\mu_0\lambda_\mathrm{L}} \cdot \vec{E} = \underline{\sigma} \cdot \vec{E}. \tag{2.58}$$

Here, $\underline{\sigma}$ denotes the complex conductivity. In this case it is assumed that the time-dependence of the applied electrical field is sinusoidal with frequency ω

$$\vec{E} = \vec{E}_0 \exp(i\omega t). \tag{2.59}$$

The complex conductivity is then given by

$$\underline{\sigma} = \sigma_\mathrm{n}\frac{n_\mathrm{n}}{n} - i\frac{1}{\omega\mu_0\lambda_\mathrm{L}} = \sigma_1 + i\sigma_2. \tag{2.60}$$

High-Frequency Dissipation

The dissipative effect caused by a high-frequency ac field can be expressed by the surface impedance Z_s of a superconductor. The propagation constant of an electromagnetic wave in a medium, which is a measure of the change undergone by the amplitude of the wave as it propagates in a given direction, with conductivity $\underline{\sigma}$ can be written as [37]

$$\underline{\gamma}_0 = \sqrt{i\omega\mu_0\underline{\sigma}}. \tag{2.61}$$

For frequencies ω smaller than the BCS energy gap, i.e. $\omega < \frac{\Delta(0)}{\hbar}$, which usually means $\omega < 10^{11} - 10^{12}$ Hz and for $T < T_\mathrm{c}$, the propagation constant in a superconductor is given by $\underline{\gamma}_0 \approx 1/\lambda_\mathrm{L}$. The complex surface impedance is defined as the ratio of the tangential electrical field strength to the tangential magnetic field strength on the surface [37], i.e.

$$\underline{Z}_\mathrm{s} = \frac{E_\mathrm{t}}{H_\mathrm{t}} = R_\mathrm{s} + iX_\mathrm{s} = \frac{i\omega\mu_0}{\underline{\gamma}_0}. \tag{2.62}$$

The surface reactance X_s describes the penetration of an electromagnetic wave into the surface of a superconductor and is proportional to the London penetration depth λ_L.
The more important part of the surface impedance is the surface resistance R_s, which is given approximately by [37]

$$R_\mathrm{s} \approx \frac{1}{2}\mu_0^2\sigma_1\lambda_\mathrm{L}^3\omega^2, \tag{2.63}$$

and explains the losses in the superconductor at a high-frequency ac field.

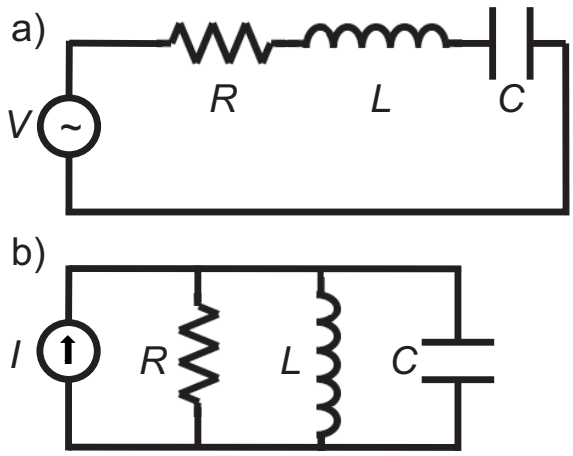

Figure 2.4:
Schematics of an RLC circuit.
a) In series. **b)** In parallel.

2.3 Superconducting Microwave Resonators

In the following section, the influences of dielectric losses on microwave circuits will be studied. With superconducting microwave resonators, dielectric losses in different amorphous materials, their dependences on processing, frequency, electric field and temperature can be analyzed. Firstly, the basics of microwave resonators will be deduced, different types of losses will be introduced and two important types of such resonators will be presented.

2.3.1 Microwave Resonators

In order to deduce the basic properties of a microwave resonator, the electric components of the resonator are considered to be physically very small in relation to the electrical wavelength. Thus, even distributed resonators can be modeled by an equivalent RLC lumped-element circuit.

Series Resonant Circuits

The input impedance of a series RLC resonant circuit (see figure 2.4a) consists of the resistance R and the reactance X as

$$Z_{\text{in}} = R + X = R + i\left(\omega L - \frac{1}{\omega C}\right), \tag{2.64}$$

where ω denotes the frequency, L the inductance and C the capacitance of the resonant circuit.

Since the current I through all elements is equal, the complex power delivered to the resonator can be given as

$$P_{\text{in}} = \frac{1}{2}Z_{\text{in}}|I|^2 = \frac{1}{2}|I|^2\left(R + i\left(\omega L - \frac{1}{\omega C}\right)\right). \tag{2.65}$$

The first term of the power expresses the dissipation by the resistor:

$$P_{\text{loss}} = \frac{1}{2}|I|^2 R, \tag{2.66}$$

while the average magnetic energy stored in the inductor is given by

$$W_{\text{m}} = \frac{1}{2}|I|^2 L, \tag{2.67}$$

and the average electric energy stored in the capacitor is given by

$$W_{\text{e}} = \frac{1}{2}|I|^2 \frac{1}{\omega^2 C}. \tag{2.68}$$

Equation (2.65) can now be written as

$$P_{\text{in}} = P_{\text{loss}} + 2i\omega(W_{\text{m}} - W_{\text{e}}). \tag{2.69}$$

In the case of resonance, $W_{\text{m}} = W_{\text{e}}$, the input resonance Z_{in} gets minimal and the the resonance frequency is defined as

$$f_0 = \frac{1}{2\pi}\omega_0 = \frac{1}{2\pi\sqrt{LC}}. \tag{2.70}$$

Parallel Resonant Cicuits

Figure 2.4b shows the schematic of a parallel lumped-element circuit. The input impedance in this case is given as

$$Z_{\text{in}} = \left(\frac{1}{R} - \frac{i}{\omega L} + i\omega C\right)^{-1}. \tag{2.71}$$

Since in a parallel circuit the voltage V across all elements is equal, the complex power can be written as

$$P_{\text{in}} = \frac{1}{2}Z_{\text{in}}|I|^2 = \frac{1}{2}|V|^2 \frac{1}{Z_{\text{in}}^*} = \frac{1}{2}|V|^2 \left(\frac{1}{R} + \frac{i}{\omega L} - i\omega C\right). \tag{2.72}$$

The dissipated power is then

$$P_{\text{loss}} = \frac{1}{2}|V|^2/R, \tag{2.73}$$

and the average electric and magnetic energies are

$$W_{\text{e}} = \frac{1}{4}|V|^2 C, \tag{2.74}$$

$$W_{\text{m}} = \frac{1}{4}|V|^2 \frac{1}{\omega^2 L}. \tag{2.75}$$

Thus, the power can also be written as (2.69), which leads in the resonant case $W_\mathrm{m} = W_\mathrm{e}$ to the same resonace frequency

$$f_0 = \frac{1}{2\pi}\omega_0 = \frac{1}{2\pi\sqrt{LC}}. \tag{2.76}$$

2.3.2 Quality Factors and Losses

The *quality factor* Q_0 of a resonant circuit is defined as

$$Q_0 = \omega\frac{(\text{average energy stored})}{(\text{energy loss/second})} = \omega\frac{W_\mathrm{m} + W_\mathrm{e}}{P_\mathrm{loss}}. \tag{2.77}$$

At resonance $W_\mathrm{m} = W_\mathrm{e}$, this leads to the following expressions for the loss

$$Q_0 = \begin{cases} \frac{1}{\omega_0 RC} & \text{for series circuits,} \\ \omega_0 RC & \text{for parallel circuits.} \end{cases} \tag{2.78}$$

The quality factor Q_0 introduced here is not influenced by any loading effects caused by external circuitry. This means that it is an intrinsic characteristic of the resonator itself, so that it is called the *unloaded quality factor* Q_0.
In order to calculate the loss in a resonator, one has to use the angle δ between the imaginary part X of the complex impedance Z and the impedance itself in the complex plane. The tangent of this *loss angle* is defined as $\tan\delta_\mathrm{tot} = \frac{R}{X}$, ratio of the real part R of the complex impedance to the imaginary one X. This ratio is called the *loss tangent* of a resonator. This loss tangent is directly connected to the unloaded quality factor Q_0 by the relation

$$\tan\delta_\mathrm{tot} = \frac{1}{Q_0}. \tag{2.79}$$

Now, the behavior at frequencies $\omega = \omega_0 + \Delta\omega$ close to resonance (i.e. $\Delta\omega \ll \omega_0$) will be considered. In a series circuit, the complex impedance can then be approximated as [38]

$$Z_\mathrm{in} \cong R + iRQ_0\frac{2\Delta\omega}{\omega_0} = R + iRQ_0\gamma, \tag{2.80}$$

where γ is the *double-sided fractional bandwidth*. Since $Z_\mathrm{in} = R$ at resonance (because $W_\mathrm{m} = W_\mathrm{e}$), the maximum power absorption by the resonator can be found there. At all other frequencies, one can find less power absorption by the resonator, which can formally be described by [38]

$$|Z_\mathrm{in}|^2 = R^2/p. \tag{2.81}$$

Here, the power fraction p ranges between $0 < p < 1$ and denotes, at which power ($p = 1$ at maximum power) the bandwidth $2\Delta\omega$ is to be taken. E.g. $\gamma(p = 0.5)$ means that the bandwidth is measured at half-power, i.e. at the half of the maximum amplitude of a resonance curve with the ordinate in linear scales. As long as the frequency is close to resonance, (2.81) can be substituted in (2.80). This leads to a more general expression of Q_0 in relation to the power fraction p

$$Q_0 = \frac{1}{\gamma(p)}\sqrt{\frac{1-p}{p}}. \tag{2.82}$$

Again, $\gamma(p)$ denotes the bandwidth at the power fraction p. Usually, the bandwidth is measured at $p = 0.5$ which leads to the result

$$Q_0 = \frac{1}{\gamma(p = 0.5)} = \frac{1}{\tan\delta_{\mathrm{tot}}}. \tag{2.83}$$

The same result can be deduced for a parallel circuit.
In practice, there are lots of influences on the overall quality factor Q_L caused by the coupling to other circuitry and the environment. Thus, the overall quality factor Q_{L}, which is called the *loaded quality factor*, is lower than Q_0. The loaded and unloaded quality factors are connected via the *external quality factor* Q_{e}

$$\frac{1}{Q_{\mathrm{L}}} = \frac{1}{Q_0} + \frac{1}{Q_{\mathrm{e}}}, \tag{2.84}$$

which takes all environmental influences into account. The influence of an external load on an RLC circuit can be expressed by an additional load resistor R_{L} shunted to the resonator.

$$Q_{\mathrm{e}} = \begin{cases} \frac{\omega_0 L}{R_{\mathrm{L}}} & \text{for series circuits,} \\ \frac{R_{\mathrm{L}}}{\omega_0 L} & \text{for parallel circuits.} \end{cases} \tag{2.85}$$

Measuring Quality Factors

In order to obtain the quality factors of a resonator, one has to measure either the transmission $|S_{21}|$ through the resonator or the reflection $|S_{11}|$ from one port back to itself. This depends on the type of resonator, which will be explained in the following. This measurement method can be explained by introducing the *scattering theory*. In this model, the resonator is assumed to be a scatterer for the currents coming from both ports connected to the resonator. The incoming and outgoing currents at each port can be expressed as wavefunctions connected by the scattering matrix

$$\begin{pmatrix} \psi_{1,\mathrm{out}} \\ \psi_{2,\mathrm{out}} \end{pmatrix} = \begin{bmatrix} S_{11} & S_{12} \\ S_{21} & S_{22} \end{bmatrix} \cdot \begin{pmatrix} \psi_{1,\mathrm{in}} \\ \psi_{2,\mathrm{in}} \end{pmatrix}. \tag{2.86}$$

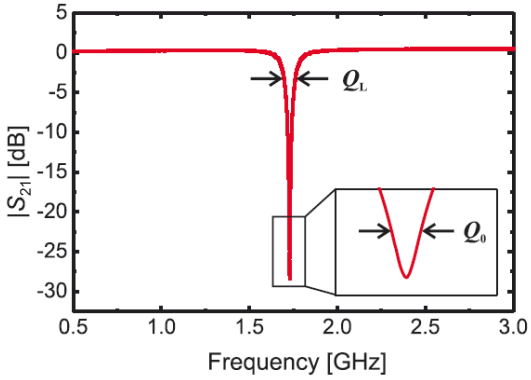

Figure 2.5:
A typical measured resonance dip in transmission $|S_{21}|$, with illustration of Q_{L} and Q_0.

A typical measurement curve of the transmission through a resonator is shown in figure 2.5.

Here, an *absorption dip* can be seen (in this case for a series-connected parallel resonator [38]). Q_0 is measured as depicted above at $\gamma(p = 0.5)$ above the minimum of $|S_{21}|$ while Q_{L} is measured at $\gamma(0.5)$ below the maximum. A factor of $\gamma(p = 0.5)$ means at half power (see above). In units of dB, as given here, one can obtain the value of $P = 3dB$ for half power using

$$P[\mathrm{dB}] = 10 \log_{10} \left(\mathrm{p} = \frac{\mathrm{P[W]}}{\mathrm{P_0[W]}} \right). \tag{2.87}$$

$P[\mathrm{dB}]$ denotes the power level for a reference power P_0 in W.

Intrinsic contributions to Q_0

There are various contributions to the intrinsic loss Q_0 from the resonator itself. These contributions compose the total value of Q_0 like

$$\frac{1}{Q_0} = \frac{1}{Q_\varepsilon} + \frac{1}{Q_{\mathrm{rad}}} + \frac{1}{Q_\rho}. \tag{2.88}$$

Here, Q_ε denotes the dielectric, Q_{rad} the radiation and Q_ρ the conductor losses.

2.3.3 Special Types of Resonators

Various types of resonators can be described by the idealized RLC circuit. It is important to distinguish between series or parallel resonators connected in series or in parallel to the environmental circuitry [38]. Beside this consideration, the physical implementation of the used components R, L and C is important. In this section, lumped element resonators consisting of discrete elements and coplanar waveguide resonators consisting of distributed elements will be described.

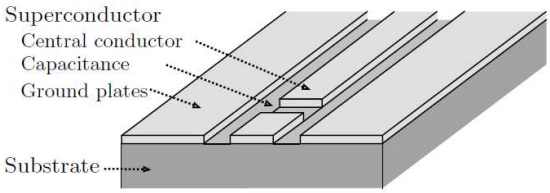

Figure 2.6:
Schematic representation of a CPWR taken from [14]. w is the width of the central conductor and s the width of the gap between the central conductor and the ground plates.

Lumped Element Resonators

As long as electrical components can be considered small in electrical size, meaning that their physical dimensions are much smaller than the electrical wavelength, which is the length of a transmission medium element expressed as the number of wavelengths of the signal propagating in the medium, they can be treated with the formulas of the previous section. In a lumped element voltage and current do not vary in magnitude and phase over its length. A typical lumped element in microelectronics is a plate capacitor with a size in the μm range. The capacitance C of such a small capacitor can be obtained by the well-known formula

$$C = \varepsilon_0 \varepsilon_\mathrm{r} \frac{A}{d}. \tag{2.89}$$

Here, A denotes the area of the planes and d the distance between the parallel plates.

Coplanar Waveguide Resonators (CPWRs)

In contrast to the lumped element resonator consisting of concentrated elements, the coplanar waveguide resonator consists of a symmetrical coplanar waveguide transmission line. This transmission line has an inner conductor line of width w separated from the surrounding ground plane by two gaps of width s (see figure 2.6). Although this type of resonator consists of distributed elements, it can be modeled by a lumped-element circuit. For this, the resistance load per unit length R', the inductance per unit length L' and the capacitance per unit length C' are introduced as normalized parameters [39]:

$$L' = \frac{Z_L \sqrt{\varepsilon_{\mathrm{r,eff}}}}{c_0}, \tag{2.90}$$

$$C' = \frac{\varepsilon_{\mathrm{r,eff}}}{L' c_0^2}, \tag{2.91}$$

$$R' = \frac{\alpha}{2 Z_L}. \tag{2.92}$$

Here, Z_L denotes the characteristic impedance, $\varepsilon_{\mathrm{r,eff}}$ the effective permittivity, α the attenuation constant and c_0 the vacuum speed of light.
The length of the transmission line determines the resonance frequency of the resonator. Typical CPWRs have the length l of a quarter- or half-wavelength of the corresponding

resonance frequency f_0

$$l_{\text{half}} = \frac{\lambda}{2} = \frac{1}{2}\frac{c_0}{f_0(\varepsilon_{\text{r,eff}})^{1/2}}, \tag{2.93}$$

$$l_{\text{quarter}} = \frac{\lambda}{4} = \frac{1}{4}\frac{c_0}{f_0(\varepsilon_{\text{r,eff}})^{1/2}}. \tag{2.94}$$

The effective dielectric constant of a CPW depends on the ratios $w/(w+2s)$ and s/h, with h denoting the substrate thickness. For thick substrates, $h \to \infty$ can be assumed leading to a saturated value of the effective dielectric constant $\varepsilon_{\text{r,eff}} = (\epsilon_{\text{r}} + 1)/2$.
The components R, L, and C of a CPWR can be deduced by treating the CPWR as lumped-element parallel circuit:

$$L = \frac{8l}{\pi^2}L', \tag{2.95}$$

$$C = \frac{l}{2}C', \tag{2.96}$$

$$R = \frac{Z_L}{\alpha l}. \tag{2.97}$$

With these values, the resonance frequency and the unloaded quality factor of the CPWR can be calculated as

$$f_0 = \frac{1}{2\pi\sqrt{LC}}, \tag{2.98}$$

$$Q_0 = 2\pi f_0 RC. \tag{2.99}$$

Kinetic Inductance

Normally, a microwave resonator is fabricated out of metal. Applying an electric field to the resonator forces the charge carriers, here the electrons, to move, which leads to a current flow.
In 1900, Drude proposed a model to explain the transport properties of electrons in metals [40]. In terms of this model, an electron passing through a metal is scattered at the ions, other electrons, phonons, etc. of this metal. This leads to a relation between the current density $\vec{J}$ of the electrons and the applied field $\vec{E}$

$$\vec{J} = \left(\frac{nq^2\tau}{m}\right)\vec{E}. \tag{2.100}$$

This equation was presented in (2.57) as *Ohm's law* with the conductivity $\sigma = \left(\frac{nq^2\tau}{m}\right)$. Here, n is the density, q the charge, m the mass and τ the mean free time of the electrons. Thus, a change of the field will cause a change of the current density. For a time-dependent electric field with frequency ω, the Drude model predicts a complex conductivity [40]

$$\sigma(\omega) = \frac{\sigma_0}{1+i\omega\tau} = \frac{ne^2\tau}{m(1+\omega^2\tau^2)} - i\frac{ne^2\omega\tau^2}{m(1+\omega^2\tau^2)} = \sigma' - i\sigma''. \tag{2.101}$$

The same form was deduced for the complex susceptibility in (2.23). The reason for this behavior is the finite relaxation time τ. It describes a delay in the response of the electron to the external force. For $\tau \to \infty$, which is the case at high frequencies and in high carrier mobility conductors (especially superconductors), the imaginary part becomes noticeable, which is related to the so-called kinetic inductance. This kinetic inductance L_{kin} can be treated as an additional series inductance to the normal geometrical inductance L_{g} which leads to

$$L = L_{\mathrm{g}} + L_{\mathrm{kin}}. \tag{2.102}$$

This additional inductance component has to be considered in superconducting resonators as it causes a shift of resonance frequency f_0 like

$$f_0 = \frac{1}{2\pi\sqrt{(L_{\mathrm{g}} + L_{\mathrm{kin}})C}}. \tag{2.103}$$

From further theoretical considerations, Mattis and Bardeen showed using the two fluid model that the quality factor of a superconducting resonator is given by [41]

$$Q_{\mathrm{MB}} = \frac{2}{\alpha}\frac{\sigma''}{\sigma'}, \tag{2.104}$$

with

$$\alpha = \frac{L_{\mathrm{kin}}}{L_{\mathrm{g}}}. \tag{2.105}$$

Chapter 3

Investigation of Dielectric Losses using Superconducting Microwave Resonators - State of the Art

In 2005 Martinis *et. al* showed that the same TLSs causing dielectric loss are also responsible for the main decoherence mechanism in superconducting phase qubits [8]. A superconducting phase qubit is realized as a superconducting ring interrupted by a Josephson junction. If the parameters are chosen in the right way, such a structure behaves like an artificial quantum mechanical two level system. Applying an adequate ac microwave signal to the qubit induces transitions between its ground and its excited state. For increasing length of this microwave pulse, the qubit will coherently oscillate between its two states, as can be seen in figure 3.1. This is commonly known as Rabi oscillations. The exponential decay of these oscillations is due to decoherence in the system. One of the main decoherence mechanisms are TLSs in qubit's vicinity, which couple to the qubit and extract energy from it. In figure 3.1, it can be seen that the decoherence is stronger if dielectrics with high dielectric losses are used in qubit fabrication. This shows that the TLSs responsible for the qubit decoherence and dielectric losses are indeed identical.

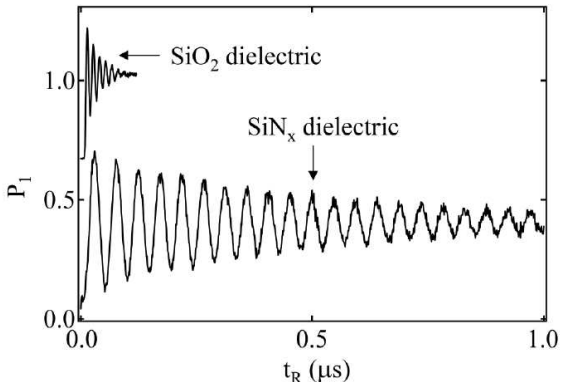

Figure 3.1:
Rabi Oscillations for a phase qubit using CVD SiO_2 (top trace, offset) and SiN_x (bottom trace) as a dielectric used in qubit fabrication. This comparison shows, that the dielectric losses in SiN_x are much lower than these of SiO_2. Microwaves at the qubit frequency are pulsed for a time t_R, and subsequent measurement of the qubit state shows an oscillation of the probability of the excited state. The figure is taken from [8].

Superconducting resonators used for loss measurements can be used to investigate temperature, power and frequency dependences of loss and hence learn more about the nature of TLSs responsible for losses. Furthermore, it is of great advantage that superconducting resonators use the same materials and working points as superconducting qubits. Understanding the loss mechanism in detail and finding low-loss materials to improve the performances of microwave devices are very important topics. This chapter will show the progress in this field starting with the investigation via coplanar waveguide resonators (CPWRs), followed by lumped element resonators. This progress will be described chronologically, but makes no claim to be complete as there are many scientific groups dealing with it. Afterwards, the measurement method developed at the IMS will be introduced and important enhancements of its design will be explained.

3.1 Coplanar Waveguide Resonators

In the next section investigations of dielectric losses in coplanar waveguide resonators will be discussed. The interpretation of their results will lead to the understanding of the nature of dielectric loss in superconducting microwave resonators.

3.1.1 Loss due to TLSs among Dielectric Substrates

In 2006 Barends *et. al* investigated the quality factors and phase noise of coplanar waveguide resonators made from Nb and Ta on dielectric substrates at GHz frequencies [10]. In figure 3.2 it can be seen that the quality factors saturate below $T/T_c < 0.25$ and that the saturation level increases with readout power. This effect could not be explained with Mattis-Bardeen theory (according to (2.104)) related to superconductivity mechanisms. The power dependence of the quality factor was attributed to a decrease of microwave losses for increasing power levels.

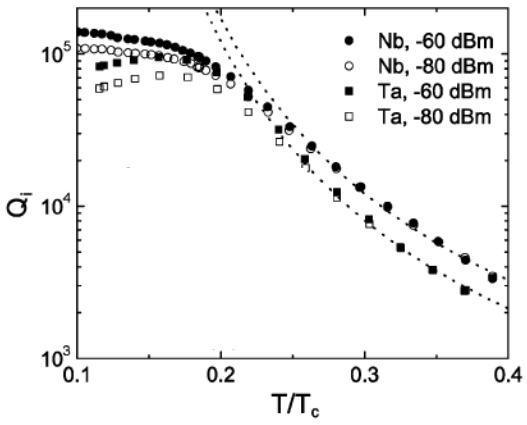

Figure 3.2:
Unloaded quality factor of Nb and Ta resonators as a function of the reduced temperature as measured by. For very low T/T_c the quality factors deviate from normal Mattis-Bardeen behavior (dotted lines) acoording to (2.104) and saturate due to TLSs in the surfaces. Both materials show the same behavior. The figure is taken from [10].

Furthermore, the resonance frequency showed a non-monotonic temperature dependence. In figure 3.3 it can be seen that above a tenth of T_c the resonance frequency increases with decreasing temperature, whereas below a tenth of T_c the resonance frequency decreases with decreasing temperature (see inset of figure 3.3). The temperature dependence of the resonance frequency above a tenth of T_c could be explained by superconductivity related mechanisms, while below the temperature dependence was assumed due to TLSs among the substrate.

Additionally, an observed $1/f$ like slope of the phase noise of the resonators were suggested to arise from two-level systems among the dielectric substrate (an theoretical deduction of the $1/f$ like TLS related noise can be found in [42]). This assumption was confirmed by the interesting fact that although the materials used for fabrication were different, their quality factors, shifts of resonance frequency and noise showed the same behavior at low temperatures.

These first investigations of quality factors, resonance frequency shifts and noise properties of CPWRs showed that these are good tools capable of observing TLSs based effects in microwave devices at low temperatures.

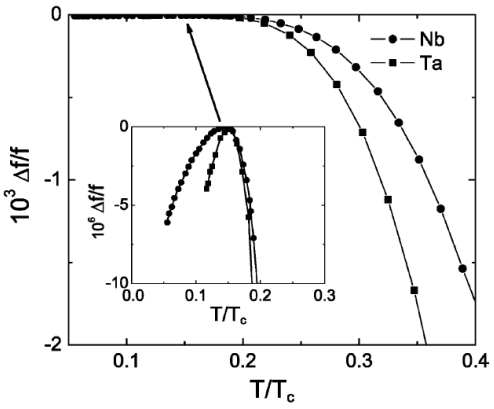

Figure 3.3:
Resonance frequency versus temperature. Above a temperature of a tenth of T_c the kinetic inductance decreases with decreasing temperature and the resonance frequency increases subsequently. The inset reveals that the slope changes sign for temperatures below a tenth of T_c. This is assumed due to TLSs among the substrate. The figure is taken from [10].

3.1.2 Identification of Surface Distributed TLSs

The discoveries of Barends *et. al* could be confirmed in 2007 by Kumar *et. al* [11]. Detailed investigations of the temperature and power dependence of the resonance frequency and frequency noise in quarter wavelength CPWRs made from Nb at GHz frequencies were carried out. In figure 3.4 it can be seen that below a temperature of 1.2 K a shift of resonance frequency could be detected, which increased with temperature while the Mattis-Bardeen theory (see dashed line in figure 3.4) would predict a much smaller shift opposite in sign.

This temperature dependence of the frequency shift was reported constant over a range of readout power (which is the applied power) of -96 to -72 dBm and for $T < 900$ mK could

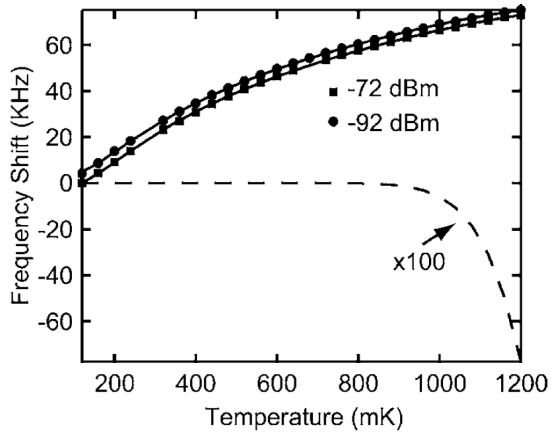

Figure 3.4:
In the results of the resonance frequency shift, defined as $\Delta f_0 = f_0(T,P) - f_0(120\text{ mK}, -72\text{ dBm})$, is plotted as a function of temperature for readout powers of -72 dBm (filled circle) and -92 dBm (filled square). The solid lines represent fits to (3.1) due to TLS theory, a further indication for TLSs in the surfaces. The figure is taken from [11].

be shown to be proportional to [11]

$$\frac{\Delta f_0}{f_0} \propto C \left[\mathrm{Re}\,\psi\left(\frac{1}{2} + \frac{hf_0}{2\pi i k_\mathrm{B} T}\right) - \log\left(\frac{hf_0}{k_\mathrm{B} T}\right)\right], \tag{3.1}$$

which is the mathematical expression of a change of permittivity due to resonant interaction of TLSs in amorphous dielectrics (see (2.45)) according to the tunneling model. In (3.1) C is a prefactor, f_0 denotes the resonance frequency of the resonator and ψ is the complex digamma function introduced with (2.45). This direct link between the change of permittivity due to TLSs and the change of the resonance frequency of a microwave resonator was a striking evidence of the TLS nature of dielectric losses among superconducting microwave resonators. In order to find a quantitative relation for the proportionality in (3.1) the prefactor was chosen to be $C = \frac{F\alpha}{\pi}$, where α is the same as (2.32) introduced in section 2.1.2 consisting of the density of states n of the TLSs and their dipole moments p. F was called the *forming factor* taking into account the distribution of the electric field in the resonator. It should quantify the portion of field in the TLSs volume to figure out where the TLSs are situated in the resonator. An obtained value of $F \approx 10^{-2}$ consistent with a reasonable thickness of order of 10 nm led to the conclusion of TLSs situated in thin layers on the surface of the resonator, e.g. due to oxidation of it. In addition, the temperature dependence of noise of the resonator could be modeled by TLS theory (for more information the see [11]) emphasizing the assumption of surface distributed TLSs.

In a closely-related work, Gao *et. al* investigated the influence of varying center strip width w of a CPWR on its excess frequency noise [43]. A rapid decrease of frequency noise with increasing w was found, scaling as $1/w^{1.6}$ and a semi-empirical model for TLS noise in superconducting microresonators was deduced being able to describe this noise effect quantitatively. In this model, a uniform spatial distribution of TLSs within a volume V_h of TLS-hosting material was assumed. V_h occupies some quantitative portion of the total resonator volume V. Considering a TLS to have an energy splitting $E = \sqrt{\Delta^2 + \Delta_0^2}$ (2.4) and a joint distribution function $f(\Delta, \Delta_0) = P/\Delta_0$ (see 2.1.1) between the TLS asymmetry

energy Δ and the tunnel splitting Δ_0 given by the tunneling model, the TLS contribution to the dielectric tensor could be deduced as [43]

$$\langle \varepsilon(\omega) \rangle = -\frac{\alpha}{\pi} \left[\mathrm{Re}\, \psi \left(\frac{1}{2} - \frac{\hbar\omega}{2\pi i k_\mathrm{B} T} \right) - \log \left(\frac{E_\mathrm{max}}{2\pi k_\mathrm{B} T} \right) \right]. \tag{3.2}$$

This is nearly the same as (2.45) except E_max which denotes the maximum energy level separation. Comparing (3.2) with (3.1) leads to the conclusion that for microwave resonators $E_\mathrm{max} = hf_0$, because at resonance the maximum power is applied. This was predicted by Schickfus *et. al* (see [16]) 30 years ago.
Using the real part $\Delta\varepsilon_1$ of this equation the temperature dependent fractional frequency shift of the resonator could be deduced to be [43]

$$\frac{\langle \Delta f_0 \rangle}{f_0} = -\frac{\int_{V_\mathrm{h}} \langle \Delta\varepsilon_1 \rangle |\vec{E}|^2 d\vec{r}}{\int_V \varepsilon |\vec{E}|^2 d\vec{r}} = \frac{w_\mathrm{h}^\mathrm{e}}{w^\mathrm{e}}. \tag{3.3}$$

This equation denotes the ratio of the electric energy w_h^e stored in the TLS-loaded volume V_h to the total electric energy w^e stored in the entire resonator expressing the first assumption of this model (see above). Thereby it was shown that the geometry of a CPWR has influence on the frequency noise. Evaluating (3.3) with an contour integral over the surface of the resonator assuming independent TLSs distributed in it the mentioned scaling of the noise could be deduced out of (3.3). This led to the conclusion that in CPWRs dielectric losses arise from surface TLSs and that the influence of the TLSs can be tuned by the geometry.

The next step was to determine the exact location of the TLSs in a CPWR. Therefore, Gao *et. al* used the same CPWRs with varying center strip widths and investigated this time the temperature dependence of the resonance frequency [12]. All resonators showed the same temperature dependence of the shift of the resonance frequency but with decreasing center strip width, the magnitude of the frequency shift increased (see figure 3.5).

The forming factor F introduced in [11] was directly connected with $w_\mathrm{h}^\mathrm{e}/w^\mathrm{e}$ introduced

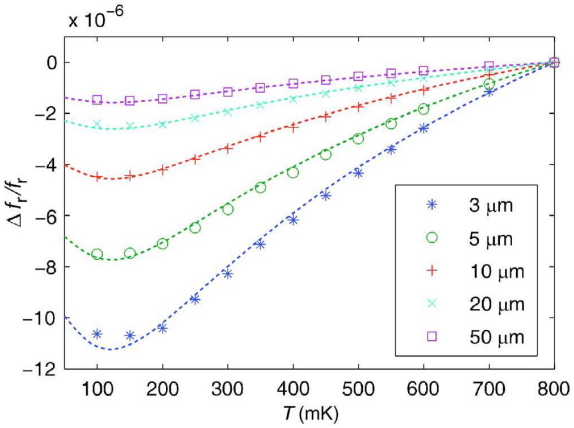

Figure 3.5:
The colored lines show the fractional frequency shifts $\frac{\Delta f_0}{f_0}$ as a function of temperature. $\frac{\Delta f_0}{f_0}$ is calculated by using $\frac{\Delta f_0}{f_0} = ((f_0(T) - f_0(800\ \mathrm{mK}))/\mathrm{f_0}(800\ \mathrm{mK})$. The markers represent different resonator geometries, as indicated by the values of the center strip width w in the legend. The dashed lines indicate fits to the TLS theory (3.1). The figure is taken from [12].

in [43]. Thus, the frequency shift could be expressed in terms of this factor as [12]

$$\frac{\Delta f_0}{f_0} = -\frac{F}{2}\frac{\Delta\varepsilon}{\varepsilon}. \tag{3.4}$$

It was suggested by Gao *et. al* that if TLSs were in the bulk substrate with dielectric constant ε_r the forming factor could be modeled by $F \approx \varepsilon_\mathrm{r}/(\varepsilon_\mathrm{r}+1)$ independent of the center strip width. If instead the TLSs were in a surface layer, F would be dependent on w [12]. The measurement results showed a dependence of F on w (as it can be seen in figure 3.5) confirming surface TLSs in a layer thickness of the order of a few nanometers. Estimation whether the TLSs are situated on the metal surface or the substrate (=gap) surface by introducing geometrical factors showed similar values for metal and substrate surfaces. Thus, the exact location stayed unclear.

In the same year, the temperature dependence of the resonance frequency and frequency noise was investigated [44] for CPWRs made from NbTiN [44] fabricated on different dielectrics like oxidized silicon, sapphire and hydrogenated silicon. Additionally the resonators were covered with sputtered SiO_x layers.
Interesting conclusions arose from this investigation. On the hand it could be observed that temperature dependence of the resonance frequency scales linearly with thickness of the SiO_x layer. In figure 3.6, it can be seen that the thicker the SiO_x layer on the NbTiN resonator the more pronounced the shift of the resonance frequency increasing with increasing temperature below 1.5 K (due to TLSs based mechanism) while decreasing with increasing temperature above 1.5 K (due to superconductivity based mechanims) [44].This was the same observation like in figure 3.3.
On the other hand the observed increase in noise is independent of the thickness of the SiO_x layer. These observations were interpreted as that the resonance frequency temperature dependence is due to TLSs in the dielectric volume sputtered on top, whereas the observed increase in the noise is due to the interface between superconductor and SiO_x layer.
Moreover, the noise level of Ta and uncovered NbTiN was very similar, whereas the resonance frequency dependence showed to be clear non-monotonic (caused by TLSs) for Ta, while for uncovered NbTiN, it followed Mattis-Bardeen theory (caused by kinetic inductance see 2.3.3). This observation suggested that the contribution of surface TLSs is dependent on the superconducting material itself. It led to the conclusion that there were less TLSs on the NbTiN surface than on the Ta one.
Additionally, the noise increased when using sapphire instead of silicon as substrate, indicating that the choice of crystalline substrate affects the frequency noise. This again points towards an influence to noise by the superconductor-dielectric interface.

This conclusion was even strengthened by the fact that for NbTiN on sapphire, the non-monotonic temperature dependence of the resonance frequency was analogous to that

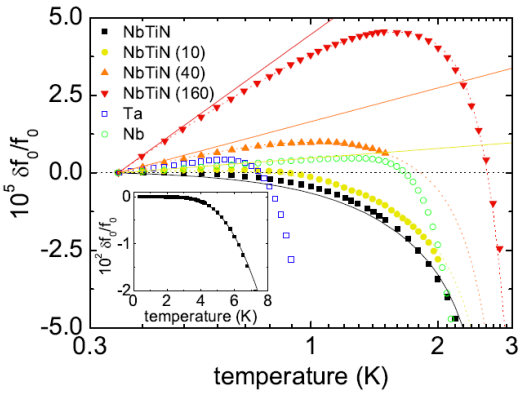

Figure 3.6:
(Color online) The temperature dependence of the resonance frequency of NbTiN samples with no coverage, NbTiN samples with a 10 nm, 40 nm or 160 nm thick SiO_x coverage, and samples of Ta and Nb. The solid yellow, orange and red lines are fits of the low temperature data to (2.47). The inset shows the temperature dependence of the resonance frequency of a NbTiN sample over a broader temperature range which closely follows Mattis-Bardeen theory (solid black line, see section 2.3.3). The superposition of the Mattis-Bardeen theory (solid black line) and fits to (2.47) found in data of covered samples (solid yellow, orange and red lines) yields the dotted yellow, orange and red lines. The figure is taken from [44].

of NbTiN on Si covered by SiO_x. This led to the conclusion that TLSs are situated in superconductor-dielectric interfaces as well as in superconductor-substrate interfaces. Hydrogenating the Si substrate showed a strong decrease of loss which led to the conclusion that the TLSs were present in the form of dangling bondings in the dielectric.

In a very recent investigation Lindström *et. al* confirmed the assumption of TLSs situated in the superconductor-substrate interface [13]. Investigating half- as well as quarter-wavelength CPWRs, the temperature and power dependence of the dielectric loss could be shown to arise directly from resonant absorption processes of TLSs. The absorption a is expressed by [13]

$$a = \frac{\pi\omega n p^2}{3c_0\varepsilon_0\varepsilon_r}\left(1+\frac{P}{P_c}\right)^{-1/2}\tanh\left(\frac{hf_0}{2k_BT}\right). \tag{3.5}$$

Here, d denotes the dipole moment, c_0 the speed of light in vacuum and n the density of TLS states. f_0 denotes the measurement frequency, which implies that only TLSs with an energy splitting of $E = hf_0$ take part in absorption (in agreement with [16]).
The influence of the resonant absorption of TLSs on the variation of frequency could be confirmed the same as in the work of Gao et al. or Kumar et al. following the expression [13]

$$\frac{\Delta f_0}{f_0} = \frac{f_0(T)-f_0(T_0)}{f_0(T_0)} = \frac{Fnd^2}{3\varepsilon}\left[\ln\left(\frac{T}{T_0}\right) - (g(T,\omega)-g(T_0,\omega))\right], \tag{3.6}$$

where $g(T,\omega) = \mathrm{Re}\,\psi\left(\frac{1}{2}-\frac{\hbar\omega-i\Gamma}{2\pi i k_B T}\right)$, T_0 is a reference temperature, F the forming factor introduced by Kumar and Gao and ψ the complex digamma function. The difference between (3.6) and (3.1) or (3.2) lies in the choice of the reference temperature T_0. As it was shown with (2.45) and (2.46), (3.1) or (3.2) follow out of (3.6) for $T_0 = 0$. It has to be criticize that $T_0 = 0$ cannot be reached experimentally. Thus, (3.6) is the exact expression for the TLSs caused frequency shift and (3.1) or (3.2) are just approximations.

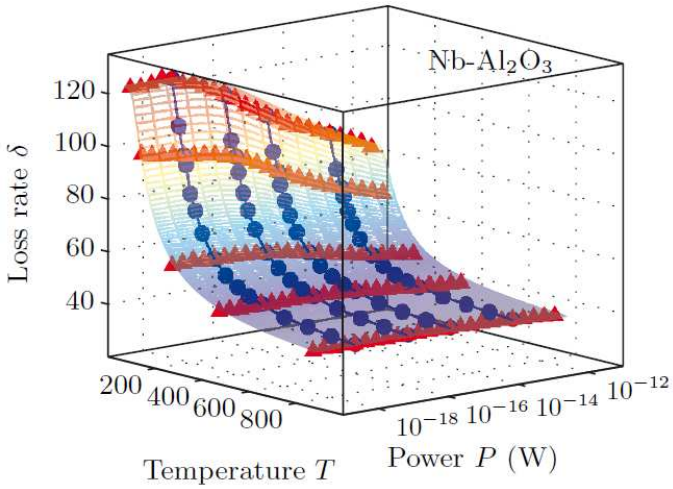

Figure 3.7:
The complete description of the loss illustrated for a Nb on sapphire sample. The grid is generated using (3.5) separated in temperature and power dependence part. Blue circles show measured data for the temperature dependence and the red triangles show measured data for the power dependence. The figure is taken from [14].

It could be observed as well that for temperatures $T \ll T_c$, thermal effects on the kinetic inductance (Mattis-Bardeen theory) were small. The main contribution comes from the resonator itself. Investigating resonators at frequencies in the range of 5 to 8 GHz, no mentionable frequency dependence of the frequency shift could be detected.

Additionally, it shall be mentioned that investigations of Macha *et. al* [14] led to the same conclusions as discussed in the work of Lindström investigating the temperature and power dependence of dielectric losses (see figure 3.7). Interestingly, the influence of the TLSs is of the same order of magnitude for all investigated superconductor (Nb, Al) substrate (Si, sapphire) combinations confirming the suggestion of a common nature of TLSs in CPWRs in general surface/interface states. Comparing this result with results obtained with CPWRs made from NbTiN (see [44] and above) and Re (see [45]) it can be assumed that it is possible to reduce influence of surface distributed TLSs by using superconductors with little surface oxide.
Another interesting observation by Macha *et. al* was that the exponent of the power-depending term of the loss were found to be much smaller than it was predicted by [16]. This fact was interpreted as that the power dependence of the losses is not only due to resonant TLS interaction. From the author's site, only a factor of 2 in [14]

$$\delta_{\mathrm{TLS}} = 2 \cdot F\alpha \cdot 2\pi\nu_0 \left(1 + \frac{P}{P_c}\right)^{\varphi} \tanh\left(\frac{h\nu_0}{2k_B T}\right), \tag{3.7}$$

remains unclear because it differs from (2.49) discussed in section 2.1.3. In (3.7), $\nu_0 = \frac{\omega}{2\pi}$ denotes the resonance frequency of the CPWR.

In a not yet published work [15], Pappas *et. al* deduced the temperature and power dependences of TLSs based losses in CPWRs as well as the temperature dependence of the resonance frequency shift of CPWRs due to TLSs concerning resonant interaction of these TLSs with the applied electric field at $T \ll T_{\mathrm{C}}$. This deduction goes hand in hand with the description of the properties of amorphous dielectrics in section 2.1.3.

The nature of the TLS dipole assumed in this model is a polar molecule such as OH^- or other impurities with precessing electric dipole moments in the electric field. The resonant interaction between such a polar molecule and an applied electric field can be described in this model by the resonant susceptibility

$$\chi_{res} = \left[\tanh\left(\frac{E}{k_B T}\right)\right] \cdot \left[\frac{1}{(\omega_0 - \omega) + i\tau_2^{-1}}\right] \cdot \left[\frac{1 + (\omega_0 - \omega)\tau_2^2}{1 + \Omega^2\tau_1\tau_2 + (\omega_0 - \omega)^2\tau_2^2}\right]. \tag{3.8}$$

Here, ω_0 is the excitation frequency, τ_2 the decoherence lifetime, τ_1 the energy relaxation lifetime, and Ω the Rabi frequency.
In a *weak field* the third factor of (3.8), which describes the dynamics of the system, can be neglected. Integration over available TLS energy splittings E up to the excitation energy $\hbar\omega_0$ leads to the well known description for the absorption (for the dielectric loss) (3.5) with the power dependent term equal to unity.
With the help of the Kramers-Kronig relation (2.44), (3.6) can be deduced out of (3.5).
In strong fields, the dynamics in the last factor of (3.8) have to be considered and lead to the power dependent term in (3.5), whereas (3.6) stays the same. Since measurements at high powers can be performed faster than at low power (because thermal noise effects are reduced), measuring the resonance frequency shift of a CPWR at low temperature in the high power limit is assumed to be preferable for evaluating the TLS density of states n and their dipole moment p. [15]
From author's site this has to be limited, because the comparability of the values of $F\alpha$ from loss measurements and frequency measurements is only given in the case of an independent density of TLSs states. In the case of an energy dependent density the values of $F\alpha$ need not to be identical as it was deduced in [30].

Additional influences of magnetic fields on the performance of CPWRs [45, 46] will not be discussed here as the investigation of the influence of magnetic fields is not part of this thesis.

3.2 Lumped Element Resonators

Not only CPWRs but also lumped element resonators are capable to investigate the dielectric losses. In the next sections investigations of dielectric losses with lumped element resonators will be presented leading to the measurement method used within this thesis.
The investigation of dielectric loss using lumped element resonators has not been pushed as intensively as using CPWRs. One reason for that is the disadvantage of low quality factors in lumped element resonators in comparison to coplanar structures. However, the advantages of compact size and easily-computable electrical variables still make lumped element resonators interesting, e.g for Kinetic Inductance Detectors (KIDs) [47].

For Lumped Element Kinetic Inductance Detectors (LEKIDs) the advantage of compact size is used to fabricate whole arrays of these LEKIDS on a small suitable chip size. For these LEKIDs, interdigitated capacitors (IDCs) are employed. Since these capacitors are coplanar elements without any dielectric between the two electrodes, these capacitors show similar influences from surface distributed TLSs [48].
Another realization of lumped element capacitors are standard parallel plate capacitors which consist of two superconducting electrodes separated by a dielectric layer. In 2008 O'Connell *et. al* used such capacitors to set up an equivalent circuit for CPWRs to be able to determine the contributions of TLS induced loss to CPWRs [9]. The facts that the capacitance of a parallel plate capacitor can be computed easily by (5.1) that the entire electric field is stored in the dielectric between the capacitor plates were used to investigate the influence of TLSs in the bulk dielectric. In contrast, in a CPWR the electric field samples a large volume around the CPWR not filled by the dielectric of interest and therefore, the fraction of dielectric energy has to be calculated using finite-element methods. Thus, using lumped element resonators with parallel plate capacitors, the values of the intrinsic dielectric losses can be achieved much more directly and reliably.
In order to avoid losses coming from TLSs in the bulk dielectrics, Cicak *et. al* presented a special design of plate capacitors without dielectric between the plates [48]. Implementing this type of vacuum-gap capacitors (VGCs) into resonators and qubits showed that VGC based devices have very low losses (see figure 3.8), although a slight power dependent behavior of the losses similar to those arising from TLSs was observed. This leads to the conclusion that even in VGCs, surface distributed TLSs exist.

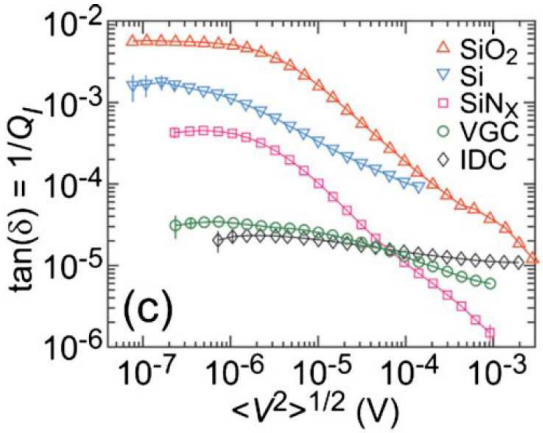

Figure 3.8:
Measured $\tan\delta$ vs average applied voltage $\langle V^2\rangle^{1/2}$ for three capacitors with dielectric materials SiO_2, Si, or SiN_x between the plates, a VGC with Al posts, and an IDC capacitor. The VGC based resonator shows very low losses due to the missing dielectric between the plates. However, a slight saturation of the losses is visible. The figure is taken from [48].

3.3 Measurement Method Developed at the IMS

In this section the principle idea of the measurement method this thesis is dealing with shall be described. As shown in the beginning of this chapter all described effects of TLSs in CPWRs are related to TLSs situated in surface/interface layers. As it was explained in

the previous section, lumped element resonators with parallel plate capacitors filled by the dielectric of interest offer the possibility of investigating the dielectric losses evolving from the TLSs situated in the bulk dielectric. In the investigations of O'Connell *et. al* such lumped element resonators were decoupled capacitively from the loadlines to establish an equivalent circuit of a half-wavelength CPWR. Firstly, this means that only the loaded quality factor is directly readable from the measurement curve but not the unloaded one. Thus, this method is not direct. Secondly, the fact that the resonator is situated between the loadline and ground (see figure 3.9a) leads to additional parallel load resistors which have to be considered extracting the dielectric losses from measurements. And thirdly, the values of C_c and the pieces of loadlines marked with red cicles around (see figure 3.9a)) are unknown what makes the results not quantitatively reliable.

Thus, there was a need of a *reliable* and *direct* determination of dielectric losses. To avoid

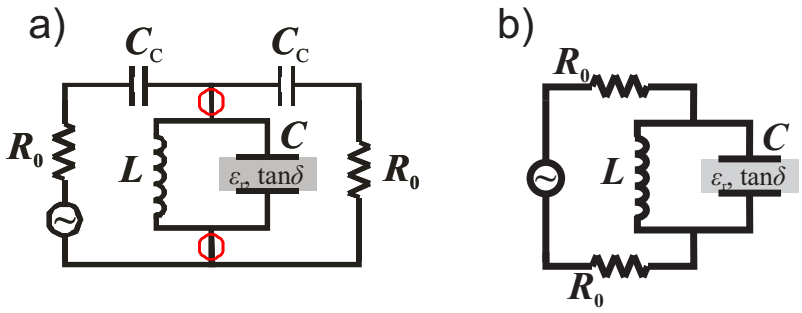

Figure 3.9:
a) Schematics of a lumped element resonator with coupling capacitors C_c as an equivalent circuit for a half-wavelength CPWR. The red circles emphasize additional load lines essential for this technique. These load lines have influences on the measurement (as explained in the text). **b)** Schematic of a lumped element resonator used at the IMS, omitting disturbing coupling capacitors and load lines.

additional coupling capacitors and parallel load resistors, a pure LC circuit (see figure 3.9a)) was designed consisting of a parallel plate capacitor and an inductance realized by a microstrip line directly connected to the load lines (see figure 3.10) [49].

By varying the area of the capacitor plates and the geometry of the inductance, a wide

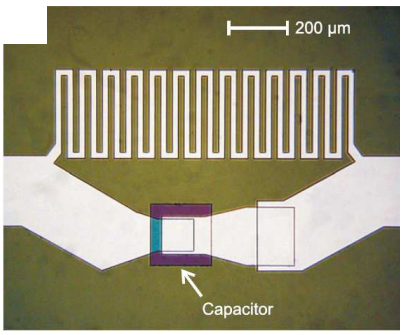

Figure 3.10:
Photograph of an LC circuit with SiO as dielectric between the capacitor plates. This is the narrowest meander that was used to realize the inductance.

frequency range was covered (150 MHz to 15 GHz). By achieving the same resonance frequency with different geometries, the redistribution of losses between the inductance

and the capacitance could be investigated. The comparison between different resonator geometries was also employed to optimize the inductor design and avoid capacitive coupling within the meanders.
When measuring the magnitude of transmission $|S_{21}|$ of such a superconducting resonator, one normally obtains the loaded quality factor Q_{L}, which is given by (2.84). Here, Q_{e} is a measure of how much the resonator is decoupled from its environment. Q_0 is the intrinsic quality factor and denotes the loss in the resonator itself. It is composed of three contributions as it was given by (2.88). Here, $1/Q_\varepsilon = \tan\delta$ denote the dielectric, $1/Q_{\mathrm{rad}}$ the radiation and $1/Q_\rho$ the conductor losses. For a carefully designed superconducting resonator with matched lines and a closed housing, $1/Q_{\mathrm{rad}}$ is negligible. As for the resonators the surface impedance amounts for $R_{\mathrm{s}} = 0.32\ \mu\ \Omega\ \mathrm{GHz}^{-2} \cdot f^2$ [49], $1/Q_\rho \approx 1 \cdot 10^{-7}$ at 100 MHz and $1/Q_\rho \approx 1 \cdot 10^{-7}$ at 15 GHz (all at 4.2 K) can be estimated. This is at least one order of magnitude lower than all measured $1/Q_0$ values (see [49]). Since R_{s} decreases exponentially with temperature [39], the described method would be especially suitable for the characterization of low-loss materials for qubit applications, since $1/Q_\rho < 1 \cdot 10^{-22}$ already at 300 mK. The fact that conductor or inductor losses do not enter the measured Q_0 values has also been confirmed by simulations and experiments, as will be discussed in chapters 4 and 5. Altogether it can safely be assumed that in the presented method $1/Q_0 = 1/Q_\varepsilon = \tan\delta$. That means that by measuring the transmission $|S_{21}|$, the total dielectric losses at the resonance frequency can be obtained from the measurement data.

3.4 Enhancements of IMS Measurement Method within this Thesis

The measurement method described in the previous section led to a lot of useful results (see [49] and the experimental results chapter). As this type of resonator has no coupling capacitors, it can be seen as a notch filter. The advantage of such a notch filter is that multiplexing is possible by putting resonators in series which cannot be done for the resonator design introduced by O'Connell *et. al* or e.g half-wavelength CPWRs, because these act like bandpasses. With a multiplexed resonator, losses at several frequencies in a broad frequency range can be investigated in one cooldown which is a striking advantage in the face of very time-consuming measurements like low temperature measurements in dilution fridges. An obtained measurement curve of a sample with four resonators in series is shown in Figure 3.11. It can be seen that all four resonances exist. Extracting the values of the loss tangent it could be shown that the values obtained by single resonators could be reproduced to a precision better than 0.1% by the multiplexed ones. This validated the idea of multiplexing the resonators. Having a multiplexed resonator to measure losses at several frequencies in a broad frequency range requires a special broadband measurement

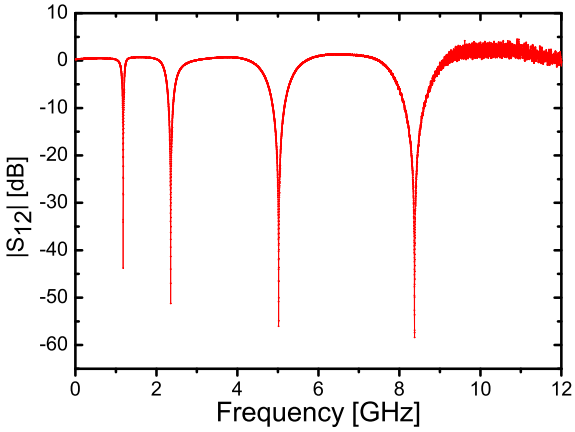

Figure 3.11:
Measurement curve for a sample with 4 resonators in series. The extracted values of the unloaded quality factors reproduced the ones obtained with single resonators to a precision better than 0.1 %. Thus, measurements at several frequencies in a wide frequency range in one cooldown are possible.

setup. Such a setup has been developed to complete the measurement method and will be explained in detail in chapter 5.

Additionally, the brass housing was found to influence the observed quality factors, which will be discussed in more detail in chapter 5. Using copper for the housings instead of brass seemed to eliminate this influence.

Chapter 4

Experimental Techniques

As briefly discussed in the previous chapter, a reliable and direct measurement method had to be developed to investigate the bulk losses due to TLSs in amorphous dielectrics usually used in Josephson Junction (JJ) fabrication. These JJs consist of a superconductor-oxide-superconductor trilayer and represent the basic component of qubits. In section4.1, the basic ideas influencing the design of the resonators will be shown, the simulation and afterwards the fabrication will be presented. As different dielectrics are used in JJ and qubit fabrication, collaborations with different groups were set up to be able to investigate various types of these dielectrics. A further condition in this context was to develop a resonator design which could be fabricated by other groups easily and offers comparable results. The different fabrication techniques used by the participating groups will be discussed at the end of section 4.1. In section 4.3.1, the different measurement setups will be described in order to investigate the temperature range of 100 mK to 4.2 K.

4.1 Sample Design and Simulation

4.1.1 Sample Design

The principle conditions in order to be able to investigate dielectric losses directly with the use of superconducting lumped element resonators and their implementations into the used resonators had been discussed in section 3.3. Furthermore, enhancements of the measurement method in order to measure at various frequencies in a broad frequency range in one cooldown were explained in section 3.4.
The areas of the parallel plates of the implemented capacitors were designed in the range from 10 x 10 μm^2 up to around 400 x 400 μm^2. Adequate inductors in order to achieve resonance frequencies in the range of 150 MHz up to 15 GHz were designed either as meandered or straight microstriplines. The distance between the meander arms was varied in order to reveal possible influences of capacitive parasitics between the meander lines. One example of these resonators have been shown in figure 3.10.

Altogether over 40 different resonators were designed covering a frequency range of 150 MHz to 15 GHz for various types dielectrics with different values of ε_r. By varying L and C relative to each other, the same resonance frequency was achieved for different geometries. Thus, it could be proved that the losses extracted from the measurements were equal at one frequency independent of the resonator design. As discussed in section 3.4, multiplexed resonators were succesfully designed implementing up to four resonators in series. The maximum number of resonators in series only depends on the chip size. Every sample was installed into a closed housing; at the beginning made from brass, later made from copper. The reason for changing the material the material of the housing will be explained in section 5.1.2. Another important part of this thesis was the design of photo masks for the photolithography fabrication process. The challenge was to adapt these mask designs to the different types of processes employed by the collaborating groups. Therefore, a detailed knowledge of all involved material parameters and types of processes was essential.

4.1.2 Simulation

During the design process, the simulation of the resonators were done in order to figure out if the designs were suitable for measurement. For this purpose, the commercial software Sonnet [50] was used. With this software it was possible to simulate any superconducting parameters (e.g. surface impedance, kinetic inductance, etc.) and geometrical parameters as well as material properties based on Maxwell equations. Additional, the simulation files could be directly used as mask files. A typical simulation file of a sample with four resonators in series simulated in Sonnet is shown in fig. 4.1.

The intrinsic quality factor Q_0 can be directly extracted from the resonance dip (see section 2.3.2). The extraction of the loss out of the dip measurement is done by simply calculating $Q_0 = 1/\gamma(0.5) = f_0/\delta f$ (this was discussed in 2.3.2). Here, δf is the bandwidth of the resonance dip at $|S_{12}| = \sqrt{2|S_{12,\min}|^2/(1+|S_{12,\min}|^2)}$ and $|S_{12,\min}|$ is taken at the resonance (see (2.83) and [51]). Thus, it is obvious that besides a possible measurement error, no further error sources enter the determination of Q_0. In simulations, all parameters (Nb as superconductor, the values of ε_r of the different dielectrics between the plates and of the substrate and the physical sizes) were inserted. The loss calculated as $\tan\delta = 1/Q_0$ out of Q_0 extracted from the simulated resonance curves was always equal to the loss value of the dielectric between the capacitor plates inserted in the simulation. This was plausible as the additional contributions (besides the dielectric loss Q_ε), Q_{rad} (radiation loss) and Q_ρ (conductor loss), to Q_0 introduced in (2.88) were assumed to be negligible as it was shown in section 3.3. In order to achieve a 50 Ω matching and thereby avoid radiation loss, the width of the line connecting the resonators (see figure 4.1) were simulated using the software WAVE, which was developed at the IMS. For a 200 nm thick microstrip line on a 300 μm thick silicon substrate (with $\varepsilon_r = 11.9$), the typical line width

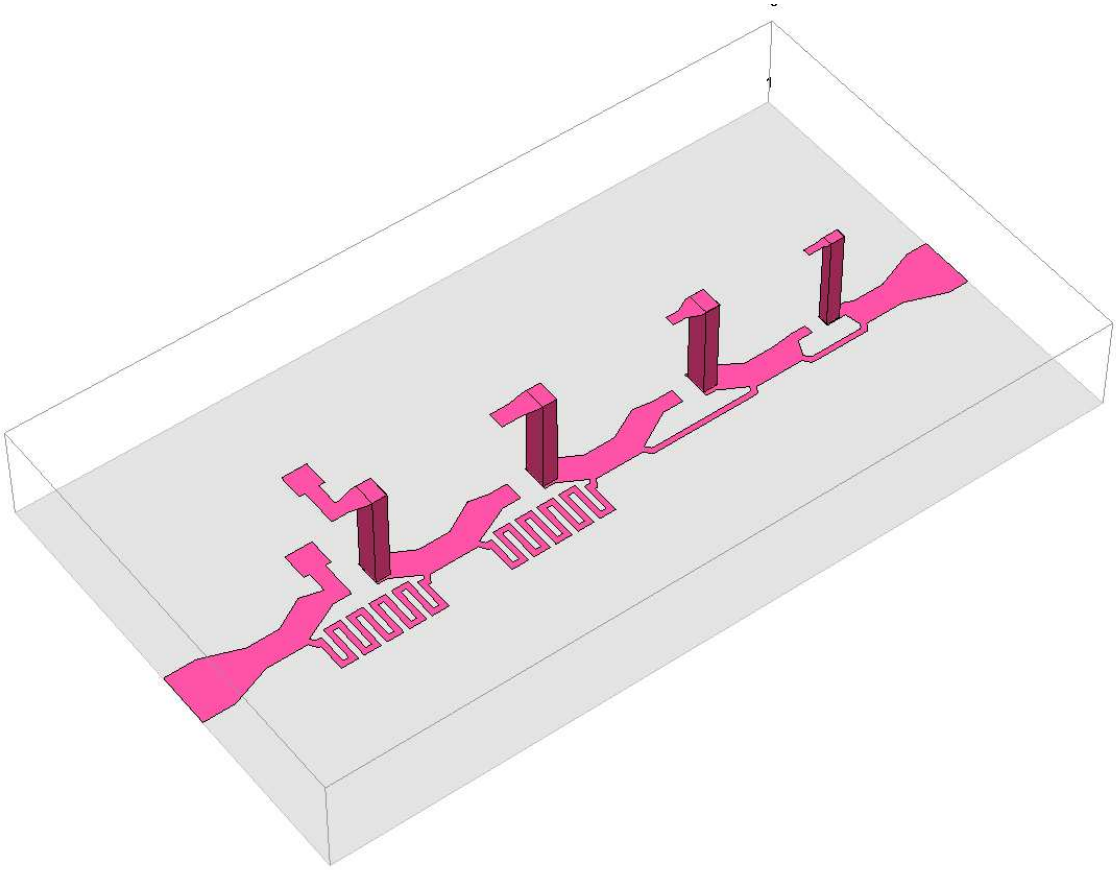

Figure 4.1:
A 3D view of a typical design and simulation file in the Sonnet environment. Here, a multiplexed resonator with 4 resonators at 4 different frequencies within a frequency range of 1 to 9 GHz is shown.The distance between base and top electrode of the capacitor is not true to scale in order to give a better overview of the multiplexed resonator. The broad microstrip lines at both ends are the contact plates for the SMA connectors which are tapered to the 50 Ω matched microstrip line which connects the resonators.

is 240 μm. As the type of substrate and its size determines the width of the microstrip line, it has to be calculated for all substrates used. As the SMA connectors were 500 μm wide, the microstrip line was tapered linearly from 500 μm to 240 μm (see figure 4.1) in order to keep close to a 50 Ω matching. As a linear taper showed no influence on the simulated loss value it was used to connect the contact plate with the microstrip. The fact that solely the dielectric loss of the amorphous dielectric between the plates determined the simulated measurement results independent of the dielectric parameters chosen for the substrate lead to the conclusion that entire dielectric field is stored in the capacitor. Thus, this measurement method could be called a direct measurement method of dielectric loss of thin films.

In the case of the multiplexed resonators, it was simulated how far the resonators have to be placed apart in order to get no crosstalk between them. Simulations showed that the resonators could be placed directly next to each other without causing crosstalk. However,

in the actual used design four resonators are connected in series (see figure 4.1) with short 50 Ω lines to ensure 50 Ω matching across the entire chip.

4.2 Fabrication

In this section, the different fabrication techniques used by the different groups whose samples were invastigated will be described shortly. Only the processing at the Institut für Mikro- und Nanoelektronische Syteme (IMS) will be explained in more detail as the fabrication of the resonators in Karlsruhe was part of this thesis.

4.2.1 Fabrication at IMS

After designing and simulating various resonators, it was part of this thesis to fabricate all the resonators containing Nb_2O_5, AlO_x and SiO as dielectrics. Altogether, more than 200 resonators were fabricated.
At the IMS, all layers were fabricated using only lift-off processes so that no etching techniques like reactive-ion-etching (RIE) or ion-beam-etching (IBE) had to be used. This ensured that the material properties were not altered by chemical processes or ion bombardment.
For each layer, the photo resist AZ5214E was spun onto a 10 x 10 mm chip (Si substrate, 300 μm thick) for 60 seconds at 6000 rpm. The resist was baked at 85 °C for 4 minutes. To remove photo resist from the edges of the chip, only the edges were exposed for 30 seconds while the rest of the chip was covered by a photomask. This was followed by developing for 30 seconds in an 2:1 solution of water to AZ developer. The "edge removing" process ensures that the photomask lies plane on the resist to avoid diffraction of used light at structures edges. Then a photomask is used to expose the resonator structure onto the resist. This mask is completely transparent except the structure of the resonator. With this mask the chip is exposed for 5 seconds before baking it at 120 °C for 5 minutes. Then the chip is exposed a last time for one minute without any coverage so that the original exposure is inverted. Finally, the chip is developed in a soft developer (MIF) for around 1 minute and 50 seconds. This process is called *inverted photolithography*. For all layers, the same photolithography process is used.
Both the base and the top electrode were made from Nb. Before Nb was sputtered, the chip was cleaned with an Ar ion beam for 10 minutes at an Ar pressure of $1.3 \cdot 10^{-3}$ mbar at constant beam voltage of 100 V and beam current of 10 mA. The base pressure in the sputter chamber is lower than $2 \cdot 10^{-7}$ mbar to avoid any contamination. Nb is sputtered at an Ar pressure of $5 \cdot 10^{-3}$ mbar at a constant rate of 18 nm/min, a sputter voltage of around 300 V and a sputter current of 175 mA. Usually, the base Nb layer is around 200 nm thick while the top layer is always 100 nm thicker than the dielectric to ensure

sufficient step coverage.
Nb_2O_5 was created out of the base electrode by anodic oxidation in an aqueous solution of $(NH_4)B_5O_8$ and $C_2H_6O_2$ at room temperature. The thickness of the grown Nb_2O_5 is controlled by the applied voltage. For a voltage of 40 V, a thickness of 96 nm can be achieved. As it will be shown in the chapter 5.1.4, different electrolytes like H_2SO_4 and H_3PO_4 have been tested to see whether the loss in Nb_2O_5 or Al would change.

SiO was thermally evaporated onto water-cooled samples at a rate of around 40 nm/min at a pressure lower than 10^{-6} mbar. It was desposited in thickness steps of around 100 nm to avoid that the photo resist gets too hot. After every single step, evaporation was interrupted for a few minutes.

After any deposition, the samples were placed in acetone to dissolve the photo resist and carry out the lift-off process. After finishing all layers, the samples were diced to a size of 9 x 9 mm.

4.2.2 Fabrication at PTB

The samples containing SiN_x were fabricated at the Physikalisch-Technische Bundesanstalt (PTB) in Braunschweig as part of the standard junction process [52]. The SiN_x was deposited by PECVD (physically enhanced chemical vapor deposition) at a temperature of 100 °C and a rate of 48 nm/min.

4.2.3 Fabrication at ICIB

One of the most promising candidates for dielectrics with low-loss is hydrogenated amorphous silicon (a-Si:H), which was fabricated at the Istituto di Cibernetica "E. Caianiello" (ICIB) of the Consiglio Nazionale delle Ricerche (CNR) in Naples. The deposition was done by CVD (chemical vapor deposition) at 250 °C, a pressure of 200 mTorr, a power of 5 W and a rate of 3 $\mathring{A}/s$.

4.3 Measurement Setup

Another important part of the presented method is the measurement setup. In this section, the measurement setups used at 4.2 K, 300 mK and 100 mK will be described. Three different techniques of cooling were used. At 4.2 K, a typical bath cooling with a dipstick in liquid ^{4}He was used. To achieve temperatures of around 300 mK, a ^{3}He cryostat was used, while to achieve even lower temperatures, the resonators were cooled in a dilution refridgerator. In principle it is possible to achieve lower temperatures than 100 mK with the used dilution refridgerator, but due to a faulty microwave cable, it was not possible to achieve temperatures lower than around 100 mK during the measurements described in this thesis. The main part of the following section is the special broadband loss measurement setup developed to investigate the frequency dependence of losses over a wide frequency range in only one cooldown cycle at very low temperatures and energies.

4.3.1 Measurements at Liquid ^{4}He

After mounting the samples into the housings, the resonances were measured in the S_{12} parameter at 4.2 K with a network analyzer (Agilent E8361A).In the case of transmission, a network analyzer measures the the parameter $|S_{21}|$ of the scattering matrix S introduced in (2.86). The housed samples were connected via SMA connectors to two unattenuated semi-rigid cables matched to 50 Ω. These cables were made from stainless steel and integrated into a dipstick. This dipstick was immersed into a ^{4}He dewar so that a temperature of 4.2 K, which is the boiling point of ^{4}He, could be achieved. The cooling rate was strong enough to thermalize in the cables in ^{4}He bath so that no attenuation was needed. The intrinsic quality factor Q_0 could be directly extracted from the resonance dip measured by the network analyzer. As it was discussed in section 4.3.2, the extraction of the loss out of the network analyzer measurement was done by simply calculating $Q_0 = 1/\gamma(0.5) = f_{res}/\delta f$. Here, δf is the bandwidth of the resonance dip at $|S_{12}| = \sqrt{2|S_{12,\min}|^2/(1+|S_{12,\min}|^2)}$ and $|S_{12,\min}|$ was taken at the resonance (see (2.83) and [51]). This method is called the *3 dB method*, because 3 dB is the power level (= half power level) at witch the bandwidth is extracted. To be able to achieve reliable results, the measured curves had to be very smooth. Especially at higher frequencies, noise came into play, disturbing the smoothness of the measurement curves. Two possibilities to find a remedy were to reduce the internal bandwidth (1 kHz in the measurements at 4.2 K) of the network analyzer and repeat the measurement several times and to average over the curves, because the noise has stochastic nature and can therefore be averaged out to a certain degree. At 4.2 K an average factor of 100 up to 600 was chosen. The measured curves were analyzed by Matlab [53] uing the 3-dB-method.

4.3.2 Special Broadband Loss Measurement Setup for Low Temperatures and Energies

This section discusses the development of a broadband measurement setup for very low temperatures ($T < 1K$) and powers (single photon regime).
At low cryogenic temperatures ($T < 1$ K) it is standard to install attenuators to the cables going down to the sample in order to attenuate the signal in the order of several magnitudes. Resistors are used as attenuators to reduce noise coming to the sample. The samples are not bath cooled but placed in an evacuated chamber and thermally anchored to a cold stage.
In a ^{3}He cryostat, a temperature of 300 mK can be achieved. ^{3}He is a rare and thus, expensive isotope of ^{4}He. It boils at 3.19 K and has a 70 times higher vapor pressure. This high vapor pressure makes it possible to achieve low temperatures down to 300 mK by pumping the ^{3}He. At the Physikalische Institut (PI) of the KIT, a Janis Modell He-3-SVSD-30 with a 2-inch wide vacuum chamber is used. It has a charcoal adsorption pump, with which very high cooling rates can be achieved. A detailed description of the principle of operation of a ^{3}He cryostat can be found in [6].
As mentioned before, for even lower temperatures than 300 mK a dilution refridgerator has to be used. In order to a reach temperatures of 100 mK or below, a dilution fridge uses a mixture of ^{3}He and ^{4}He. Below a critical temperature of 800 - 900 mK, the mixture undergoes a spontaneous phase separation, leading to a ^{3}He rich and a ^{3}He poor phase. Energy is required to transport atoms from the rich to the poor phase. If this transition is set up continuously, the mixture is cooled and can reach very low temperatures down to 10 mK. The principle and different types of such dilution refridgerators are explained in detail in [6]. For the dilution fridge measurements at the Physikaische Institut (PI) an Oxford Kelvinox KELMX SYSTEM GA 38832 was used.
By attenuating the signal, one is able to apply very low powers to the sample built into the cryostat. In fig. 4.2 one can see a -20 dB attenuator thermally anchored at 4 K. -20 dB is equal to a dissipation of 99 % of the applied power. Another -20 dB attenuator is thermally anchored at the coldest stage (either 300 mK for the ^{3}He cryostat or 100 mK for the dilution fridge). In combination with the cables, which have an attenuation of -15 dB, and a step attenuator, which is able to vary the attenuation in steps from 0 to -60 dB, a maximum attenuation of -115 dB could be achieved, without considering the adjustable output power of the network analyzer. The thermal anchoring of the attenuators reduces thermal noise. With the two anchored -20 dB attenuators, the thermal noise temperature could be reduced to 30 mK at the coldest stage (for both cryostats).
In the outgoing line, the signal has to be amplified again to be able to measure the signal back at room temperature. At this side, the sample has to be protected from noise coming from the amplifier thermally anchored at 4.2 K. For this purpose, the standard technique is to use a circulator at the coldest stage. A circulator is like a one-way resistor, attenu-

ating the signal coming from the amplifier but leaving that one coming from the sample undamped. As this technique is limited by the small frequency ranges of these circulators (usually 2 - 4 GHz, 4 - 8 GHz and 8 - 12 GHz) in comparison to the frequency range covered by 4 resonators in series, a circulator could not be used. The idea was to use a power combiner, which is in principle a circuit consisting of three resistors. This power combiner can be integrated in the measurement setup as shown in fig. 4.2.

This power combiner is not a one-way resistor like a circulator and therefore attenuates

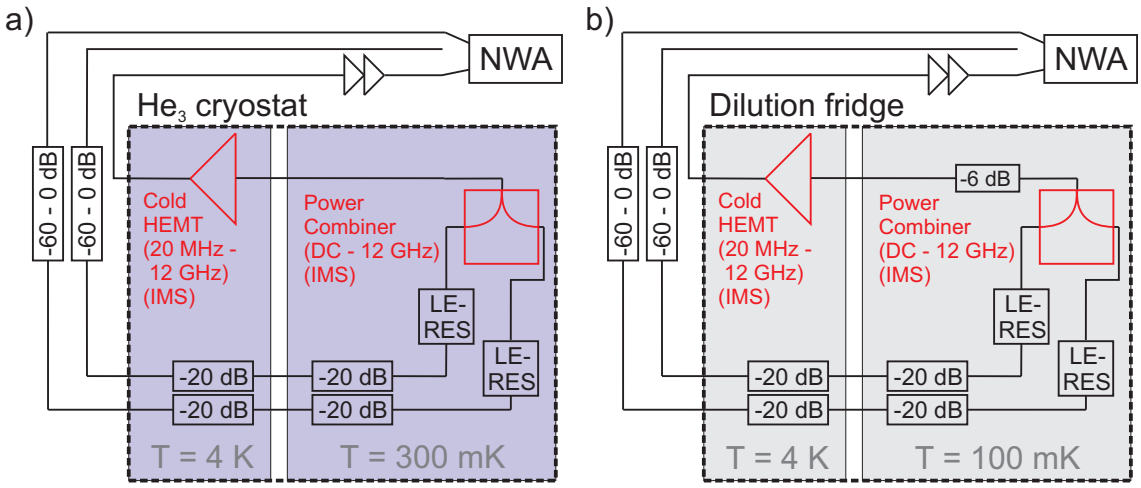

Figure 4.2:
Schematics of the broadband loss measurement setup **a)** for ^{3}He cryostat, **b)** for the dilution fridge. Two identical lines go down from the network analyzer (NWA) to the two samples (LE-RES). -20 dB attenuators are thermally anchored at 4 K and at the coldest stage. Additionally, a -60 to 0 dB step attenuator can be used at room temperature. The two lines are combined by the power combiner (red) and amplified with +25 dB at 4 K by the broadband HEMT (red). The power divider was developed within this thesis while the amplifier was designed by S. Wünsch at the IMS. For the dilution fridge, there is an additional -6 dB attenuator (see text). At room temperature, there are two more +28 dB amplifiers in order to see the signal.

the signal coming from the sample as well. But it still protects the sample from the cold amplifier. The power combiner has another striking advantage. With it, one is able to calibrate when the cryostat including the sample is cooled down, because one line can be used for calibration while the other one is used for measuring. As part of this thesis, such a power combiner with an average attenuation of -8 dB was developed. As it can be seen in figure 4.3b (black curve), the developed power combiner had a -6dB attenuation up to 6GHz, before the attenuation went slowly to -11 dB at around 10 GHz and back to -8 dB at 12 GHz. For frequencies higher than 12 GHz, the influences of parasitic resonances from the housing and the printed circuit board (PCB) do not allow for a proper functionality of the power combiner. However, a range of 100 MHz to 12 GHz was enough for the developed setup, as the upper limit of the used cold amplifier was 12 GHz. An important condition was to achieve two exactly equal input lines of the power combiner in order to use the advantage of cold calibration. This gives the possibility - under the condition that the two lines going to the samples are exactly equal as well - to calibrate out any unwanted effects

over one line, changing the line and then measuring the other line with this calibration. As it is shown in figure 4.3b (red curve), a flat curve can be achieved by calibration over one line of the power combiner and measuring the other one. Even additional noise, as it can be seen in the black curve, can be calibrated out. In the best case, a sample with four resonators can be installed at each site, measured and calibrated. The only condition in this case is that at the site of each resonance, the $|S_{21}|$-curve of the other sample has to be flat. Otherwise, calibration would not be possible. In figure 4.4, the combination of two samples plus power combiner in a frequency range of 10 MHz to 12 GHz is presented. The only critical superposition of two resonances of the different samples can be seen at the second resonance of both resonators. In fact, this is the combination, whose measurement results will be discussed in chapter 5.

The PCB for the power combiner was designed with coplanar waveguide connectors using

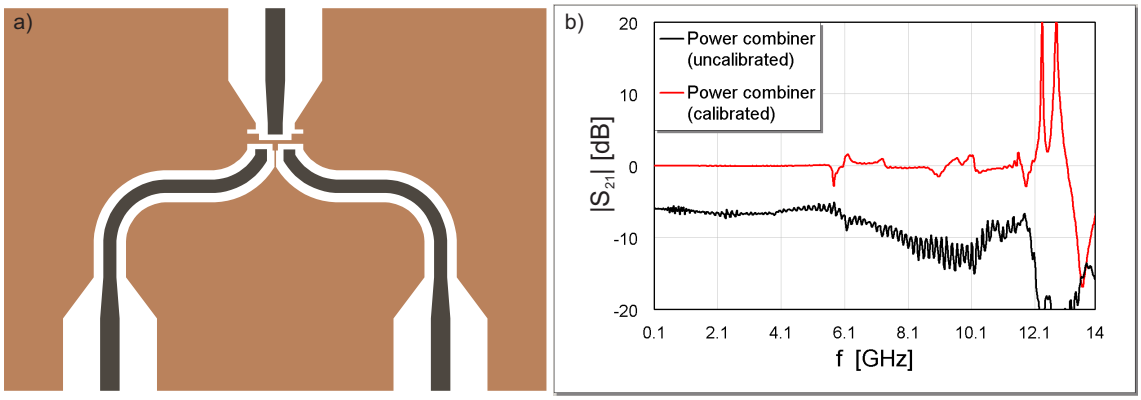

Figure 4.3:
PCB design (a) and performance (b) of the power combiner developed within this thesis for the broadband measurement setup. The feedlines on the PCB were designed as coplanar waveguides (inner conductor colored in dark brown, ground colored in light brown). An average attenuation of -8dB could be achieved up to a frequency of 12 GHz (black curve). Additional, a very good calibration behavior was obtained (red curve).

Sonnet [50]. The PCB design can be seen in figure 4.3a. The PCB material used was TMM10i from Rogers. The power combiner chip used is a Susumu PS2012GT2-R50-T5 and has a specified frequency range from DC to 17.5 GHz. Due to effects of the housing and parasitic resonances from the PCB, the range of the power combiner was limited from DC to 12 GHz. Only in the dilution fridge, the power combiner is followed by an additional -6 dB attenuator. This is necessary to attenuate the thermal 4 K noise of the amplifier down to 160 mK. As in a ^{3}He cryostat the achieved temperatures are not that low, the additional attenuator can be left out leading to a noise temperature of around 400-500 mK.

This attenuation on the outgoing line is needed especially because the semi rigid cable between power combiner and amplifier is made from niobium. Therewith, it gets superconducting and has no attenuation during the measurement.

The outgoing signal is amplified at 4 K by a broadband (20 MHz to 12 GHz) cryogenic

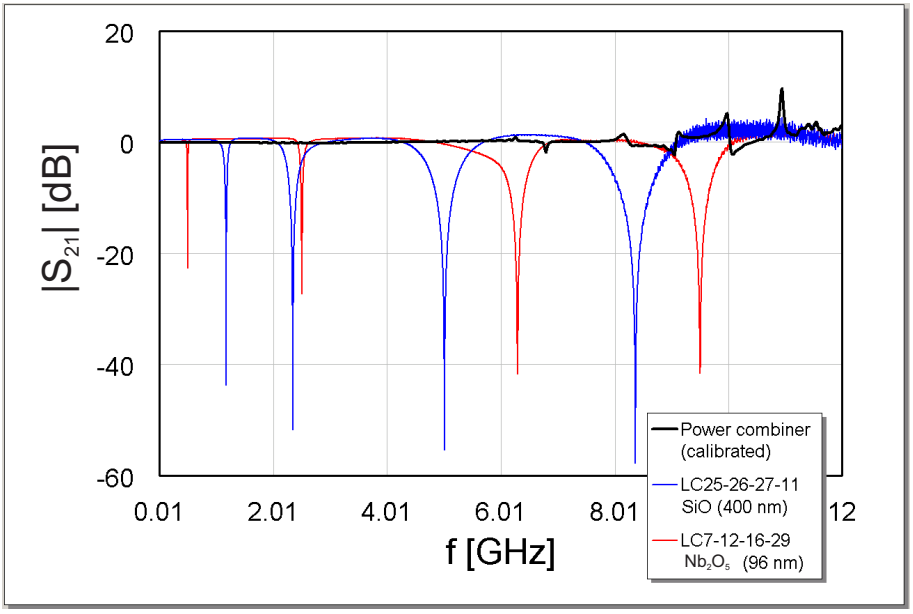

Figure 4.4:
A combination of two multiplexed resonators (red and blue) with four resonance frequencies per sample. Designing the resonances displaced to each other, both samples can be measured in one cooldown cycle with the broadband setup developed within this thesis. The black curve shows that the developed power combiner can be excellently used in the broad frequency band.

HEMT amplifier (+25 dB amplification) designed by S. Wünsch at the IMS. As an alternative, a low-noise cryogenic amplifier No. 060703 developed in the Ukraine with a bandwidth of 4 to 8 GHz, an amplification of +30dB and a noise temperature of 10 K was used to check the noise temperature of the amplifier from the IMS. Since the observed noise contributions, especially at very low power, did not change, it can be assumed that the noise temperature of the broadband HEMT amplifier is low enough and that the amount of noise at the sample is only limited by the power combiner.

As described above, the values of Q_0 can be extracted from the measured resonance dip at by the 3-dB-method, but the measured curves have to be very smooth. Especially in dilution fridge measurements at very low powers, noise comes into play disturbing the smoothness of the measurement curves. For the dilution fridge measurements the internal bandwidth of the used network analyzer (Anritsu MS4642A) was set to 1 Hz to average over the curves because the noise has stochastic nature and can therefore be averaged out to a certain degree. These techniques help to maximize the signal to noise ratio. The power combiner in the presented method limits this signal to noise ratio, because the signal coming from the sample is attenuated. This represents the only real disadvantage of this method. A consequence of this fact is that averaging has to be increased, which reduces the time efficiency of the presented method.

While at high powers (around -55 dBm), only an average factor of 1 to 2 is needed for usable measurement results over 200 to 300 points in the measured bandwidth, at low powers (below -105 dBm) an average factor up to 300 has to be used. However, it is not

possible to achieve really smooth curves at very low powers. Therefore, the 3-dB-method exhibits a significant loss of accuracy. Consequently, another method had to be taken to achieve reliable results. Here, the so called *Lorentzian fit method* was used. This method was suggested by Paul J. Petersan and Steven M. Anlage to be the most accurate and precise measuring tool above a signal to noise ratio of 65 [54].
For this method, a Lorentzian curve is fit to the $|S_{21}|$ versus frequency data using a non-linear least-squares fit [55]

$$|S_{21}|^2 = A \cdot \left(1 + Q^2 \left(\frac{f}{f_0} - \frac{f_0}{f}\right)^2\right). \tag{4.1}$$

Here, Q denotes the quality factor, f the frequency, f_0 the resonance frequency at the minimum of $|S_{21}|$ and A a constant factor. As the fit parameter Q consists of the loaded quality factor Q_L and unloaded one Q_0, the fitting function has to be fitted only to the lowest 3 dB of the resonance curve in order to achieve reliable results. The accuracy of this method was tested by comparing the Lorentzian fit method to the 3-dB-method at high as well as low powers and thus, smooth as well as noisy curves. The relative difference between the two methods was much smaller than 0.01 % for smooth curves, whereas at noisy curves, the relative difference lay above 40 %. Thus, the Lorentzian fit method was used to extract the values of Q_0 and f_0 from the measured curves.

Chapter 5

Experimental Results

In this chapter, the results of the low-temperature measurements will be presented. In section 5.1, the results obtained at 4.2 K will be discussed. As the thermal energy at 4.2 K is high enough for the TLSs to populate their exited states, relaxation processes are clearly dominant and the measurement data can be treated with the theoretical descriptions deduced in section 2.1.2. The results obtained at lower temperatures ($T < 1$ K) using ^{3}He cryostat and dilution fridge cooling techniques will be shown in section 5.2. With decreasing temperature below ($T < 1$ K), thermal energy is not sufficient any longer to populate the excited states. This leads to an increase of TLSs in the ground state. As it was discussed in section 2.1.3, these TLSs try to excite by resonant absorption of photons of the applied elecric field. As it will be shown, the results obtained below $T < 1$ K are in excellent agreement with these resonant absorption processes discussed in section 2.1.3.

5.1 Results at 4.2 K

All measurements in this section were performed at 4.2 K with a ^{4}He bath cryostat, as it was discussed in section 4.3.1. In the first part, investigations done to achieve reliable results will be explained, before results of the frequency dependence of losses and detailed investigations of certain dielectrics will be discussed.

5.1.1 Results at 4.2 K

The first investigation was to determine the influences of the power applied to the resonator. This was done to ensure that no overdrive occurred. In Figure 5.1, the power dependence of the intrinsic quality factor Q_0 is shown. An overdrive occurs for powers higher than -10 dBm. This overdrive can be explained by an increased current density in the inductor bends, leading to a suppression of superconductivity. Thus, all measurements at 4.2 K were carried out in the flat regime between -15 and -27 dBm.

After confirming that the multiplexed resonator design was able to provide reliable results

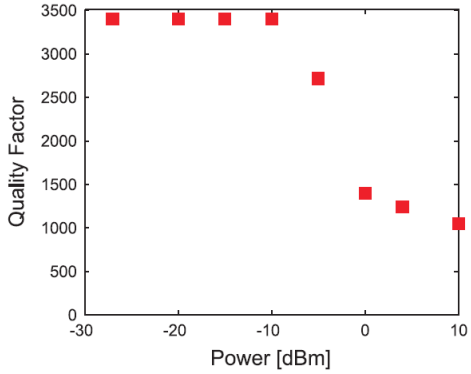

Figure 5.1:
Dependence of the measured quality factor on the applied power [49]. The overdrive is due to the higher current density in the inductor bends.

(see section 3.4), and that overdrive effects could be excluded, the influence of thermal cycling and remounting of the samples was tested. Thermal cycling was done by simply measuring a resonator in a first cooldown, warming it up and subsequently cooling it down and measuring it again. This procedure was repeated several times. Remounting was done by measuring Q_0, warming up the resonator, dismounting the resonator out of his housing, remounting it again and measuring it again in a further cooldown. Very recently, samples fabricated at the beginning of the thesis were measured again after one year of staying in an exicator. The achieved values of Q_0 could be reproduced for the whole series of measurements to a precision better than 0.1%. All these results reflect the reliability and robustness of the developed method and that no aging effects influenced the materials used.

5.1.2 Investigation of Housing Influences on Quality Factors

As mentioned in section 4, for all measurements done at 4.2 K, the resonators were built in brass housing. Due to the fact that at $T < 1$ K the samples were not bath cooled but only thermally connected to the coldest stage via a copper sheet, copper was chosen as new housing material because of its higher thermal conductivity leading to a more efficient cooling of the sample. The resonators assembled in copper housings were first tested at 4.2 K. In figure 5.2, it can be seen that the losses of resonators in copper housings were much lower than the losses of the resonators assembled in brass. This means that the brass housing, acting as ground plane of the resonator, leads to an additional loss contribution. Further in can be seen in figure 5.2 that the differences in losses for brass and copper housings are not the same for SiO and Nb_2O_5. The losses of SiO became smaller by a factor of 2.5 whereas the losses of Nb_2O_5 were lowered by a factor of only 1.2. All results, which will be discussed in section 5.1 were achieved with samples assembled in brass housings. Therefore, all loss measurement data presented in 5.1 will be given in terms of $1/Q_0$ of the extracted intrinsic quality factor. Although this housing influence was found after all the samples had been measured and could not be measured again, yet, the

obtained results are very relevant. As it can be seen in figure 5.2, the frequency dependence obtained with brass housing is equal to that obtained with copper one. This means that the frequency dependence of the dielectric loss was not influenced by the housing. Solely the absolute loss values were superposed by a constant offset value of the brass housing. For all measurements at $T < 1$ K, copper housing was taken.

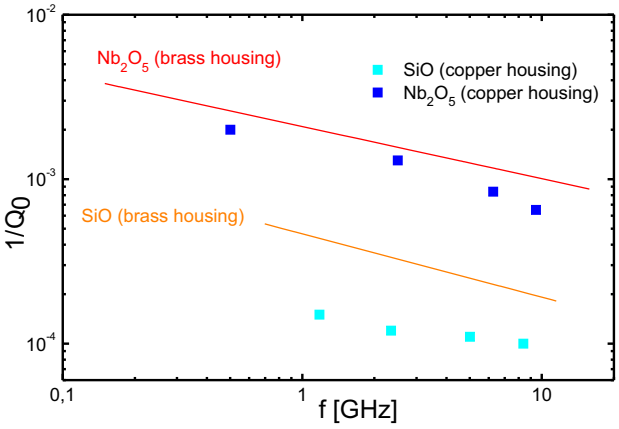

Figure 5.2:
Frequency dependence of losses for SiO (red) and Nb_2O_5 (violet) in copper housing. The solid lines are taken from 5.3 as these lines were achieved in brass housing. Less loss can be observed for samples in copper housing. The frequency dependence stays the same, only the absolute loss value changes, but in a different way for the two dielectrics. The contribution of the brass housing is a constant offset, which does not influence the frequency dependence of dielectric losses.

5.1.3 Frequency Dependence of Dielectric Loss

As it was discussed in section 3, TLSs causing dielectric loss are also responsible for the main decoherence mechanism in superconducting phase qubits. Thus, the loss of different dielectrics usually used in qubit fabrication should be investigated. Furthermore, the frequency dependence of the dielectric losses was of great interest. Thus, various resonators with a variety of dielectrics (Nb_2O_5, SiO, SiN_x and a-Si:H) were tested.
The results for the frequency dependence of the losses of amorphous dielectric thin films are shown in figure 5.3. All SiN_x data as well as part of the Nb_2O_5 and SiO data was obtained before the start of this thesis. Within this thesis, more data for Nb_2O_5 and SiO was gathered using multiplexed resonators. Furthermore, all a-Si:H samples fabricated by the collaborating group at ICIB in Naples were measured within this thesis. For completeness all data points were taken into account for the interpretation. The measurements carried out before the start of the thesis are discussed in detail in [49]. Additionally, a detailed description of the losses in multi-layer dielectrics is given there, whereas this thesis is only dealing with losses in single layers.

As it can be seen in figure 5.3, the material with the highest loss is Nb_2O_5. Furthermore, it can be seen, that the absolute values of the losses in different materials compare to each other as expected, for example from [9]. It is obvious, that the lower the oxygen contribution in the dielectric the lower the loss (SiO $\rightarrow$ SiN_x $\rightarrow$ a-Si:H). This leads to the conclusion that the origin of the TLSs lies in defect states like OH^- bonds in the

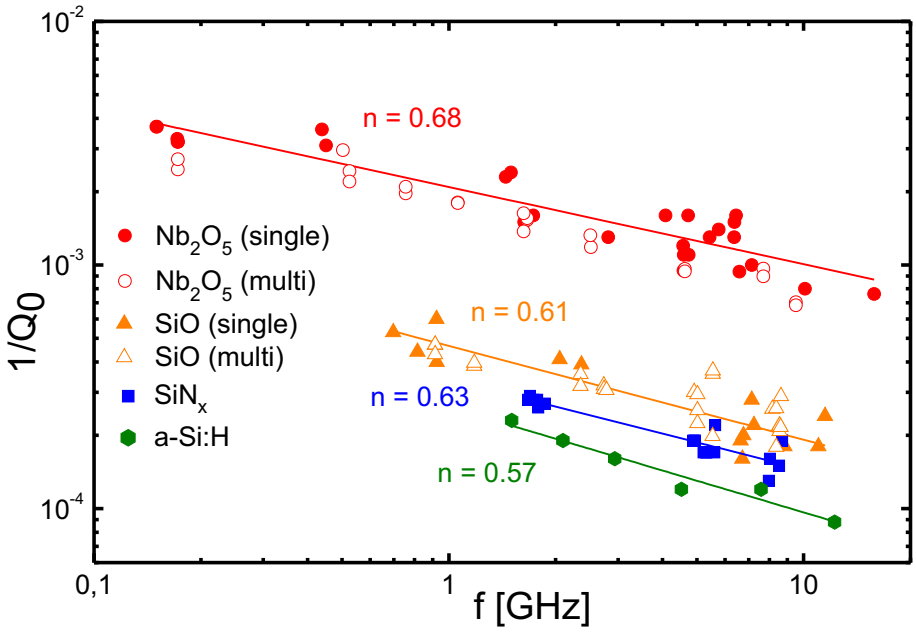

Figure 5.3:
Frequency dependence of dielectric losses in different amorphous thin films (usually used in Josephson junction fabrication). The fits (solid lines) to (2.37) show that the data is in agreement with the universal law and the exponents n are in the range related to many-body interacting dipoles [19]. The filled symbols represent measurements performed with single resonators, while the transparent ones represent measurements performed with multiplexed resonators.

dielectric.

As it was discussed in the beginning of this section, the behavior of TLSs at 4.2 K is dominated by relaxation processes. Thus, the universal law, explained in Section 2.1.2, was taken to describe the frequency dependence of the dielectric losses of the different materials. Therefore, the relations $\tan\delta = 1/Q_0 \propto \chi''$ and $\chi'' \propto \omega^{n-1}$ were used to fit the data. As is illustrated in Figure 5.3 by the fits (solid lines), the universal law was able to explain the observed frequency dependence of the losses. Since the found exponents were $0.57 \leq n \leq 0.68$ for all investigated amorphous dielectric thin films, it can be concluded that the TLSs behave like dipoles with many-body interaction (see predicted values of n in Section 2.1.2).

As the data obtained by single resonators and by multiplexed ones were carried together and no difference can be seen the reliability of the new multi-plexed resonator design could be proved again.

A rather large spread of the measured Q_0 values for each material was apparent. This spread was not caused by the measurement procedure and found to be the same for samples from different or the same processing runs. It seems to be in the nature of such materials research, and a large number of samples was measured to allow fitting to the data.

In order to exclude a dependence of the thickness of the dielectrics, the thickness was varied. A thicker dielectric changes the distance d of the plate capacitor and therewith its

capacitance

$$C = \varepsilon_0 \varepsilon_r \frac{A}{d}. \tag{5.1}$$

Here, ε_0 denote the electric constant, ε_r the permittivity of the dielectric between the plates, and A the area of the plates. As a thicker dielectric changes the capacitance of the resonator a change in resonance frequency occurs. The obtained value $\tan\delta = 1/Q_0$ at this frequency is in excellent agreement with the the universal law. Therefore, it can be claimed that the measurement method is independent of the geometry [49]. This means, that no dependence of the losses on the dielectric film thickness was found. This is not surprising for such lossy amorphous materials and shows that the bulk losses exceed the interface losses by far.

5.1.4 Detailed Investigation of Nb_2O_5 and AlO_x

The Nb_2O_5 films which were investigated so far were created by anodic oxidation in an aqueous solution of $(NH_4)B_5O_8$ and $C_2H_6O_2$ at room temperature. As Nb_2O_5 is commonly used in the fabrication of Nb-based superconducting qubits, it is desirable to reduce its high losses (see figure 5.3). In semiconductor industry, electrolytes like aqueous solutions of H_2SO_4 and H_3PO_4 are often used because this lead to a lower losses [56].
Thus, these electrolytes were employed for anodic oxidation at the IMS to figure out if lower losses could indeed be achieved. In figure 5.4, the losses over frequency are shown for Nb_2O_5 made with the different electrolytes. The data shows that no decrease of loss could be achieved. This could be due to the fact that in semiconductor industry, granular Nb is used to make Nb_2O_5 [56] instead of sputtered Nb as in this thesis. The loose cohesion in a granular may favor the growth of Nb_2O_5 with lower loss than it is the case in amorphous sputtered Nb.

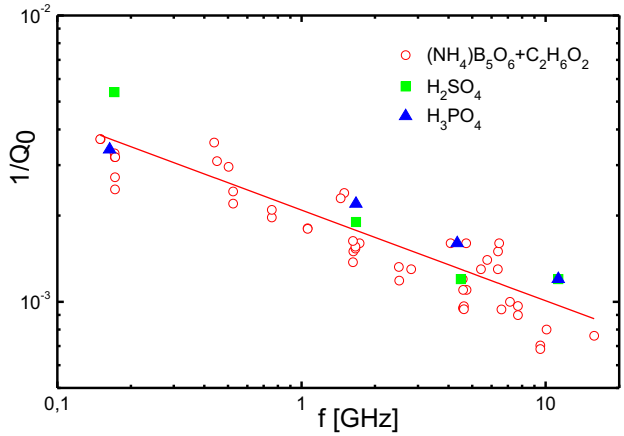

Figure 5.4:
Frequency dependence of losses (in terms of $1/Q_0$ for Nb_2O_5 made with different dielectrics. The absolute values as well as the exponents n coincide for all different fabrication techniques.

5.1.5 Detailed Investigation of a-Si:H

Hydrogenated amorphous silicon (a-Si:H) was recently suggested [9] for qubit fabrication because of its high coordination number leading to low loss. The additional saturation with hydrogen reduces the possibility for OH^- groups to act dipole-like, extracting energy from the environment.

As it can be seen in Figure 5.3, a-Si:H showed the lowest losses among the investigated materials. To investigate if the losses could be decreased, the surface of the Nb under the a-Si:H was treated to reduce surface TLSs (which were discussed in section 3). The Nb was *in-situ* with its sputtering nitridized or covered with Si in order to protect the surface of oxidizing and therewith avoid surface losses. The idea of reducing surface loss among resonators with a-Si:H is reasonable as these resonators are the only ones exhibiting bulk losses down to 10^{-5}.

In Figure 5.5, the results for the standard process are compared to the modified fabrication techniques. Surprisingly, the losses were much higher for the two modified processes than for the standard one, and they were even higher than the losses in SiO.

A possible reason for this is the so-called "poisoning" of Nb by hydrogen impregnation due to the hydrogenation of the amorphous Si (for further details of this process see [57]). In principle this poisoning leads to a reduction of the superconducting transition temperature. This leads to an increase of the surface impedance R_s of the Nb which is, according to (2.63), proportional to frequency in the order of ω^2. Thus, this poisoning should lead to a different frequency dependence of the losses in the measurements. However in figure 5.5, the frequency dependence of the losses obtained with the two modified techniques have the same as the losses obtained by the standard process. This leads to the assumption that poisoning is not the reason for this increase of loss.

But it is to mention that as all samples with a-Si:H were fabricated at the ICIB in Naples the author can only speculate about the obtained results.

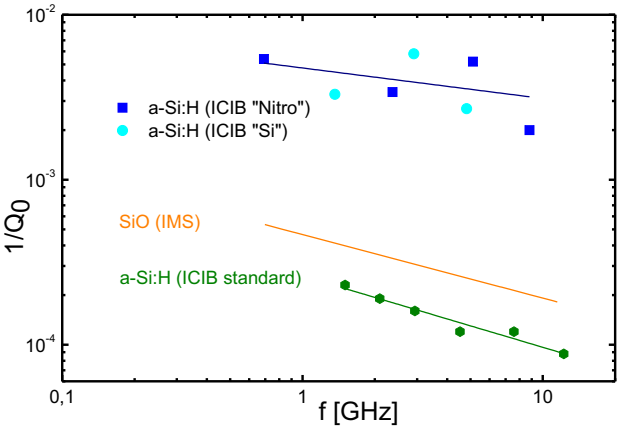

Figure 5.5:
Frequency dependence of losses (in terms of $1/Q$) for a-Si:H fabricated in different process runs. a-Si:H fabricated in the standard process (blue) has least loss. a-Si:H fabricated onto an additional Si layer ("Si") and onto nitridized Nb ("Nitro") show much more loss Reason for this can only be speculated (see text).

5.2 Results at Temperatures $T < 1$ K

The presented method consisting of the multiplexed resonator design (see section 4) and the broadband setup (see section 4.3.2) gives the possibility to investigate dielectric losses at mK temperatures not only in dependence of temperature and power but also with regard to frequency. All these dependences can be investigated in one cooldown cycle with multiplexed resonators fabricated in the same process. Thus, it is possible to investigate the frequency dependence reliably. This would be not possible in the case of e.g.obtaining results with several cooldowns as the complete system can change in any cooldown. In the next two sections, the temperature and power dependence will be investigated separately for each single resonator before the achieved values will be compared and thus, the frequency dependence investigated. For all measurements at temperatures $T < 1$ K, copper housing were used.
The data presented in the next sections were obtained with one chip. The properties of the four resonators on this chip are listed in table 5.1.
It has to be mentioned that LC11 was defect on this chip. Therefore, the investigations

Chip name	Dielectric material	ε_r	Thickness [nm]
LC25-26-27-11 SiO400	SiO	5.7	400
Resonator name	**C [pF]**	**L [nH]**	**$f_{0,\text{design}}$ [GHz]**
LC25	11.36	1.8	1.11
LC26	2.84	1.8	2.23
LC27	1.02	1.0	4.98
LC11	0.53	0.7	8.24

Table 5.1:
Parameters of the chip with which all measurement results at $T < 1$ K were performed.

could only be performed at three frequencies. However, this confirmed the reliability of the developed multiplexed resonator design, as the malfunction of one resonator did not influence the performance of the remaining ones.
The power values in the next sections are mostly given in units of dBm. These values were obtained by summarizing the applied output power of the network analyzer and the attenuation values of the attenuators as well as of the cables, which were given in section 4.3.2. Power values in dBm can easily transformed to W by

$$P[\text{W}] = 10^{\text{P[dBm]}/10} \cdot 1\text{mW}. \tag{5.2}$$

5.2.1 Temperature and Power Dependence of Dielectric Losses

In figure 5.6, two measurements curves for measurements at high power (-55 dBm) and low power (-110 dBm) are shown. As can be seen, the noise in the signal at low powers was much stronger than at high powers. This was not surprising as the power for these two curves differed by more than five orders of magnitude, whereas the noise contribution

stayed the same. In the two figures the data (blue points) was fitted (red lines) with (4.1). The fits were obtained with Matlab [53], which gave values for the 95 % confidence bounds, which are the bounds of plus and minus one σ (standard deviation). In figure 5.6c the relative error σ/Q_0 of the intrinsic quality factor Q_0 is plotted over the applied power. In the case of -110 dBm, this means that the fitted absolute value of the Q_0 has a relative error of $\sigma/Q_0 = 9\%$, which is tolerable for the following investigations. The dielectric loss is extracted from the measured unloaded quality factor Q_0 as $\tan\delta = 1/Q_0$.

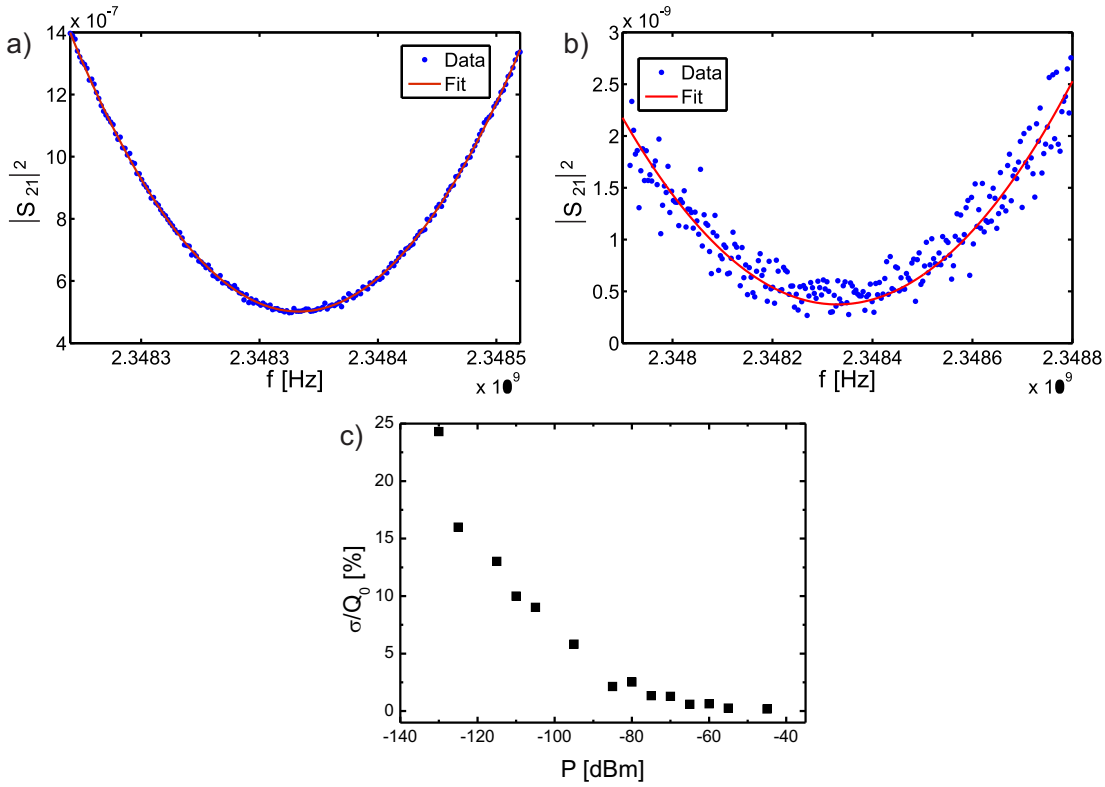

Figure 5.6:
a) Data and fit for a measurement curve obtained at -55 dBm. In this high power regime, the observed noise level is very small. b) Data and fit for a measurement curve obtained at -110 dBm. In the low power limit, noise influence increases. In c), this influence of the noise is given in form of a relative error, showing that for very low powers the error increases clearly.

In figure 5.7, the temperature dependences of the losses of each resonator at certain power levels are shown. These data were achieved in the dilution refrigerator by cooling down to base temperature (106 mK in this case), measuring each resonator at each power level, warming up to the next temperature and measuring each resonator at each power level again. It can be observed in each plot (meaning for each frequency) that below a power level of around -80 or -85 dBm, the losses increase with decreasing temperature. Below -85 dBm, the losses are rather constant or slightly decreasing with decreasing temperature. The losses seem to be saturated for higher powers and temperatures, which was discussed in section 2.1.3.

In figure 5.8, the power dependences of the losses of each resonator at certain temperatures

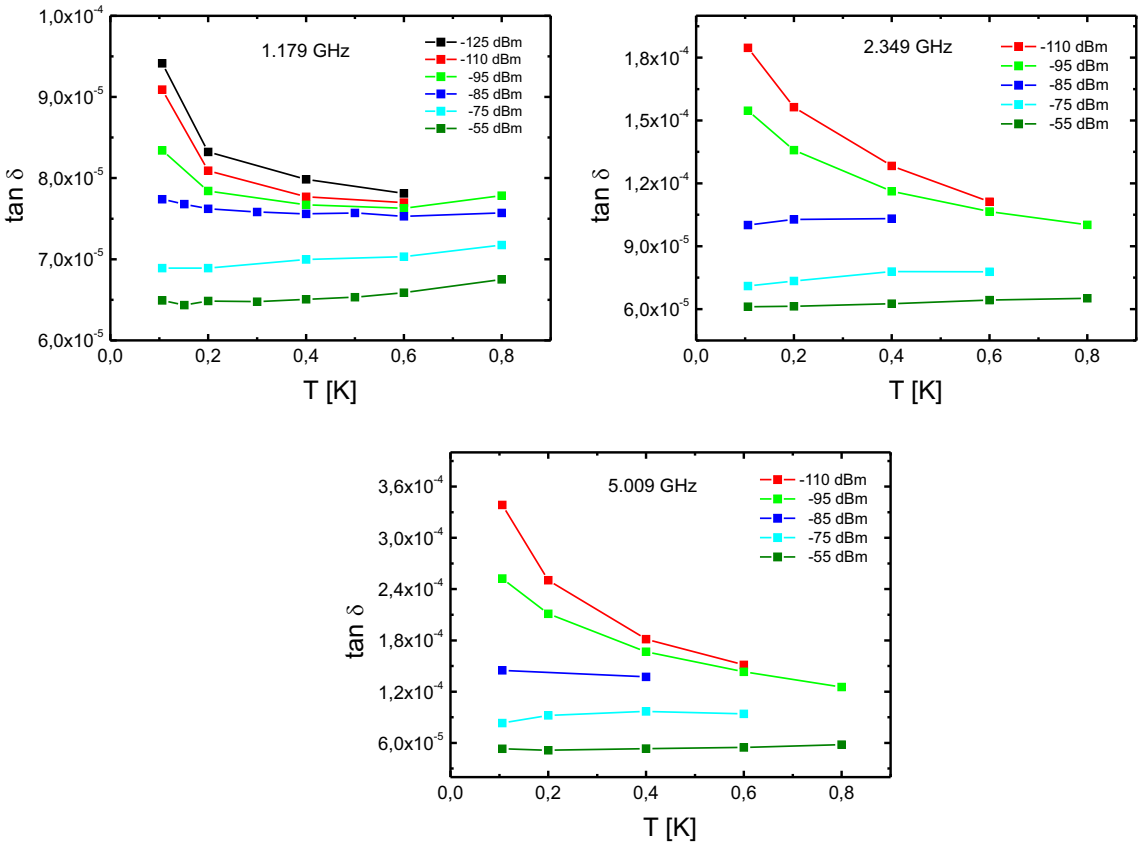

Figure 5.7:
Each plot shows the temperature dependence of the loss at various power levels for one resonator. Going below a certain power, an increase of loss with decreasing temperature is observable. This is due to resonant interaction between the TLSs in the dielectric and the applied field.

are shown. It is the same data as in figure 5.7, only plotted over the applied power. For each temperature and frequency, the losses exhibit flat plateau at high power levels (-45 to approximately -75/80 dBm) fading to a linear power level regime (-85/90 to approximately -110/115 dBm) before reaching a rather flat plateau at low power levels below -110/115 dBm. In reference to literature [14], this plateau shall be called the *low power limit*.

As the observed dependencies of temperature and power are qualitatively the same for all investigated frequencies and as measurements at 4.2 K have confirmed that only the TLSs in the dielectric contribute to the measured losses, it can be claimed that the effects shown in the figures 5.7 and 5.8 are due to the TLSs in the dielectric (SiO in this case) between the capacitor plates of the resonator.

The described loss behavior with temperature and power is comparable to the behavior of TLSs in bulk glasses (see section 2.1.3) or in surfaces of CPWRs (see section 3). This leads to the assumption that the same processes are responsible for the observed behavior of TLSs in bulk glasses, surface layers as well as bulk dielectrics. This must be due to the same nature of TLSs in all these investigated fields. The fact that the obtained temperature

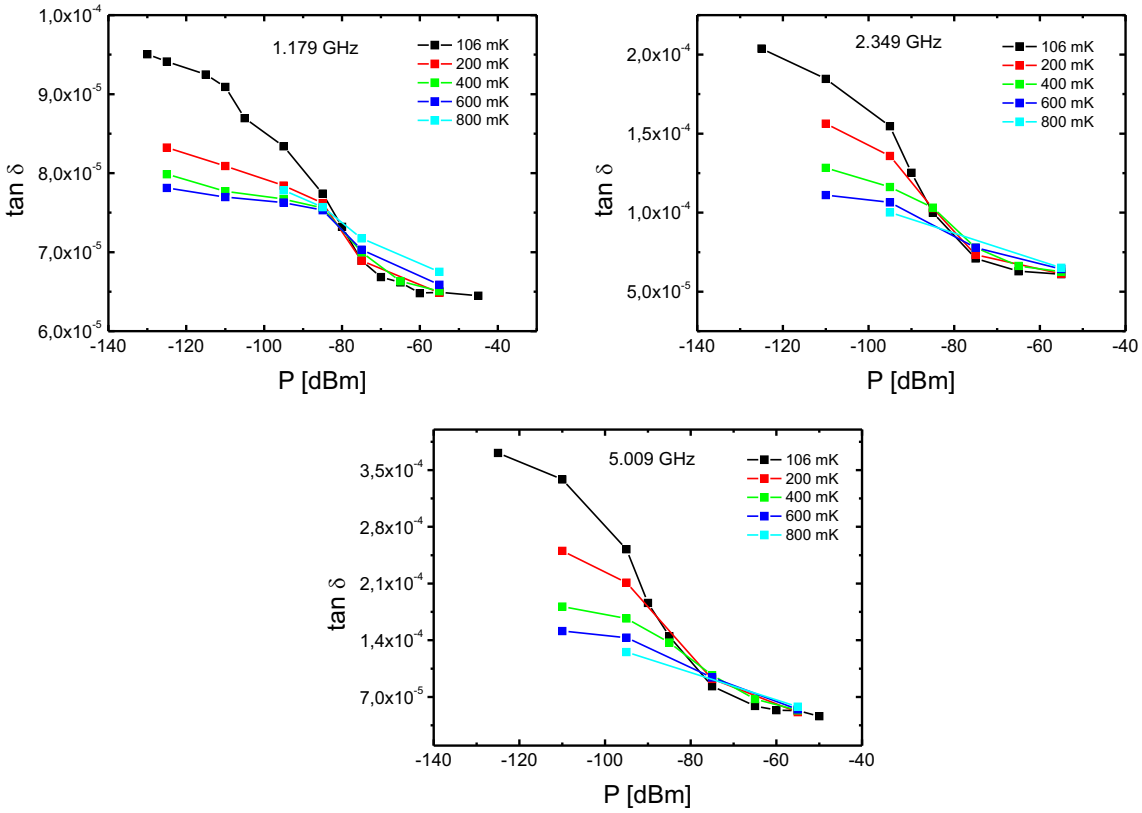

Figure 5.8:
Each plot shows the power dependences of the loss at certain temperatures for one resonator. For the visible saturation effect, see text.

and power dependencies at $T < 1$ K within this thesis were in excellent agreement with the description for resonant absorption in terms of the tunneling model (see section 2.1), supported this assumption.

As in the low power limit, there is nearly no power dependence of the losses (nearly flat niveau) one can neglect the power dependence and evaluate the temperature dependence separately. Under this condition, the temperature dependence of the losses can be deduced with help of the tunneling model (see section 2.1.3 and [16]):

$$\tan\delta = \tan\delta_{\mathrm{sat}} + F\alpha \tanh\left(\frac{hf_0}{2k_{\mathrm{B}}T}\right). \tag{5.3}$$

Here, α is the same as (2.32). F is the forming factor (see (3.4)) introduced by Gao [12], expressing the ratio of the electric energy w_h^e stored in the TLS-loaded volume V_h to the total electric energy w^e stored in the entire resonator. In the presented case of lumped element resonators with the entire electric field in the TLS hosted dielectric between the plates, the forming factor F can be assumed to be unity. This means that the factor α which expresses the intrinsic properties of a TLS in the dielectric can be obtained directly out of the fit to (5.3). Furthermore, f_0 denotes the resonance frequency and $\tan\delta_{\mathrm{sat}}$ denotes the constant loss caused by TLSs that are saturated by thermal energy or power. As it

was discussed in section 2.1.3, a saturation of TLSs is given when there is enough energy for the TLSs to populate the excited states. When the occupation number (see (2.24)) becomes 0 at high enough energies, ground and excited states are equally populated and resonant absorption is dominated by relaxation processes. The constant loss in this limit is $\tan\delta_{\mathrm{sat}}$. Thus, it is obvious, that the increase of loss with lowering temperature can be explained with the difference in occupation number leading resonant absorption to become dominant. This was explained in detail in section 2.1.3. There, it was also discussed that for sufficiently low temperatures, the loss will reach its maximum. The temperature at which the maximum loss is reached depends on the energy splitting and therewith on the frequency(as it was shown in section 2.1.3). This means, that the higher the frequency the higher the limiting temperature. Only for the highest investigated frequency of 5.01 GHz in this thesis could be nearly observed. In figure 5.9, one can see by the interpolation of the fits that only in the case of 5.01 GHz a saturation has started, whereas the lower frequencies show no saturation yet.

As it was explained above, (5.3) is fitted in the low power limit for all frequencies, which

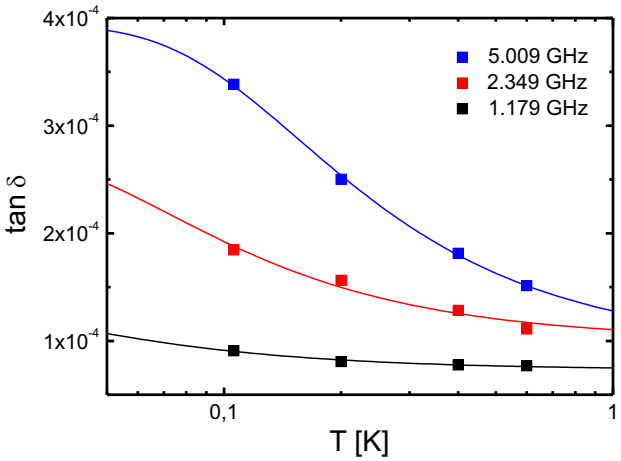

Figure 5.9:
Loss data for each resonator at a power level of -110 dBm, which is the beginning of the low power limit. Solid lines are fits to (5.3).

is shown in figure 5.9. Here, $P = -110$ dBm is chosen because this value represents the beginning of the low power limit, but has still a small relative error (see figure 5.6). The fitting parameter values for all frequencies are shown in table 5.2.

Resonace frequency f_0 [GHz]	$\tan\delta_{\mathrm{sat}}$	α
1.179	$7.3 \cdot 10^{-5}$	$6.60 \cdot 10^{-5}$
2.349	$1.0 \cdot 10^{-4}$	$1.80 \cdot 10^{-4}$
5.009	$9.17 \cdot 10^{-5}$	$3.02 \cdot 10^{-4}$

Table 5.2: Values of $\tan\delta_{\mathrm{sat}}$ and α obtained from the fits (solid lines) in figure 5.9. The values of α are different for different frequencies.

In comparison with the $F\alpha$ values obtained by CPWR measurements investigating surface losses, the α values (remember that $F = 1$) obtained here are at least one order of magnitude higher. This leads to the conclusion that the TLS density is much higher here

than in CPWRs, where the TLSs are situated only in a volume within the entire electric field. The comparison of the values for different frequencies will be done in section 5.2.2. Here, it shall just be mentioned that the α values are not equal as assumed in (5.3), where α is not frequency dependent.

In the next step, the power dependence of the losses shall be investigated in more detail. When power levels higher than -110 dBm are applied, the linear regime described above (see figure 5.8) is entered. This was explained in section 2.1.3 as high power limit under the influence of strong electric fields. In other words, a power dependence of the losses has to be taken into account. With this additional power dependence, (5.3) is extended to [16, 30]

$$\tan\delta = \tan\delta_{\mathrm{sat}} + F\alpha\left(1+\frac{P}{P_{\mathrm{c}}}\right)^{\phi}\tanh\left(\frac{hf_0}{2k_{\mathrm{B}}T}\right). \tag{5.4}$$

$\left(1+\frac{P}{P_c}\right)^{\phi}$ will be called $f(P)$ from now. Here, P is the power of the applied field, P_{c} is a critical power for the crossover from the linear regime to the low power limit and the exponent ϕ is predicted to be equal to -0.5 (the exact deduction follows out of Bloch equations and can be found in [2, 16, 30]). In order to investigate the power dependence separately, one has to normalize with respect to temperature by eqúating

$$f(P) = \frac{\tan\delta - \tan\delta_{\mathrm{sat}}}{\alpha\tanh\left(\frac{hf_0}{2k_{\mathrm{B}}T}\right)}. \tag{5.5}$$

With the values given in table 5.2, any obtained loss value for each frequency can be normalized with respect to power. In figure 5.10, the normalized loss values for each frequency below a power level of -85 dBm and at a temperature of 106 mK are shown.

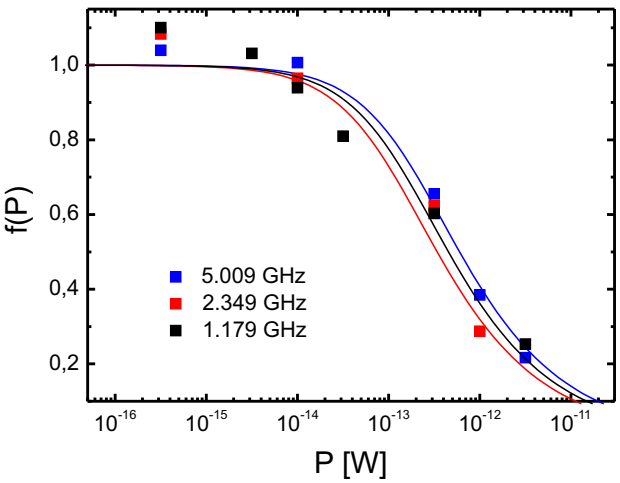

Figure 5.10:
Power dependences $f(P)$ of loss values normalized with respect to power at $T = 106$ mK for all frequencies with fits (solid lines) to (5.5). All data points and fit curves lay nearly congruent. Consequently, the power dependence can be assumed to be frequency independent.

Power is given in units of W to be comparable with literature e.g. [14]. In table 5.3 the fitted values of P_c and ϕ for each frequency can be seen. Although the values of P_{c} and ϕ are not completely the same, it can be seen that for all frequencies, the normalized $f(P)$

Resonace frequency f_0 [GHz]	P_c [W]	ϕ
1.179	$9.7 \cdot 10^{-14}$	-0.38
2.349	$3.93 \cdot 10^{-13}$	-0.9
5.009	$3.17 \cdot 10^{-13}$	-0.69

Table 5.3: Values of the critical power P_c and ϕ obtained from the fits (solid lines) in figure 5.10.

curves as well as the solid lines which are fits to (5.4) are nearly congruent. Consequently, the power dependence can be assumed to be frequency independent. Furthermore, the values of ϕ are close to -0.5, the value predicted from the theory (see section 2.1.3).
The deviations in the values of P_c and ϕ are assumed to arise from the high relative error σ/Q_0 (see figure 5.6) for very low powers ($P < -110$ dBm). An evidence for that can be seen in figure 5.10 at very low powers (left site) where the $f(P)$ values deviate most from the fitted curves.

As a last step, the original measured loss data at each frequency will now be normalized with the help of the obtained values in tables 5.2 and 5.3 in the following way

$$\tan\delta_N = \tan\delta_{sat} + \frac{\tan\delta - \tan\delta_{sat}}{f(P)}. \tag{5.6}$$

Here, $\tan\delta_N$ denotes the complete normalized loss, not only with respect to power but also with respect to $\tan\delta_{sat}$. This makes it possible to normalize all temperature dependence curves at any power level smaller than -85 dBm (this is the power level were the linear regime starts). This can be seen in figure 5.11 for each frequency. For each frequency, the curves are nearly congruent. The deviation, meaning the small spread of the points at each temperature is assumed to be due to the relative error entering the fitted values from the power dependence fit.
The fact that such a normalization works with the formulas deduced from the tunneling model for resonant absorption, suggests that the behavior of the TLSs in the dielectric below a power level of -85 dBm is clearly dominated by resonant interaction between TLSs and the applied field. Above -85 dBm, this behavior cannot be observed due to the fact that the TLSs are saturated due to power in this power regime.

5.2.2 Temperature Dependence of the Resonance Frequency

As described in section 2.1.3, the losses are directly connected to the imaginary part χ'' of the complex susceptibility $\chi(\omega)$. With the help of the Kramers-Kronig relation (2.44), it is possible to obtain the real part χ' of the complex susceptibility out of χ''. The real part ε' of the complex permittivity is directly connected with χ' (see (2.26)). Thus, using (2.44), a change in the permittivity ε' with temperature is predicted (2.45). As a change in the permittivity of the dielectric changes the capacitance of the resonator, the resonance frequency changes as well. This can be seen in figure 5.12, where the relative frequency

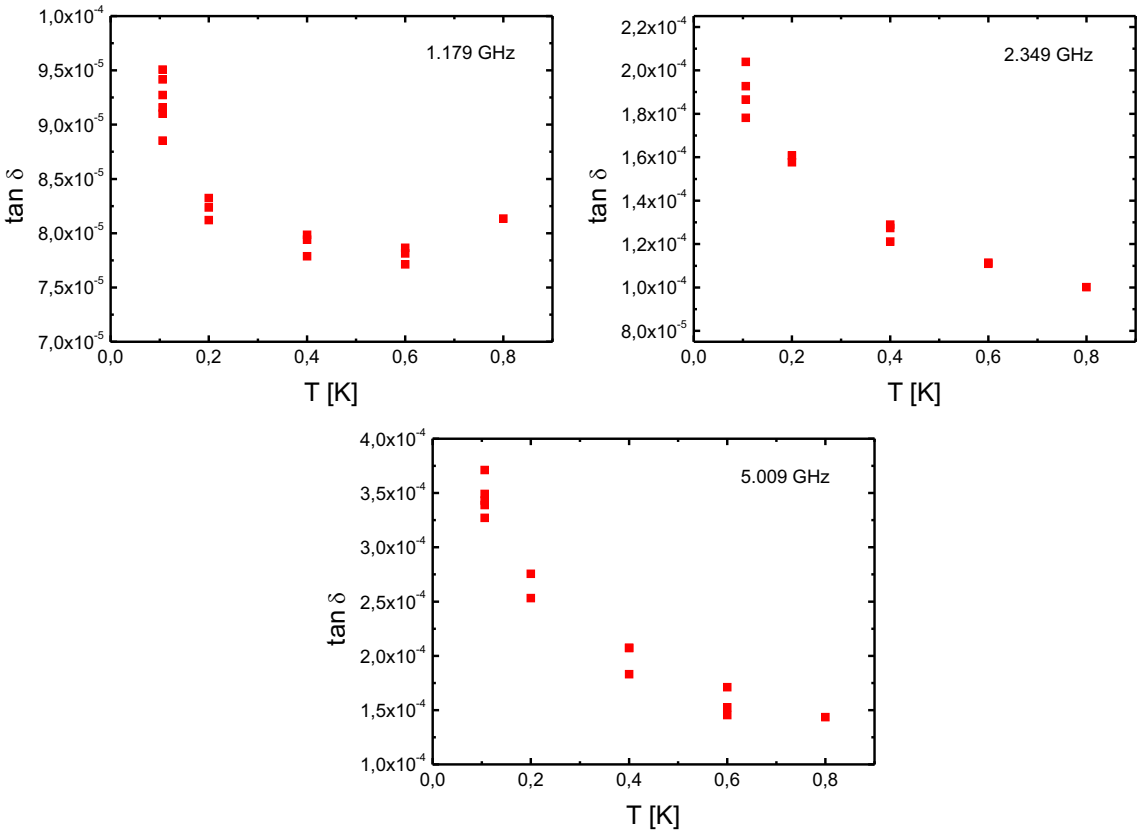

Figure 5.11:
All curves below a power level of -85 dBm for each resonator of figure 5.7 are normalized via (5.6). The normalized curves are nearly congruent for each resonator exhibiting a small spread due to the relative error given in figure 5.6.

shift $\Delta f_0/f_0(T_0) = (f_0(T) - f_0(T_0))/f_0(T_0)$ with $T_0 = 106\text{mK}$ is plotted over temperature. For all frequencies, it can be seen that the resonance frequency shifts to higher frequencies for increasing temperature.

The mathematical description of how a change in permittivity affects a change in resonance frequency was deduced in [12]. The frequency shift is predicted as (3.6)

$$\begin{aligned}\Delta f_0/f_0(T_0) &= (f_0(T) - f_0(T_0))/f_0(T_0) \\ &= \frac{F\alpha}{\pi}\left[\ln\left(\frac{T}{T_0}\right) - \left(\operatorname{Re}\psi\left(\frac{1}{2} + \frac{\hbar\omega}{2\pi i k_\mathrm{B} T}\right) - \operatorname{Re}\psi\left(\frac{1}{2} + \frac{\hbar\omega}{2\pi i k_\mathrm{B} T_0}\right)\right)\right]. \quad (5.7)\end{aligned}$$

Again, as it was discussed for the presented resonator design, the filling factor F can be assumed to be unity. Thus, a fit of (5.7) to the measured frequency shifts offers a second possibility to obtain values for α.
For temperatures $T < 1$ K, the logarithmic term in (5.7) is dominant, leading to a decrease of resonance frequency for decreasing temperature. In figure 5.12, the shifts in resonance frequency for each resonator are fitted to (5.7). The obtained values for α can be found in

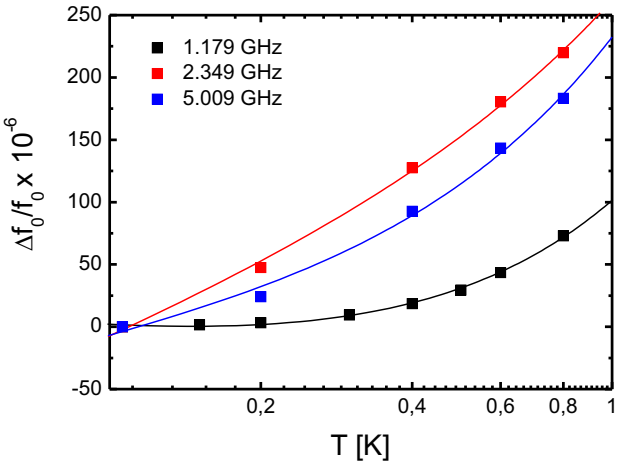

Figure 5.12:
Relative frequency shifts of the resonant frequencies plotted over temperature. The behavior can be described and fitted (solid lines) by (5.7).

table 5.4.

It is visible that the values of α are not equal for the different frequencies. Furthermore,the

Resonace frequency f_0 [GHz]	α
1.179	$8.17 \cdot 10^{-5}$
2.349	$2.13 \cdot 10^{-4}$
5.009	$2.57 \cdot 10^{-4}$

Table 5.4: Values of α obtained by the fits shown in figure 5.12. The values are different for different frequencies.

obtained values differ slightly from those obtained by the loss measurements. This will be discussed in more detail in the next section.

Another interesting observation can be made. (5.7) predicts an increase of the relative frequency shift for decreasing frequencies. This is not confirmed by the data shown in figure 5.12, since the durve for $f_0 = 1.179$ GHz exhibits the lowest $\Delta f_0/f_0$ values. This leads to the assumption that an additional frequency dependence is present, which will be discussed in the next section.

Additionally, (5.12) predicts an upturn in the frequency shift for $2k_\mathrm{B}T < hf_0$. In other words, the frequency shift increases with decreasing temperatures below $T_\mathrm{ground} < \frac{hf_0}{2k_\mathrm{B}}$. This limit was discussed for losses as well (see above). As the lowest measuring temperature was 106 mK, this upturn only could have been observed for the resonance frequency of 5.009 GHz, because at this frequency $T_\mathrm{ground} = 120$ mK. However, no beginning upturn was observable for 5.009 GHz. But as this upturn was shown to be very flat around T_ground (see [12, 58]), it is not surprising that it is not visible here.

5.2.3 Frequency Dependence of the TLSs

As was discussed in section 3.1 and as can be found in [16], the values for α both obtained from loss and from the frequency shift have been found equal for the same material. This

went along with the assumption of the tunneling model [30] that the TLS density of states n, which is part of the factor α, is frequency independent. In general, however, n can be frequency dependent [30]. This can be explained as follows. The Kramers-Kronig relations are used to deduce the change in permittivity (which is connected to the real part of the complex permittivity) from the mathematical description of the losses (which is connected to the imaginary part of the complex permittivity). As was discussed in the previous section and in section 2.1.3, the power dependent part $f(P)$ vanishes in this calculation. This is why there is no power dependence in (5.7), and indeed no power dependence could be seen in the frequency shift measurements carried out in the previous section. The reason for this is that the major contribution to the Kramers-Kronig relation comes from states for which $\frac{hf}{k_\mathrm{B}T}$ is close to unity, and which are therefore much more difficult to saturate than those for which $hf \ll k_\mathrm{B}T$ (for more details please see [30]). Consequently, it was predicted that TLSs sampled in a measurement of the change of the permittivity (which is represented by the frequency shift measurement here) have a larger energy splitting than those probed in loss measurements at the same frequency. This is why the obtained α values do not need to be identical in these two measurements if n is frequency dependent [30]. As $E = hf_0$, energy and frequency dependent are here equivalent. This is exactly what can be seen comparing the values of α in tables 5.2 and 5.4. Comparing the α values in 5.2 with each other shows that they are different. The same can be found for comparing the α values in table 5.4 with each other. It can be seen that in both cases the α values increase with increasing frequency. Comparing the α values for the same frequencies of tables 5.2 and 5.4 with each other, they are found to be (slightly) different. In other words, the α values obtained from loss measurements are not equal to that obtained by frequency shift measurements. If the TLS density of states was frequency independent, all α (for all frequencies in both tables) would be the same. As the α values obtained within this thesis are not equal, though, this leads consequently to the conclusion, that the TLS density of states is frequency dependent.
This is clearly shown in figure 5.13, where the three plots of figure 5.11 are plotted into one plot. As all three curves are normalized with respect to power and $\tan\delta_\mathrm{sat}$ and α is assumed to be the same for all three frequencies, all three plots would have to be congruent. But as is obvious, the loss values rise with increasing frequency.

The influence of this frequency dependence of the density of TLS states on the losses can nicely be discussed in figure 5.14. Here, the losses at certain power levels are plotted over frequency at a temperature of 106 mK. The frequency dependence of the losses changes completely with decreasing power. The frequency dependence at high powers is similar to the observed at 4.2 K caused by relaxation effects of TLSs. This confirms that when the available energy (by power like here or by temperature like at 4.2 K) is sufficient to saturate the TLSs, relaxation effects clearly dominate resonant processes by far. On the other hand, the frequency dependence becomes completely inversed entering the regime of

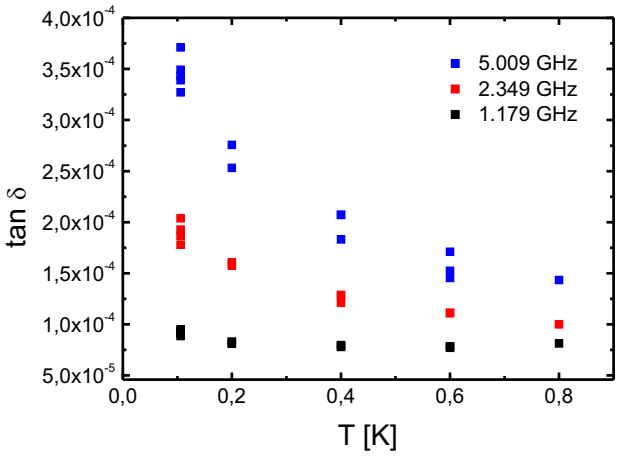

Figure 5.13:
Here, all three curves of figure 5.11 are plotted into the same diagram in order to see the frequency dependence of the losses.

resonant interaction (here, below -85 dBm at $T < 1$ K). Although such a frequency dependence has not been observed yet for the dielectric properties of SiO (for glasses actually), this property is well known from the investigation of the specific heat of glasses, as it was discussed in section 2.1.1 and can be found in [3].

The question whether the discovered frequency dependence of the TLS density of states

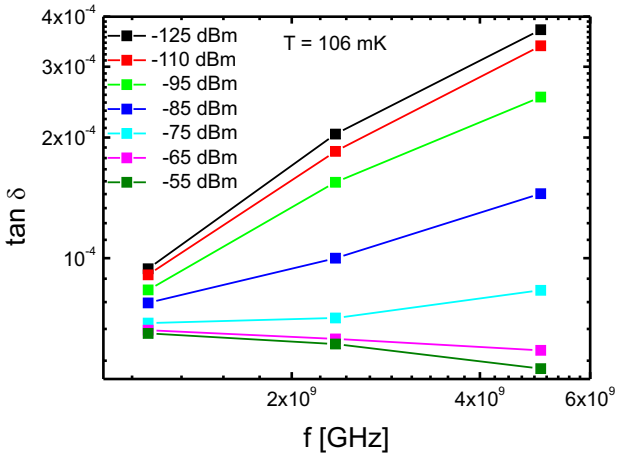

Figure 5.14:
Losses at 106 mK at certain power levels plotted over frequency. For power levels smaller than -85 dBm a frequency dependence of the losses becomes clearly visible, leading to the conclusion that the density of TLS states is frequency dependent (see text).

is equal to the one obtained from specific heat measurements could not be investigated yet. This as well as the anomalous effect of the frequency shift curve of $f = 1.179$ GHz in 5.12 showed the smallest shift (see explanation above) has to be investigated in more detail after the end of this thesis.

The discovered frequency dependence of the TLS density of states in amorphous dielectrics can be considered very important for the qubit technology as qubits work at frequencies between 6 and 10 GHz at mK temperatures and in the low power limit, a regime where losses are clearly dominated by resonant absorption. As according to the presented results, the losses are higher at higher frequencies due to the found frequency dependence of the TLS density of states, it should be considered whether it is possible to design qubits at frequencies lower than 6 to 10 GHz to reduce decoherence.

Chapter 6

Summary

As it is shown recently that two-level tunneling systems (TLSs) responsible for the qubit decoherence and dielectric losses are identical, one aim of this work was to investigate dielectric losses of amorphous materials usually used in qubit fabrication. Thereby, promising candidates for qubit fabrication should be figured out. In investigating dielectric loss in qubit working regime (very low temperatures $T < 1$ K and single photon excitation energies), a further goal arose, namely to reveal the physical properties of the TLSs themselves. In this thesis, an existing measurement method was used which is capable of direct and reliable evaluation of dielectric loss in amorphous thin films employing superconducting microwave resonators. It was enhanced by multiplexing the resonators. Therefore, it allowed to measure the losses in the film volume as well as the metal/dielectric interfaces quantitatively at several frequencies in a broad frequency range in one cooldown cycle. Firstly, the losses in thin films of Nb_2O_5, AlO_x, SiO, SiN_x and a-Si:H have been measured at 4.2 K and GHz frequencies, confirming results of former experiments whereby it was shown that the losses in the volume of such amorphous materials exceed the ones on the interfaces by far. With the new multiplexed resonator design, the frequency dependence of the losses was investigated confirming the formerly reported behavior to follow a universal law. This universality is expressed by fractional power laws in the form of $\tan\delta \propto \omega^{n-1}$, meaning that the dielectric loss is proportianl to frequency due to relaxation processes of two-level tunneling systems (TLSs) in the dielectrics. The found narrow range of $0.57 < n < 0.68$ for all different dielectrics investigated in within this thesis, assumed the TLSs to be many-body interacting dipoles of the same kind in all investigated dielectrics. The absolute loss values of all investigated dielectrics compared to each other ranged as predicted recently. Nb_2O_5 with the highest content of oxygen exhibit the highest losses by far, whereas a-Si:H with its defect states saturated by hydrogenation showed the lowest losses. Thus, a-Si:H is one of the most promising candidates for qubit fabrication. Despite its high loss, Nb_2O_5 is commonly used in Nb based qubit fabrication. Thus, it was tried to reduce dielectric loss in anodically oxidized Nb_2O_5 and AlO_x by using various electrolytes. However, no reduction of loss could be achieved. In the case of a-Si:H, it was tested whether the loss could be

reduced even more by special treatments of the superconductor-dielectric interface. So far, no success could be achieved.

Another very important part of this thesis was the investigation of the temperature, power and frequency dependencies of dielectric loss at temperatures $T < 1$ K using cryogenic cooling techniques. As standard low-temperature microwave setups are hindered by devices with a narrow frequency working range, a broadband measurement setup had to be developed. This new measurement setup including the multiplexed resonator design was able to perform reliable measurements of the frequency of dielectric losses for the first time, because the frequency dependence could be investigate in one cooldown cycle. At low powers and $T < 1$ K, an increase in loss for decreasing temperature was detected. Furthermore, a saturation effect of loss for decreasing power was observed. Additionally, a shift of the resonance frequencies to lower frequencies for decreasing temperature was measured. These phenomena were observed for all investigated frequencies and were in excellent agreement with the resonant absorption of photons by TLSs in terms of the tunneling model. Considering the frequency dependence of the losses, a frequency dependence of the TLS density of states could be clearly stated. Although this has not been seen so far, neither in investigations of dielectric loss in bulk glasses nor in investigations of TLSs induced loss in superconducting microwave resonators, it is in excellent agreement with investigations of the specific heat of glasses and it is not excluded in terms of the tunneling model. The discovered frequency dependence of the TLS density of states in amorphous dielectrics can be considered very important for the qubit technology as qubits work at frequencies between 6 and 10 GHz at mK temperatures and in the low power limit, a regime where losses are clearly dominated by resonant absorption. As according to the presented results, the losses are higher at higher frequencies due to the found frequency dependence of the TLS density of states, it should be considered whether it is possible to design qubits at frequencies lower than 6 to 10 GHz to reduce decoherence.

In the future, the frequency dependence of the TLS density of states should be investigated at further frequencies in order to figure out the quantitative relation between density and frequency. According to the results obtained at 4.2 K within this thesis, the nature of the TLSs is the same in all investigated dielectrics. Therefore, the frequency dependence of the losses of the remaining dielectrics should be investigated in the qubit working regime as well in order to confirm the universality of TLS behavior in amorphous thin films.

Bibliography

[1] R. C. Zeller, R. O. Pohl, *Thermal Conductivity and Specific Heat of Noncrystalline Solids*, Phys. Rev. B **4**, 2029 (1971).

[2] W. Arnold, S. Hunklinger, *Ultrasonic Properties of Glasses at Low Temperatures*, Physical Acoustics: Principles and Methods **12**, 155 (1976).

[3] R. B. Stephens, *Low-Temperature Specific Heat and Thermal Conductivity of Noncrystalline Dielectric Solids*, Phys. Rev. B **8**, 2896 (1973).

[4] P. W. Anderson, B. I. Halperin, C. M. Varma, *Anomalous low-temperature thermal properties of glasses and spin glasses*, Philos. Mag. **25**, 1 (1972).

[5] W. A. Phillips, *Tunneling states in amorphous solids*, J. Low Temp. Phys. **7**, 351 (1972).

[6] C. Enss, S. Hunklinger, *Low-Temperature Physics* (Springer Verlag, Berlin Heidelberg, 2005).

[7] U. Strom, M. von Schickfus, S. Hunklinger, *Low-Temperature Anomalies in the Microwave Dielectric Properties of Na β-Alumina*, Phys. Rev. Lett. **41**, 910 (1978).

[8] J. M. Martinis, K. B. Cooper, R. McDermott, M. Steffen, M. Ansmann, K. D. Osborn, K. Cicak, S. Oh, D. P. Pappas, R. W. Simmonds, C. C. Yu, *Decoherence in Josephson Qubits from Dielectric Loss*, Phys. Rev. Lett. **95**, 210503 (2005).

[9] A. D. O'Connell, M. Ansmann, R. C. Bialczak, M. Hofheinz, N. Katz, Erik Lucero, C. McKenney, M. Neeley, H. Wang, E. M. Weig, A. N. Cleland, J. M. Martinis, *Microwave Dielectric Loss at Single Photon Energies and milliKelvin Temperatures*, Appl. Phys. Lett. **92**, 112903 (2008).

[10] R. Barends, J. J. A. Baselmans, J. N. Hovenier, J. R. Gao, S. J. C. Yates, T. M. Klapwijk, H. F. C. Hoevers, *Niobium and Tantalum High Q Resonators for Photon Detectors*, IEEE Transaction on Applied Superconductivity **17**, 263 (2007).

[11] S. Kumar, J. Gao, J. Zmuidzinas, B. A. Mazin, H. G. LeDuc, P. K. Day, *Temperature dependence of the frequency and noise of superconducting coplanar waveguide resonators*, Appl. Phys. Lett. **92**, 123503 (2008).

[12] J. Gao, *Experimental evidence for a surface distribution of two-level systems in superconducting lithographed microwave resonators*, Appl. Phys. Lett. **92**, 152505 (2008).

[13] T. Lindström, J. E. Healey, M. S. Colclough, C. M. Muirhead, *On the properties of superconducting planar resonators at mK temperatures*, arXiv:0905.1481v1 (2009).

[14] P. Macha, S. H. W. van der Ploeg, G. Oelsner, E. Il'ichev, H.-G. Meyer, *Losses in coplanar waveguide resonators at millikelvin temperatures*, Appl. Phys. Lett. **96**, 062503 (2010).

[15] D. P. Pappas, M. R. Vissers, D. S. Wisbey, J. S. Kline, J. Gao, *Evaluation of Two Level Systems in Superconducting Resonators using Power and Temperature Dependence of Loss and Frequency*, IEEE ASC Conference Series **-**, 1 (2010).

[16] M. von Schickfus, S. Hunklinger, *The dielectric coupling of low-energy excitations in vitreous silica to electromagnetic waves*, J. Phys. C: Solid State Phys. **9**, L439 (1976).

[17] P. J. W. Debye, *Polar Molecules* (Dover Publications, New York, 1945).

[18] J. Lisenfeld, *Experiments on Superconducting Josephson Phase Quantum Bits*, Dissertation, Friedrich-Alexander-Universität Erlangen-Nürnberg, 2008.

[19] R. M. Hill, A. K. Jonscher, *The dielectric behaviour of condensed matter and its many-body interpretation*, Contemp. Phys. **24**, 75 (1983).

[20] A. K. Jonscher, *Universal relaxation law* (Chelsea Dielectrics Press Ltd, Chelsea, 1996).

[21] A. K. Jonscher, *Dielectric relaxation in solids*, J. Phys. D: Appl. Phys. **32**, R57 (1999).

[22] M. Pollak, B. Shklovskii, in *Hopping Transport in Solids*, Hrsg.: M. Pollak, B. Shklovskii (North Holland, 1000 AE Amsterdam, The Netherlands, 1991).

[23] K. L. Ngai, C. T. White, *Frequency dependense of dielectric loss in condensed matter*, Phys. Rev. B **20**, 2475 (1979).

[24] S. Havriliak, S. J. Havriliak, *Dielectric and mechanical relaxation in materials: Analysis, interpretation, and application to polymers* (Hanser Publishers, Munich and New York and Cincinnati, 1997).

[25] J. Rault, *Origin of the Vogel-Fulcher-Tammann law in glass-forming materials: the* $\alpha - \beta$ *bifurcation*, Journal of Non-Crystalline Solids **271**, 177 (2000).

[26] S. Shtrikman, E. P. Wohlfarth, *Theory Theory of the Vogel-Fulcher Law of Spin Glasses*, Phys. Lett. **85A**, 467 (1981).

[27] P. A. O'Connell, G. B. McKennab, *Arrhenius-type temperature dependence of the segmental relaxation below T_g*, J. Chem. Phys. **110**, 11054 (1999).

[28] H. A. Kramers, *Diffusion of light by atoms*, Atti. Congr. Intern. Fis. **2**, 545 (1927).

[29] R. L. Kronig, J. Opt. Soc. **12**, 547 (1926).

[30] W. A. Phillips, *Two-level states in glasses*, Rep. Prog. Phys. **50**, 1657 (1987).

[31] M. Abramowitz, I. A. Stegun, *Handbook of Mathematical Functions with Formulas, Graphs, and Mathematical Tables* (Dover Publications, New York, 1965).

[32] H. Kamerlingh Onnes, *On the sudden change in the rate at which the resistance of mercury disappears*, Leiden Commun. **124c**, (1911).

[33] W. Meißner, R. Ochsenknecht, Naturwissenschaften **21**, 787 (1933).

[34] M. Tinkham, in *Introduction to Superconductivity*, Hrsg.: M. Tinkham (Dover Publications, Inc., Mineola, New York, 2004).

[35] F. London, H. London, *The Electromagnetic Equations of the Supraconductor*, Proc. Roy. Soc. A **149**, 71 (1935).

[36] C. J. Gorter, H. B. J. Casimir, *Zur Thermodynamik des supraleitenden Zustandes*, Physica **1**, 306 (1934).

[37] S. Wünsch, *Supraleitende koplanare Mikrowellenfilter für radioastronomische Empfänger bei 15 K*, Dissertation, Universität Karlsruhe (TH), 2005.

[38] J. R. Bray, L. Roy, *Measuring the unloaded, loaded, and external quality factors of one- and two-port resonators using scattering-parameter Magnitudes at fractional power levels*, IEE Proc.-Microw. Antennas Propag. **151**, 345 (2004).

[39] G. Hammer, S. Wünsch, K. Ilin, M. Siegel, *Ultra high quality factor resonators for kinetic inductance detectors*, Journal of Physics: Conference Series **97**, 012044 (2008).

[40] P. Drude, *Zur Elektronentheorie der Metalle*, Annalen der Physik **306**, 566 (1900).

[41] D. C. Mattis, J. Bardeen, *Theory of the Anomalous Skin Effect in Normal and Superconducting Metals*, Phys. Rev. **III**, 412 (1958).

[42] A. Shnirman, G. Schön, I. Martin, Y. Makhlin, *Low- and High-Frequency Noise from Coherent Two-Level Systems*, Phys. Rev. Lett. **94**, 127002 (2005).

[43] J. Gao, A. Vayonakis, J. Zmuidzinas, M. Daal, B. Sadoulet, B. A. Mazin, P. K. Day, H. G. Leduc, J. M. Martinis, *A semi-empirical model for two-level system noise in superconducting microresonators*, arXiv:0804.0467v1 (2008).

[44] R. Barends, H. L. Hortensius, T. Zijlstra, J. J. A. Baselmans, S. J. C. Yates, J. R. Gao, T. M. Klapwijk, *Contribution of dielectrics to frequency and noise of NbTiN superconducting resonators*, arXiv:0804.3499v2 (2008).

[45] H. Wang, M. Hofheinz, J. Wenner, M. Ansmann, R. C. Bialczak, M. Lenander, E. Lucero, M. Neeley, A. D. O'Connell, D. Sank, M. Weides, A. N. Cleland, J. M. Martinis, *Improving the Coherence Time of Superconducting Coplanar Resonators*, arXiv:0909.0547v1 (2009).

[46] C. Song, M. P. DeFeo, K. Yu, B. L. T. Plourde, *Reducing microwave loss in superconducting resonators due to trapped vortices*, Appl. Phys. Lett. **95**, 232501 (2009).

[47] P. K. Day, H. G. LeDuc, B. A. Mazin, A. Vayonakis, J. Zmuidzinas, *A broadband superconducting detector suitable for use in large arrays*, Nature (London) **425**, 817 (2003).

[48] K. Cicak, D. Li, J. A. Strong, M. S. Allman, F. Altomare, A. J. Sirois, J. D. Whittaker, J. D. Teufel, R. W. Simmonds, *Low-loss superconducting resonant circuits using vacuum-gap based microwave components*, Appl. Phys. Lett. **96**, 093502 (2010).

[49] Ch. Kaiser, S. T. Skacel, S. Wünsch, R. Dolata, B. Mackrodt, A. Zorin, M. Siegel, *Measurement of Dielectric Losses in Amorphous Thin Films at Gigahertz Frequencies using Superconducting Resonators*, Supercond. Sci. Technol. **23**, 075008 (2010).

[50] Sonnet 12.52, Sonnet Software Inc., 1020 Seventh North Street, Suite 210, Liverpool, NY 13088, USA.

[51] A. P. S. Khanna, Y. Garault, *Determination of Loaded, Unloaded, and External Quality Factors of a Dielectric Resonator Coupled to a Microstrip Line*, IEEE Trans. Microw. Theory Tech. **31**, 261 (1983).

[52] R. Dolata, H. Scherer, A. B. Zorin, J. Niemeyer, *Single-charge devices with ultrasmall $Nb/AlO_x/Nb$ trilayer Josephson junctions*, Appl. Phys. Lett. **97**, 054501 (2005).

[53] Matlab R2010a, MathWorks, 3 Apple Hill Drive, Natick, Massachusetts 01760, USA.

[54] P. J. Petersan, S. M. Anlage, *Measurement of resonant frequency and quality factor of microwave resonators: Comparison of methods*, J. Appl. Phys. **84**, 3392 (1998).

[55] P. R. Bevington, *Data Reduction and Error Analysis for the Physical Sciences* (McGraw-Hill, New York, 1969).

[56] H. Störmer, E. Ivers-Tiffee, C. Schnitter, D. Gerthsen, *Microstructure and dielectric properties of nanoscale oxide layers on sintered capacitor-grade niobium and V-doped niobium powder compacts*, Int. J. Mat. Res. (formally Z. Metallkd.) **97**, 794 (2006).

[57] Harry Kroger, Josephson Device with Tunneling Barrier having Low Density of Localized States and Enhanced Figure of Merrit, 1984.

[58] P. Macha, Diplomarbeit, Physikalisch-Asrtonomische Fakultät, Friedrich-Schiller-Universität Jena, 2009.

Acknowledgements

First of all, I would like to thank Prof. Alexey. V. Ustinov and Prof. Michael Siegel for giving me the possibility of working in such an exciting field of research. For setting up the collaboration between the Physikalische Institut (PI) and the Institut für Mikro- und Nanoelektronische Systeme (IMS) at the KIT great thanks appertains to them, because this collaboration allowed me to achieve the interesting results I showed in this thesis. Not until, the free admission to the knowledge of both institutes made this interesting work possible.

Furthermore, I would like to thank Christoph Kaiser for being a great supervisor helping me with any challenge I had to face within the last three years I worked at the IMS. His personal support guided me through all new and pushed me to realize this fascinating work.
I would like to thank Stefan Wünsch, my personal microwave hero, for explaining me how microwave world works and for his humaneness. He always wrested a smile from me.
I would like to thank Hannes Rotzinger, my cryogenic guru, for helping me with all the setup at the PI and showing me how important patience can be, especially in the case of Janis.
I would like to thank Alexander Lukashenko for helping me to reach 106 mK in times I doubted whether I would be able to measure at this temperature within the time of my thesis. And of course I have to thank him for his jokes and songs.
I would like to thank Markus Jerger for his endless help with microwave devices and measurement tools which made my investigations possible.
I would like to thank Pascal Macha for intensive discussion giving me essential impulses.
Further deep thanks to Alexander Stassen who made things happen whenever I needed them.
I would like to thank Karlheinz Gutbrod, Hansjürgen Wermund, Roland Jehle and Reinhold Dehm for their technical support especially in situations when time was scarce.
I would like to thank Max, Alex, Axel, Petra, Dagmar, Matthias and Gerd for making work very enjoyable at the IMS.
I would like to thank Susanne, Anastasia, Jochen, Tobi, Bernhard, Philipp, Kirill, Piotr, Lyosch, Jürgen, Stefano and Gerda for providing a wonderful atmosphere at the PI.

Doch mein größter Dank gebührt meiner Gama und meinen Eltern, Monika Skacel und Werner Mülhaupt, die mich nicht verzweifeln ließen, vor allem in der letzten Zeit, die so unwahrscheinlich beschwerlich war und mir mehr abverlangt hat, als ich dachte leisten zu können. Ich liebe Euch von ganzem Herzen und aus tiefster Seele.
Danken möchte ich auch all meine Freunden, die immer an meiner Seite waren und mir Kraft gegeben haben. Ihr seid großartig.

It matters not how strait the gate,
How charged with punishments the scroll,
I am the master of my fate:
I am the captain of my soul.

Erklärung:

Ich versichere, dass ich diese Arbeit selbstständig verfasst und keine anderen als die angegebenen Quellen und Hilfsmittel benutzt habe.

Karlsruhe, den